

AD _____

Award Number: W81XWH-05-1-0221

TITLE: Development of an Automated Modality-Independent Elastographic Image Analysis System for Tumor Screening

PRINCIPAL INVESTIGATOR: Dr. Jao J. Ou
Dr. Michael I. Miga

CONTRACTING ORGANIZATION: Vanderbilt University
Nashville TN 37238-7749

REPORT DATE: February 2007

TYPE OF REPORT: Annual Summary

PREPARED FOR: U.S. Army Medical Research and Materiel Command
Fort Detrick, Maryland 21702-5012

DISTRIBUTION STATEMENT: Approved for Public Release;
Distribution Unlimited

The views, opinions and/or findings contained in this report are those of the author(s) and should not be construed as an official Department of the Army position, policy or decision unless so designated by other documentation.

REPORT DOCUMENTATION PAGE				<i>Form Approved</i> OMB No. 0704-0188	
Public reporting burden for this collection of information is estimated to average 1 hour per response, including the time for reviewing instructions, searching existing data sources, gathering and maintaining the data needed, and completing and reviewing this collection of information. Send comments regarding this burden estimate or any other aspect of this collection of information, including suggestions for reducing this burden to Department of Defense, Washington Headquarters Services, Directorate for Information Operations and Reports (0704-0188), 1215 Jefferson Davis Highway, Suite 1204, Arlington, VA 22202-4302. Respondents should be aware that notwithstanding any other provision of law, no person shall be subject to any penalty for failing to comply with a collection of information if it does not display a currently valid OMB control number. PLEASE DO NOT RETURN YOUR FORM TO THE ABOVE ADDRESS.					
1. REPORT DATE (DD-MM-YYYY) 01-02-2007		2. REPORT TYPE Annual Summary		3. DATES COVERED (From - To) 26 Jan 06 – 25 Jan 07	
4. TITLE AND SUBTITLE Development of an Automated Modality-Independent Elastographic Image Analysis System for Tumor Screening				5a. CONTRACT NUMBER	
				5b. GRANT NUMBER W81XWH-05-1-0221	
				5c. PROGRAM ELEMENT NUMBER	
6. AUTHOR(S) Dr. Jao J. Ou and Dr. Michael I. Miga E-Mail: jao.ou@vanderbilt.edu				5d. PROJECT NUMBER	
				5e. TASK NUMBER	
				5f. WORK UNIT NUMBER	
7. PERFORMING ORGANIZATION NAME(S) AND ADDRESS(ES) Vanderbilt University Nashville TN 37238-7749				8. PERFORMING ORGANIZATION REPORT NUMBER	
9. SPONSORING / MONITORING AGENCY NAME(S) AND ADDRESS(ES) U.S. Army Medical Research and Materiel Command Fort Detrick, Maryland 21702-5012				10. SPONSOR/MONITOR'S ACRONYM(S)	
				11. SPONSOR/MONITOR'S REPORT NUMBER(S)	
12. DISTRIBUTION / AVAILABILITY STATEMENT Approved for Public Release; Distribution Unlimited					
13. SUPPLEMENTARY NOTES					
14. ABSTRACT The objective of this project is to further develop modality-independent elastography as a system that is able to reproducibly detect regions of increased stiffness within the breast based on pre- and post- compression input images of the anatomy. As stated in the proposal, the original specific aims are concerned with enhancement of the method, investigation of texture and statistical analyses for evaluating the success of the method, and engineering of a device that can generate proper forces on mock setups within current available clinical imaging systems. To date, progress on each of these aims has been made in handling increased computational complexity, developing and testing metrics for the evaluation of reconstructions, and the fabrication of a compression chamber tested on a tissue-like polymer phantom.					
15. SUBJECT TERMS elastography, breast cancer screening, image processing					
16. SECURITY CLASSIFICATION OF:			17. LIMITATION OF ABSTRACT UU	18. NUMBER OF PAGES 76	19a. NAME OF RESPONSIBLE PERSON USAMRMC
a. REPORT U	b. ABSTRACT U	c. THIS PAGE U			19b. TELEPHONE NUMBER (include area code)

Table of Contents

Introduction.....	1
Body.....	1
Key Research Accomplishments.....	8
Reportable Outcomes.....	9
Conclusions.....	9
References.....	10
Appendices.....	11

Introduction

Early detection of masses within the breast that may transform into malignancies is known to be essential for positive treatment and outcome. Currently, mammography is the clinical standard for screening and provides useful but at times ambiguous information, which can necessitate further invasive workup of benign lesions. Recent research has indicated that a family of methods developed in the field of elastography holds promise as an alternative means of interrogating soft tissue structures by providing a spatial mapping of material properties (e.g. elasticity) that can be inspected for the detection of lesions [1, 2]. A technique known as ‘modality-independent elastography’ (MIE) [3-5] has been introduced with the intent of combining the intuitive discrimination from manual detection with the superior depth of penetration and anatomical detail typically given by imaging. The basic requirements for the method are two images of the tissue in different states of deformation (e.g. compression). Elasticity parameters are then reconstructed within the context of an inverse problem that utilizes non-rigid image registration constrained by a biomechanical model in order to best describe the composition of the tissue. The final result is a map of the breast (or other tissue of interest) that reflects material inhomogeneity, such as in the case of a tumor mass that disrupts the surrounding structure of normal tissue. Because MIE works on probing the differences between images, it can be used to not only work in concert with more traditional screening techniques but also address a possible gap when those methods are unable to directly discern tissues of interest.

Body

As stated in the original proposal, there are three main aims of this project: (1) to expand and refine the current MIE technique to enhance its efficiency and capabilities, (2) to perform analyses on texture in input images and quantify statistical parameters capable of estimating and evaluating the success of elastographic reconstruction, and (3) to engineer a device that is compatible with current medical imaging systems and can produce compressive forces appropriate for phantom and/or clinical setups. The relevant proposed and completed work is listed below and organized as closely as possible to the two major arcs of the Statement of Work.

Task 1(a) stated: **“Incorporation of additional biomechanical models (e.g. 3D and 2D/3D deformation effects).”**

Initial work with MIE involved reconstructions of circular stiff inclusions embedded within thin rectangular membranes of polyurethane rubber. The materials used have essentially indistinguishable colors but vary significantly in their elastic modulus values (a contrast ratio of approximately 5.7:1 as confirmed by material testing by an Enduratec ELF 3200). A black permanent marker was used to place a pattern of regularly spaced (~1 cm) grid lines across the membrane, which was then securely clamped along two opposite edges and subjected to a uniaxial tensile displacement (~8% strain) by means of a milling vise. A commercial webcam was rigidly mounted above the membrane to acquire image pairs of the pre- and post-deformation states. The intent of these experiments was to have a means of performing relatively quick 2D analyses and possibly develop an application for dermoscopic evaluation of skin lesions. The model utilized the plane stress approximation [6], which is actually a reduction of

the 3D formulation of Cauchy's Law. However, because the skin has multiple layers in which a potential lesion might be present, it was uncertain whether the use of planarity was suitable for elastographic work. In particular, the subcutaneous layer of adipose tissue that serves to essentially lubricate the epidermis and dermis may have a non-trivial thickness such that in-plane loading is no longer confined to a sufficiently thin slab. Therefore, a 2D/3D comparison was performed to examine the effects of model assumptions on deformations used in the reconstruction process. Two physical characteristics of the domain were examined: the depth of penetration of the stiff lesion (simulating a melanoma) and the thickness of the subcutaneous layer. Full 3D deformations were solved over a finite element mesh, projected to the surface, and aligned to the dermoscopic image before proceeding to the elastographic reconstruction. Figures 1 and 2 show the coupling of the 3D model with 2D reconstruction. The analysis of the recovered elasticity distributions indicated that deeper lesions were more accurately characterized, and the thickness of the subcutaneous layer had no significant impact on the reconstruction. Further details of this work can be found in Appendix D.

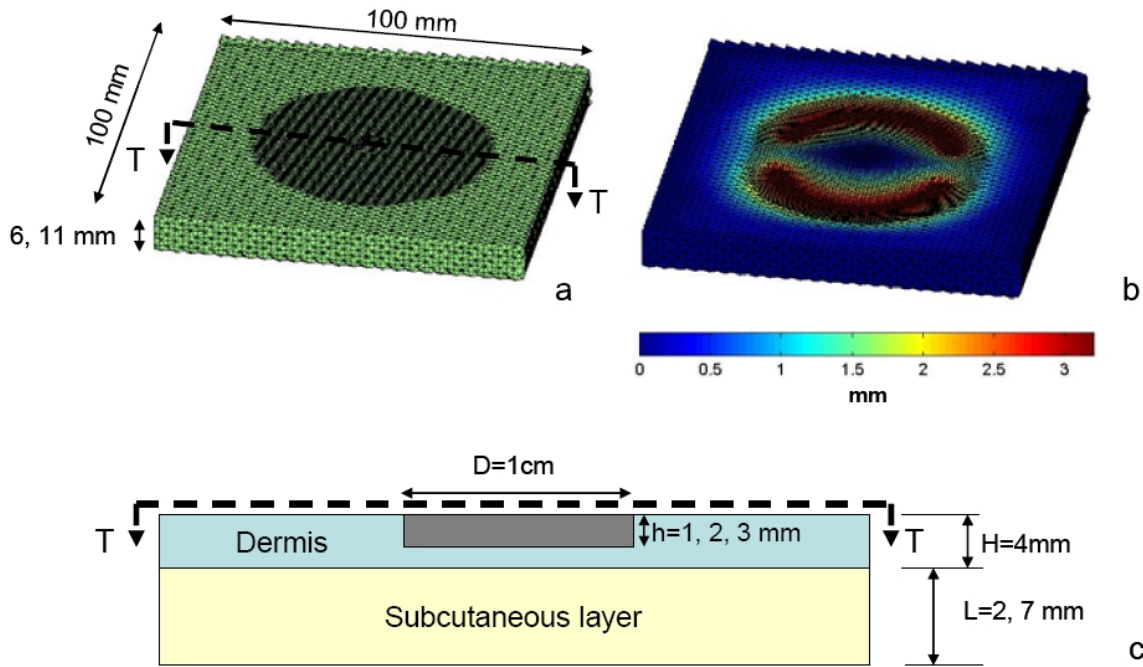


Figure 1. MIE 2D/3D experiment setup. (a) finite element mesh (b) overlay of displacements induced by hypothetical dermoscopic probe (c) diagram of skin composition in mesh (gray=lesion) from side view.

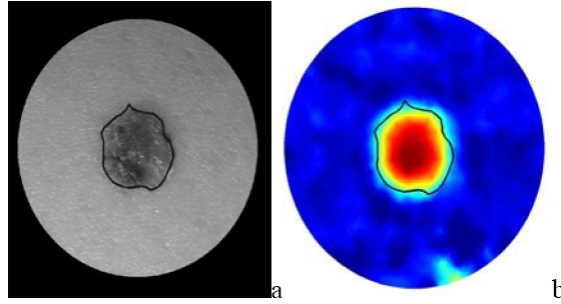


Figure 2. MIE 2D/3D images. (a) source image obtained from a digital photograph of a melanoma (b) sample simulation reconstruction obtained by experiment shown in Figure 1. Black overlays in both frames denotes border of lesion.

Task 1(b) stated: **“Design and implementation of computational code routines (e.g. modification of finite element model).”** and Task 1(c) stated: **“Enhancement of model programming structure via numerical analysis and parallelization.”**

In order to accommodate the methodology of MIE in creating a Jacobian matrix fully sensitive to the discretization of the domain, a large number of solutions involving the finite element model and the subsequent image deformation are required. With the proposed increase in dimensionality to handle 3D data, the implementation complexity quickly increases beyond the capabilities of the original MATLAB/FORTRAN/LAPACK design. Therefore, the Portable Extensible Toolkit for Scientific Computation (PETSc) toolkit [7,8] was selected to provide the necessary framework for developing sparse matrix system solvers and split the Jacobian formation process. A separate C/C++ routine has also been written to perform a Gauss-Newton optimization and interface with PETSc solver structures. This framework is flexible enough to accommodate the use of 2D models such that unified data structures and formats are now employed, and multi-resolution capabilities present in the previous 2D-only codebase are now available in 3D.

It was previously reported that by using a share of 100 CPUs from the Vanderbilt University Advanced Computing Center for Research and Education cluster, speedups in the overall computation of over two orders of magnitude were achieved. This actually indicated a superlinear path over predictions from Ahmdal’s Law [9]; however, recent observations indicate that although significant gains are regularly made in employing parallel code, heterogeneity of machine power and network latencies may actually hinder efficiency. This is hypothesized to be a consequence of the current design of the internal messaging system and may be resolved by adjusting the current master-slave relationship to utilize a dynamic SPMD (single program, multiple data) flow concept wherein the master attempts to concurrently designate a task to the next available processor while accepting the latest completed job. An in-house cluster of 18 processors (2.0 Ghz Pentium 4 Xeon) is now available for performing additional reconstructions and further benchmarking to investigate this enhancement.

Task 1(d) stated: **“Design of texture analysis parameter for predicting elastographic reconstruction effectiveness.”**

Earlier work had examined the effects in 2D of noise in both the image and boundary condition selection. The primary conclusions of that work were that degradation in the image of up to 10% randomized noise was within the expected behavior of most acquisition systems, and that boundary mismappings of less than 0.5 pixel units was generally tolerated by the reconstruction algorithm. For further detail, please see the full text of this work as listed in Appendix B.

With the recent move to 3D reconstruction work, it has become of increasing concern to analyze the effects of boundary condition estimation. Because similarity metrics (e.g. correlation coefficients) typically normalize and/or blur the intensity distribution [10], image noise can be tolerated fairly well. However, any inaccuracy in the boundary condition set propagates through the model and into image deformation, thereby having a significant impact on the evaluation of the objective function and the success of the reconstruction. The current method of selecting displacement (Type 1) boundary conditions requires manual interaction to guide or correct point correspondence for every surface node. Assuming that an input device (e.g. a mouse) is needed to identify the specific coordinates, this introduces an operator-dependent noise process in localizing any given point. A gold standard boundary condition set was derived by simulating compression of the breast with a device described below in the work related to Task 2. Reconstructions were performed using randomized vectors to disrupt the target surface; the results of this experiment indicate that improper localization of boundary points greater than or equal to 0.5 units of voxel spacing can introduce significant error to the reconstruction process and impair its ability to characterize the underlying elasticity distribution. This is a similar result to that found from the prior work done in 2D [Appendix B]. It also confirms that randomizing the vectors is a significant challenge to the algorithm because of the introduction of highly non-physical deformations that cause backlash in the finite element mesh and other numerical anomalies.

The increase in dimensionality from 2D to 3D necessitates much higher discretization levels in meshing and pre-processing work. To effectively cover the surface of a CT volume requires over 6,000 nodes, which would result in an unreasonable task for manual boundary condition selection. Therefore, an automated method for determining surface correspondence and then interpolating those results into displacements for boundary condition sets is needed. Three methods of surface registration and point correspondence were considered; two are derived from surface matching of potential energy distributions based on the diffusion and Laplace equations, and the other is a free-form warping via a thin-plate spline. For complete details on the methods and buildup from previous work, please see documents provided in Appendix D and Appendix F. Compared to the gold standard boundary condition set, the target registration error was greatest for the diffusion method and least (best) for the thin-plate spline. Energy matching from the solutions of the diffusion and Laplace equations yielded boundary condition sets that were inadequate for reconstructing a proper elasticity contrast. This can be partly explained because the mean errors of those surface registration techniques (as compared to the gold standard and in an equivalent sense to the tested noise levels) are approximately 3.3 and 1.7 voxel units, respectively, and are far too large for the algorithm to handle. The diffusion-based boundary conditions also proved more difficult to obtain a stable solution for in the model, which further contributed to the mismatch in reconstructed elasticity contrast. However, the results obtained using the thin-plate spline method are encouraging because the mean error was 0.43 voxel units,

thereby satisfying the threshold (<0.5 voxel units) while demonstrating reconstruction success. The reconstruction behavior in that case was consistent with the predicted objective function space and the optimal elasticity contrast was found to be within 6% of the true value. This preliminary result appears to identify the use of thin-plate spline interpolation as a strong candidate for generating boundary conditions for MIE. The implementation for that method required the use of 40 control points, which is seen as a reasonable choice in placing fiducials for data acquisition in order to capture the extent of anticipated deformation processes. A more detailed explanation of this work and summary of experimental results is provided in the accompanying document found in Appendix E.

Task 2(a) stated: **“Design and construction of breast phantoms with simulated tumors.”**

We have opted to work with polyvinyl alcohol cryogel (PVA-C) because of its relative ease and safety in manufacture and handling. The polymer has previously been described as being a desirable material for the fabrication of both ultrasound and MR elastography phantoms for use in representing the brain, blood vessels, and breast [11-13]. To create a breast-shaped fascimile, approximately 650 cc of 8% wt/vol polymer solution is molded in a plastic container for 1 or 2 freeze-thaw-cycles. The result is a dome shape approximately 10-11 cm at the base and tapering over a depth of about 5-6 cm.

Because of its use of intensity-based image similarity metrics, the MIE methodology requires image texture in the variation of intensity values within the domain to perform a registration assessment based on similarity. While the natural structures of the breast present little concern in resulting in a homogeneous distribution, introducing usable patterns into a phantom poses some technical challenges in order to not have intensity correlate too strongly with structural differences and to avoid altering the elastic properties by creating a heterogeneous composite material. A method that has been found to be potentially satisfactory for MIE involves doping a separate quantity of polymer solution with an imaging contrast agent. Before the phantom fully polymerizes through freezing, a hypodermic needle is used to create multiple tracts of the contrast-enhanced slurry, thereby creating regions of different intensity while maintaining a nearly homogeneous bulk material. Figure 14 below shows a few slices of a PVA-C phantom constructed in this manner using iohexol suspension (Omnipaque®, GE Healthcare, Chalfont St. Giles, UK) and scanned by a clinical CT unit.

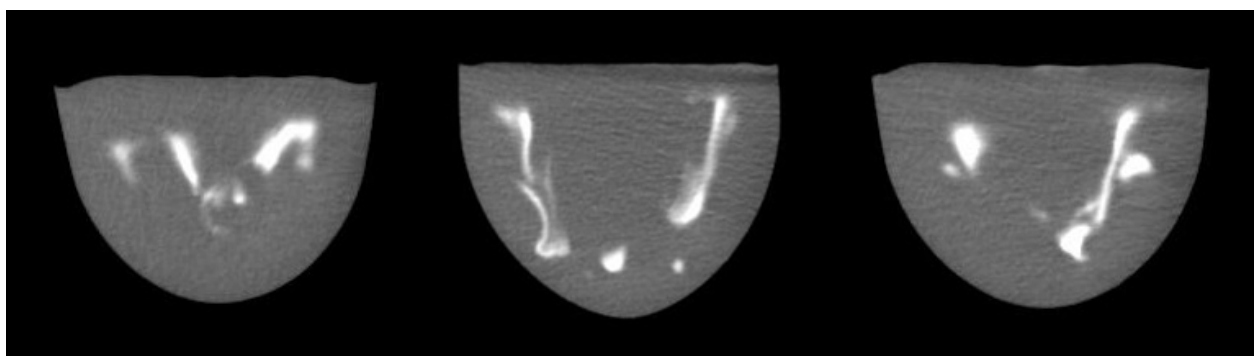


Figure 3. Selected views of a PVA-C breast phantom using iodine injections and imaged by CT.

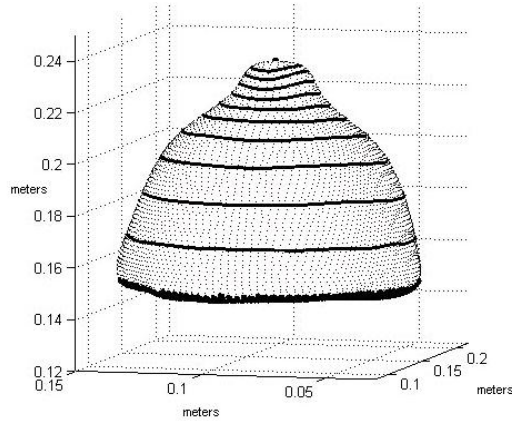
Experimentation has also led to a protocol that should allow for the creation and implantation of a simulated tumor in the phantom. Prior to manufacture of the main breast phantom, a spherical inclusion can be made (out of a significantly stiffer piece of PVA-C) about 2.5-cm in diameter by using at least two freeze-thaw-cycles on the liquid polymer. This inclusion can then be suspended within the main breast mold to let the bulk material solidify around it.

Task 2(b) stated: **“Prototype construction of compression device including design modifications to optimize compatibility with current imaging modalities.”** and Task 2(c) stated: **“Conduct breast phantom experiments to investigate efficacy of MIE reconstruction while varying parameters (e.g. degree of compression) during imaging.”**

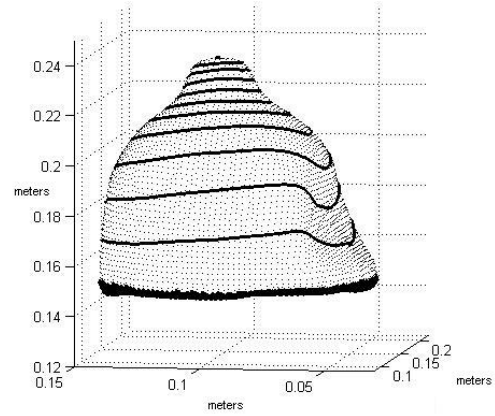
Two sets of compression devices have been constructed and found to be compatible in magnetic resonance (MR) and X-ray computed tomography (CT) imaging systems. Both devices are primarily composed of a clear acrylic material and make use of neoprene air bladders to deliver a compression of up to 5 cm. The first device is a rectangular Plexiglas frame that traps the phantom in at least two directions with a sliding wall and fixed wall which houses the air bladder. This unit has been used on PVA-C phantoms fabricated as described above. Figure 4 below illustrates the use of the device (in this case, in CT); the specifics of the experiment are described in Appendix F.

A prototype compression chamber that is more clinically oriented has been designed to fit into the chassis of a Philips Intera breast coil unit. In order to retain the geometry of the overall device, which is made to accommodate 95% of the population for imaging purposes according to the manufacturer, the chamber was fabricated from by cutting cylindrical segments at $\sim 27^\circ$. The air bladders are attached using polycarbonate pins to face the cranial and caudal (supra- and infra-mammary aspects, respectively) surfaces of the breast. The overall assembly is then covered with an expandable nylon sheet (see Figure 5).

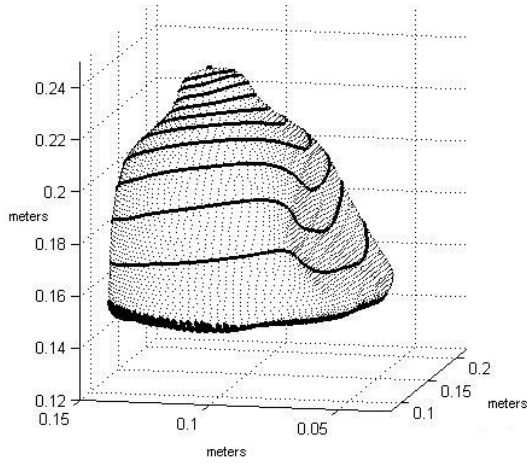
Image acquisition studies in conjunction with the Vanderbilt University Institute of Imaging Science have recently begun to demonstrate the clinical feasibility of the design. A Philips Achieva 3T equipped with field strengths up to 80 mT/m, and slew-rates up to 200T/m/s and an eight channel SENSE breast coil has been used for all breast imaging. The target and deformed images were acquired with a 3D T_1 -weighted high resolution isotropic volume exam (THRIVE) that includes a fat-nulling inversion pulse. Pulse sequence parameters were TR/TE=6.19ms/3.2ms with a flip angle of 10° and a NEX=1. 129 2-mm thick slices were acquired with an acquisition matrix was 400x400 zero reconstructed to 512x512 over a field of view of 20 cm² to 25.6 cm² (depending on breast size). This sequence design is currently being utilized for initial MIE analysis and will be altered accordingly if necessary. Figure 6 below shows a sample image slice of a patient breast with a tumor obtained from the MIE clinical compression chamber.



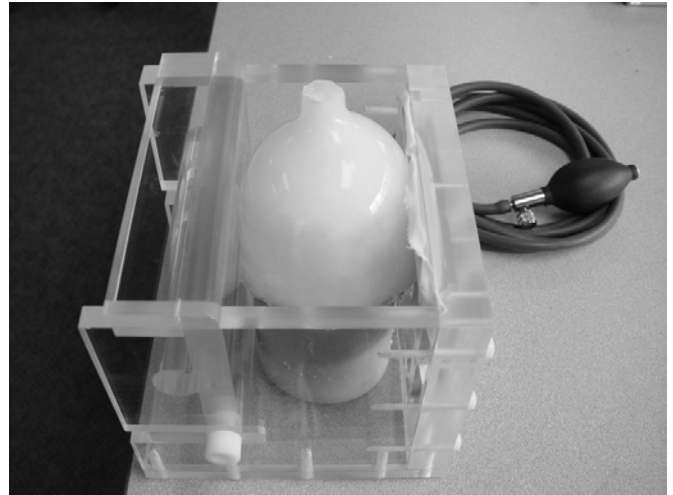
(a)



(b)



(c)



(d)

Figure 4. Experimental system for image data acquisition on phantoms. A polyvinyl alcohol cryogel is placed within a Plexiglas chamber with its surfaces held in place against the walls. (a)-(c) volumetric segmentations of the CT image volume taken of the phantom at 0%, 50%, and 100% inflation of the air bladder. (d) photograph of the setup. Compression is delivered through an air bladder (right wall in picture) inflated manually through a bulb adapted from a standard sphygmomanometer. [from Appendix F]

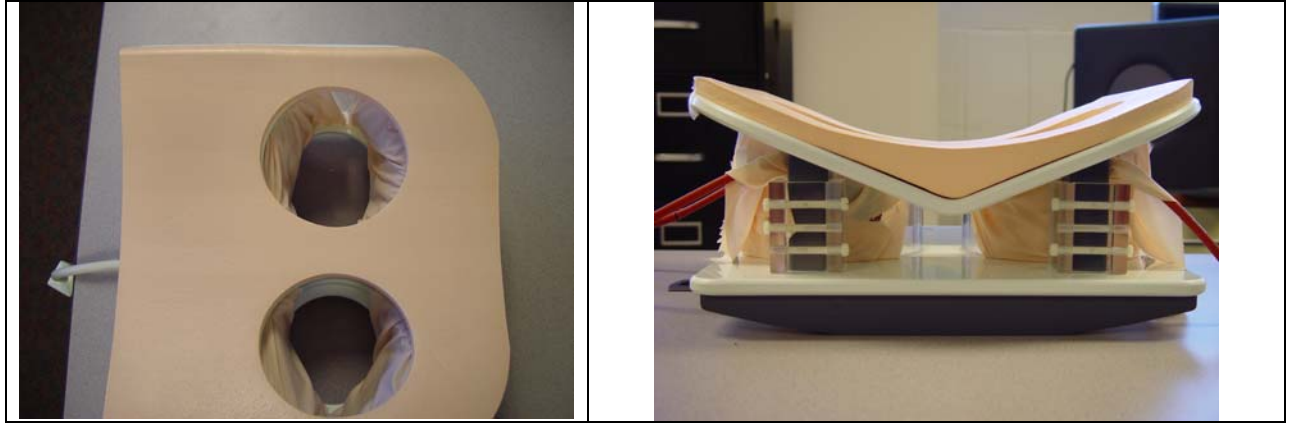


Figure 5. Left: Photograph of assembly looking down into the Philips Intera breast coil unit. Right: front view of the device, which is clamped to the chassis but does not interfere with the imaging field of view.

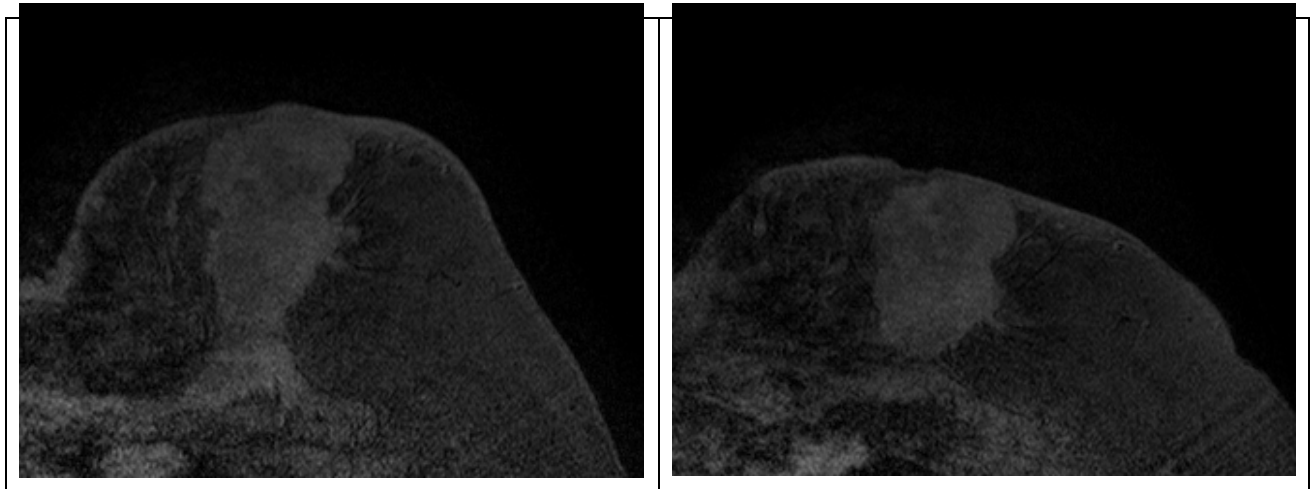


Figure 6. Example slices of an MR image obtained of a breast (a) before and (b) after compression as delivered by the clinical MIE chamber.

Key Research Accomplishments

Although the basic requirements of a static compression and pre-/post- image analysis that are the foundation of MIE are simple conceptually compared with other elastography methods, the implementation of a robust system is a significant engineering challenge. The flexibility of the parallelized code base is for this project has provided an interesting avenue of analysis of a large-scale nonlinear optimization problem. In addition, the relatively easy translation of data acquisition system designs to the clinic is a key breakthrough for the project to demonstrate the safety and applicability of the method in a real-world setting, whether on phantom or human subjects.

Reportable Outcomes

Work on the MIE method has so far resulted in multiple conference papers. Prior work that was completed in the reporting timeline resulted in a peer-reviewed journal publication. These items have provided the foundation for a thesis proposal approved by the graduate school, as well as a forthcoming manuscript currently being prepared.

Poster presentations

Vanderbilt University Medical Scientist Training Program retreat (July 2006). Brentwood, TN.

Conference papers

Ou JJ, Barnes SL, and Miga MI, "Application of multi-resolution modality independent elastography for detection of multiple anomalous objects," in Medical Imaging 2006: Physiology, Function and Structure from Medical Images, San Diego, CA, Feb 2006, pp. 614310-1 to 614310-9.

Ou JJ, Barnes SL, Miga MI, "Preliminary testing of sensitivity to input data quality in an elastographic reconstruction method," in IEEE International Symposium on Biomedical Imaging, Arlington, VA, Apr 2006, pp. 948-951.

Schuler DR, **Ou JJ**, Barnes SL, Miga MI, "Automatic surface correspondence methods for a deformed breast," in Medical Imaging 2006: Visualization and Image-Guided Procedures, San Diego, CA, Feb 2006, pp. 614125-1 to 614125-8.

Ou JJ, Ong RE, Miga MI, "An Evaluation of 3D Modality Independent Elastography Robustness to Boundary Condition Noise", SPIE Medical Imaging 2007. Accepted Oct 2006, In press.

Ong RE, **Ou JJ**, Miga MI, "Using Laplace's equation for non-rigid registration of breast surfaces", SPIE Medical Imaging 2007. Accepted Oct 2006, In press.

Miga MI, **Ou JJ**, Ellis DL, "An elastography framework for use in dermoscopy", SPIE Medical Imaging 2007. Accepted Oct 2006, In press.

Conclusions

The current results and progress denoted in this report are within the proposed statement of work and are encouraging towards completion of the overall objectives with further effort. No significant deviations are reported at this time.

References

- [1] Garra BS, Cespedes I, Ophir J, et al. Elastography of breast lesion: Initial clinical results. *Radiology* 1997;202:79–86.
- [2] McKnight AL, Kugel JL, Rossman PJ, Manduca A, Hartmann LC, Ehman RL. MR Elastography of Breast Cancer: Preliminary Results. (2002) *Am. J. Roentgenol.* 178, 1411-1417
- [3] M. I. Miga, "A new approach to elastography using mutual information and finite elements," *Physics in Medicine and Biology*, vol. 48, pp. 467-480, Feb 21 2003.
- [4] C. W. Washington and M. I. Miga, "Modality independent elastography (MIE): a new approach to elasticity imaging," *IEEE Trans Med Imaging*, vol. 23, pp. 1117-28, Sep 2004.
- [5] M. I. Miga, M. P. Rothney, and J. J. Ou, "Modality independent elastography (MIE): potential applications in dermoscopy," *Med Phys*, vol. 32, pp. 1308-20, May 2005.
- [6] A. Boresi and K. P. Chong, *Elasticity in Engineering Mechanics*, 2nd ed.: Wiley-Interscience, 1999.
- [7] Balay S, Buschelman K, Eijkhout V, Gropp WD, Kaushik D, Knepley MG, McInnes LC, Smith BF, Zhang H. "PETSc Users Manual", ANL-95/11 Revision 2.1.5. Argonne National Laboratory, 2004.
- [8] Balay S, Gropp WD, McInnes LC, Smith BF. "Efficient Management of Parallelism in Object Oriented Numerical Software Libraries", Modern Software Tools in Scientific Computing. Birkhauser Press, pp. 163-202, 1997.
- [9] G. Ahmdahl, "Validity of the single processor approach to achieving large-scale computing capabilities," in *AFIPS Conference Proceedings*, 1967, pp. 483-485.
- [10] J. M. Fitzpatrick, D. L. G. Hill, and C. R. Maurer, "Image registration," in *Handbook of Medical Imaging*. vol. 2: SPIE Press, 2000, pp. 447-513.
- [11] K. C. Chu and B. K. Rutt, "Polyvinyl alcohol cryogel: an ideal phantom material for MR studies of arterial flow and elasticity," *Magn Reson Med*, vol. 37, pp. 314-9, Feb 1997.
- [12] K. J. Surry, H. J. Austin, A. Fenster, and T. M. Peters, "Poly(vinyl alcohol) cryogel phantoms for use in ultrasound and MR imaging," *Phys Med Biol*, vol. 49, pp. 5529-46, Dec 21 2004.
- [13] E. Brusseau, J. Fromageau, G. Finet, P. Delachartre, and D. Vray, "Axial strain imaging of intravascular data: results on polyvinyl alcohol cryogel phantoms and carotid artery," *Ultrasound Med Biol*, vol. 27, pp. 1631-42, Dec 2001.

Appendix

The following is a listing of original works referred to in the Body of the Report. Full reprints and other relevant supplemental material are provided after this description.

		Page
A.	Ou JJ, Barnes SL, Miga MI, “Application of multi-resolution modality independent elastography for detection of multiple anomalous objects”, <i>SPIE Medical Imaging 2006</i> .	1
	(Condensed) slides from oral presentation, February 2006.	10
B.	Ou JJ, Barnes SL, Miga MI, “Preliminary testing of sensitivity to input data quality in an elastographic reconstruction method”, <i>IEEE International Symposium on Biomedical Imaging 2006</i> .	19
	(Condensed) slide of poster presentation, April 2006.	23
C.	Schuler DR, Ou JJ, Barnes SL, Miga MI, “Automatic surface correspondence methods for a deformed breast,” <i>SPIE Medical Imaging 2006</i> .	24
D.	Miga MI, Ou JJ, Ellis DL, “An elastography framework for use in dermoscopy”, <i>SPIE Medical Imaging 2007</i> .	32
E.	Ou JJ, Ong RE, Miga MI, “An Evaluation of 3D Modality Independent Elastography Robustness to Boundary Condition Noise”, <i>SPIE Medical Imaging 2007</i> .	43
F.	Ong RE, Ou JJ, Miga MI, “Using Laplace’s equation for non-rigid registration of breast surfaces”, <i>SPIE Medical Imaging 2007</i> .	52

Application of multi-resolution modality independent elastography for detection of multiple anomalous objects

Jao J. Ou, Stephanie L. Barnes, Michael I. Miga
 {jao.ou,steph.barnes,michael.i.miga}@vanderbilt.edu
 Vanderbilt University, Department of Biomedical Engineering, Nashville, TN 37235

ABSTRACT

This work extends a recently realized inverse problem technique of extracting soft tissue elasticity information via non-rigid model-based image registration. The algorithm uses the elastic properties of the tissue in a biomechanical model to achieve maximal similarity between image data acquired under different states of loading. A new multi-resolution, non-linear optimization framework has been employed which allows for improved performance and object detection. Prior studies have demonstrated successful reconstructions from images of a tissue-like thin membrane phantom with a single embedded inclusion that was significantly stiffer than its surroundings. For this investigation, a similar phantom was fabricated with two stiff inclusions to test the effectiveness of this method in discriminating multiple smaller objects. Elasticity values generated from both simulation and real data testing scenarios provided sufficient contrast for detection and good quantitative localization of the inclusion areas.

Keywords: Elastography, elasticity imaging, multi-resolution methods, image similarity, finite elements

1. INTRODUCTION

The practice of palpating soft tissue structures in the course of the clinical physical exam has had a long-standing history of providing correlation of improper stiffness with pathology. The ability to characterize the mechanical properties of tissue is a potential source of additional information relevant for detection and diagnosis of a disease process, and has implications for the assessment of treatment. One way in which this could be achieved in a minimally invasive manner is by analyzing tissue deformation through imaging and/or image processing techniques, which is a central goal of the field of elastography [1]. Application of such methods to the interrogation of the breast [2,3], skin [4-6], prostate [7], and other accessible organ systems is an emerging area of research.

Many of the current elastography methods are founded in ultrasound (US) and magnetic resonance imaging (MR) and involve the estimation of induced displacements within the tissue of interest to infer the elasticity distribution. We have pursued the development of a reconstruction method utilizing quasi-static deformation and image similarity metrics that has been termed 'modality-independent elastography' (MIE) [8-10] because of its potential to handle native anatomical image data from different modalities with simple modification to the acquisition procedure. Common problems facing all of these methods involve limitations with the accurate recovery of elastic property values, detection of small lesions in tissue, and the resolution of multiple discrete lesions [11,12]. Building upon recent study involving a single focal lesion [6], the objectives of this work were to challenge the ability of the MIE method to reconstruct a scenario of two small inclusions embedded in a homogeneous domain and to further explore the feasibility of the method in handling image data from different imaging modalities. This was accomplished by performing simulated reconstructions using images obtained from X-ray computed tomography (CT), MR, and digital photography and then a reconstruction from a real-world experiment using a thin phantom membrane.

2. METHODS

2.1 Elastographic reconstruction framework

The conceptual framework for our elastographic reconstruction has been previously described in [6,8-10]. In brief, an image of a tissue of interest (*source*) is deformed by a biomechanical computer model and compared against an acquired image of the same tissue in a mechanically loaded state (*target*). The deformation and comparison is repeated

using systemic updates of elasticity parameters until a suitable match in intramodal image similarity is achieved in a least squares manner to satisfy a multi-resolution, non-linear optimization scheme. This process can be classified as an inverse problem, with model-based deformation of the source image representing the forward problem. Each of the three major components (model, image comparison, and optimization) is described in more detail in the following sections, and a flow chart representation of the overall process is included in Figure 1.

2.1.1 Biomechanical model

A central component to the model-based inverse problem is the manner in which the continuum is represented. While the constitutive model that best describes tissue deformation mechanics is more complex, for this work, linear isotropic elasticity has been employed. The partial differential equation that expresses a state of mechanical equilibrium can be written as [13]:

$$\nabla \bullet \sigma = 0 \quad (1)$$

where σ is the Cartesian stress tensor.

For the purposes of the following experimentation, we also apply either the plane stress or plane strain approximations to the thin membrane and breast cross-section trials, respectively. The direct consequence of this is a reduction of the 36 stiffness constraints in the general 3D formulation of Cauchy's Law to the two parameters of Young's modulus (E) and Poisson's ratio (ν) in 2D. These simplifications, while significant, are appropriate descriptions of sufficiently thin and thick systems under planar loading. In plane stress,

$$\begin{bmatrix} \sigma_x \\ \sigma_y \\ \tau_{xy} \end{bmatrix} = \frac{E}{(1-\nu^2)} \begin{bmatrix} 1 & \nu & 0 \\ \nu & 1 & 0 \\ 0 & 0 & (1-\nu)/2 \end{bmatrix} \begin{bmatrix} \varepsilon_x \\ \varepsilon_y \\ \gamma_{xy} \end{bmatrix} \quad (2)$$

describes the constitutive relationship between the Cartesian stress tensor $[\sigma_x, \sigma_y, \tau_{xy}]$ and strain tensor $[\varepsilon_x, \varepsilon_y, \gamma_{xy}]$. Similarly, in plane strain,

$$\begin{bmatrix} \sigma_x \\ \sigma_y \\ \tau_{xy} \end{bmatrix} = \frac{E(1-\nu)}{(1+\nu)(1-2\nu)} \begin{bmatrix} 1 & \nu/(1-\nu) & 0 \\ \nu/(1-\nu) & 1 & 0 \\ 0 & 0 & (1-2\nu)/2(1-\nu) \end{bmatrix} \begin{bmatrix} \varepsilon_x \\ \varepsilon_y \\ \gamma_{xy} \end{bmatrix} \quad (3)$$

A finite element (FE) model using triangular elements is constructed from the source image and assigned appropriate boundary conditions based on estimated displacement or stress (i.e. Dirichlet and Neumann conditions, respectively). The standard Galerkin method of weighted residuals [14] is used to construct and solve the system.

2.1.2 Image deformation and comparison

To further describe the reconstruction process, we introduce some additional terminology at this point. The *model domain* is equivalent to the total area of the FE mesh constructed using the *source* image as stated above and contains the relevant elasticity information. The model domain is partitioned by a K-means clustering of the element centroids (MATLAB R14, Mathworks, Natick, MA) into N number of *regions*, each of which has a distinct set of spatially homogeneous elastic properties. Subdividing in this manner allows for the implementation of the multi-resolution reconstruction whereby progressively finer spatial distributions of elasticity parameters are utilized in the process, a method that improves upon previous versions using only a single resolution [8-10]. Analogously, the *comparison domain* is an area specified by semi-automated segmentation on the *target* image and contains information pertaining to image similarity. The comparison domain is separated into M number of rectangular *zones* containing approximately equal numbers of pixels.

The reconstruction algorithm begins by assigning an initial Young's modulus value to each of the regions at the coarsest resolution. Poisson's ratio is held constant at $\nu = 0.485$ to represent a nearly incompressible material. The FE model is solved to determine the nodal mesh displacements, which are in turn used to deform the source image. This model-deformed image is then compared to the target image for every zone using an intensity-based image similarity metric. While a number of methods are available for such a task, here, we utilize the correlation coefficient (CC) [15] throughout, as it has empirically demonstrated superior performance over other metrics such as the sum of squared differences and normalized mutual information.

2.1.3 Optimization scheme

Let T be a function that represents the model-based image deformation and takes as its input a vector of elastic modulus values \mathbf{E} of length N that corresponds to the current distribution of regions in the model domain. Then for two distributions of modulus values \mathbf{E}_1 and \mathbf{E}_2 , the similarity between the images produced by $T(\mathbf{E}_1)$ and $T(\mathbf{E}_2)$ is the vector \mathbf{S} of length M containing evaluations of the correlation coefficient corresponding to the distribution of zones in the comparison domain. The elasticity parameter optimization can be written as the minimization of the least squares error objective function

$$\Psi = |\mathbf{S}_{TRUE} - \mathbf{S}_{EST}|^2 \quad (4)$$

where \mathbf{S}_{TRUE} is the set of similarity values achieved when comparing the target image to itself, \mathbf{S}_{EST} is the similarity between the model-deformed source and the target images using current estimates of the elastic modulus distribution, and $|\cdot|$ denotes the vector L_2 norm. By definition, \mathbf{S}_{TRUE} is the maximum value for the similarity metric (max CC = 1). Using a Levenberg-Marquardt approach, the residual form of equation (4) becomes

$$[J^T J + \alpha I] \{\Delta E\} = [J^T] \{\mathbf{S}_{TRUE} - \mathbf{S}_{EST}\} \quad (5)$$

where $\mathbf{J} = \partial \mathbf{S}_{EST} / \partial \mathbf{E}$ is the Jacobian matrix of size $M \times N$ and \mathbf{I} is the $N \times N$ identity matrix. Because $\mathbf{J}^T \mathbf{J}$ is typically an ill-conditioned term, the regularization parameter α is determined using the methods described in [16]. Modulus values of the regions at a given resolution are updated by ΔE until an error tolerance is reached or a maximum number of iterations have been completed. Upon reaching a stopping criterion, the material property description is interpolated onto the next (i.e. finer) resolution and the above steps are repeated. Spatial averaging of modulus values within the model domain and solution relaxation between successive resolution levels are also utilized to improve the stability of the optimization.

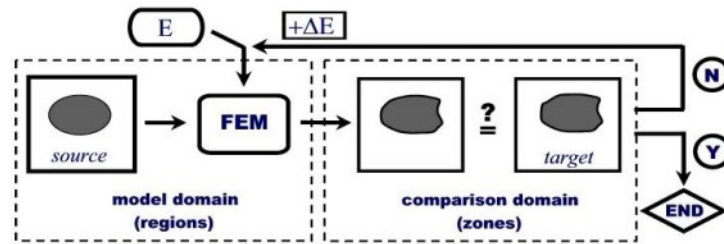


Figure 1. Flow chart of elastographic reconstruction framework.

2.2 Reconstruction experiments

A two-material phantom membrane of simulated skin had been previously constructed [6] using Smooth-On™ polyurethanes (Smooth-On, Easton, PA) designated by the manufacturer as Evergreen 10 and Evergreen 50. These materials have essentially indistinguishable colors but vary significantly in their elastic modulus values, so the former was used as the bulk material and the latter for stiff objects. From material testing, the elastic modulus contrast was expected to be approximately 5.7:1. The phantom was made to contain two circular stiff inclusions 1.5 cm in diameter

embedded near opposing corners of a rectangular field of bulk material measuring 15 cm x 14 cm. A black permanent marker was used to place a pattern of regularly spaced (~ 1 cm) grid lines across the membrane. The thin membrane was securely clamped along two opposite edges and then subjected to a uniaxial tensile displacement ($\sim 8\%$ strain) by means of a milling vise. A commercial webcam (Logitech QuickCam Pro 4000, 960 x 1280 pixel resolution) was rigidly mounted above the membrane to acquire image pairs of the pre- and post-stretched states.

To initially test the method regarding the two-inclusion scenario, a simulation using the source image of the membrane was performed by deforming it with a prescribed model (plane stress) of known boundary displacements and elasticity parameters to generate a target image; high modulus values were assigned to elements bounded by a segmentation of the inclusion locations. A reconstruction was then performed using the actual image data acquired as described above. In both cases, resolutions of $N = 16, 64, 256, 512$, and 800 regions and $M = 400$ zones were used. The results of the idealized and real data reconstructions are shown in Figures 4 and 5, with further quantitative evaluation in Table 1.

In order to examine the robustness of the method regarding its use of data from differing sources, simulation reconstructions were performed using image slices extracted from breast image volumes obtained from CT and MR scans (see Figure 3). Although these were taken from two different patients, the images were selected to be approximately corresponding slices ~ 2 cm away from the chest wall in the coronal orientation of the standard anatomical position. The simulations were set up in the same manner as for the digital photographs, using either one or two inclusions of about 1 cm in diameter embedded within the true elasticity distribution and a small compression ($\sim 8\%$ strain) in the cranial-caudal direction. The relative stiffness of the inclusions was designated to be 5.7:1 for consistency with the material testing data and also because the value is fairly representative of breast tumor properties [17]. The plane strain model approximation was used in the breast simulation trials, progressing through resolutions of $N = 24, 64, 256$, and 576 regions using $M = 200$ zones. The reconstruction method was then run for all four test cases, and the results are presented in Figures 6 and 7 and Table 2.

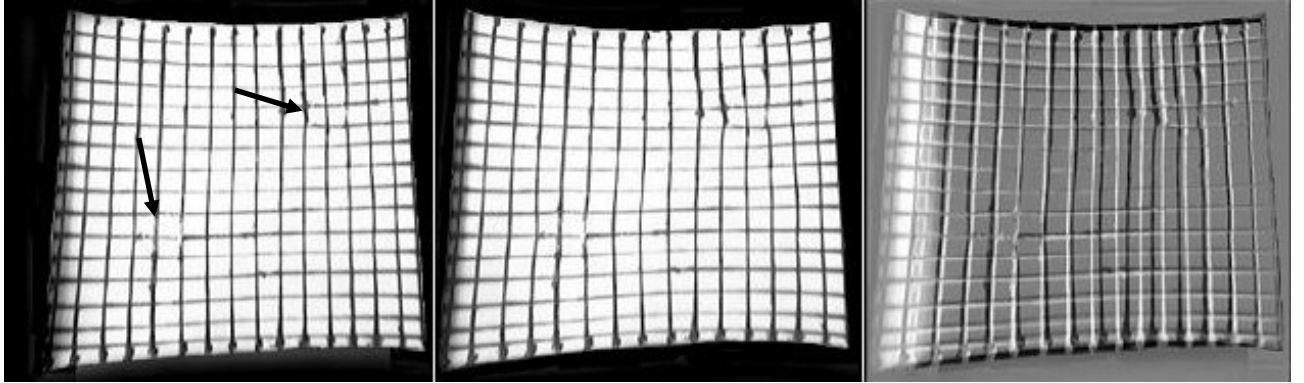


Figure 2. (Left to right): Phantom membrane in undeformed state (*source* image), under deformation (*target* image), and difference image. Arrows in the left panel indicate the positions of the two stiff inclusions.

2.3 Reconstruction evaluation

The fidelity of the elasticity reconstruction was evaluated on its ability to detect the presence of an inclusion based on classification of the material property distribution, and the retrospective accuracy of localizing the lesions. The elastic properties as a whole were treated as a Gaussian mixture of two classes and separated by a threshold established via the method described in [18]. The likelihood of detecting a lesion in the elasticity image was found using the contrast-to-noise ratio as defined by [12,19]:

$$CNR = \sqrt{\frac{2(\mu_L - \mu_B)^2}{\sigma_L^2 + \sigma_B^2}} \quad (6)$$

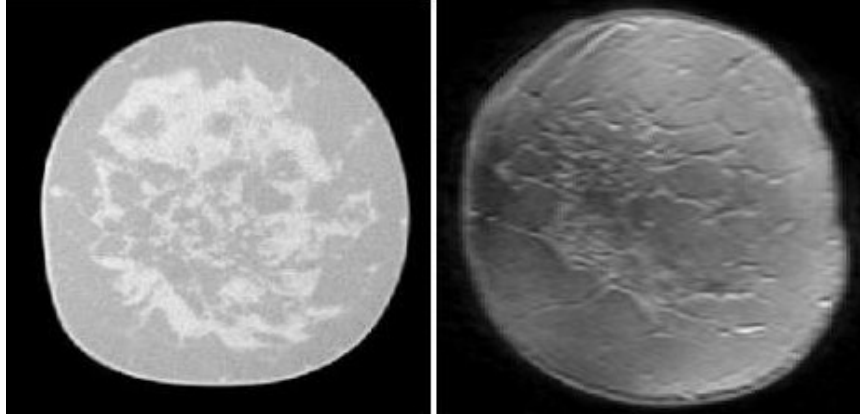


Figure 3. Images slices of breast tissue extracted from a CT volume (left) and MR volume (right) used in simulation study of the ability of the reconstruction method to utilize disparate image data types.

where μ and σ^2 are the sample mean and variance of a material property distribution and the subscripts L and B denote the lesion and bulk material classes, respectively. As a quantitative assessment of the localization of the lesion(s), the positive predictive value of correctly identifying a lesion material within the known segmented region of the inclusions was used as a 'quality of reconstruction score' (QRS). This value is significant because identification of the lesion border and material classification are done independently, so any user knowledge of the test scenario does not influence the performance of the measure. Cutoffs for successful detection and localization were set at $\text{CNR} \geq 2.2$ as noted by [12] and $\text{QRS} \geq 80\%$ as determined by prior study in our laboratory. The average modulus contrast is found from the ratio of the means of the two material classes, and a peak modulus contrast value is also reported by taking the ratio of two manually selected homogeneous regions of approximately equal area known to be representative of the two materials. It should be noted that in other work not presented here, the definition of QRS included a weighting factor provided by the estimated reconstruction modulus contrast, but for the current purposes, only localization accuracy was considered to maintain an objective evaluation of inclusion detection.

3. RESULTS

Figure 4 demonstrates the ability of the reconstruction method to produce an elasticity map from the simulation data with good localization of the inclusions that are easily visually distinguishable from the surrounding bulk material. The progression through resolutions of $N = 64, 256, 512$, and 800 regions shows improving delineation of the inclusions and elastic contrast. Figure 5 demonstrates a similar behavior for the reconstruction of the acquired phantom membrane data, with both spatial definition and modulus contrast increasing with the finer discretization. Table 1 summarizes the quantitative evaluation of the reconstructions in both simulation and phantom trials, including CNR, contrast ratio, and QRS values. The CNR values are sufficient to allow for discrimination of the two materials and the identification of the inclusions was determined to be accurate in both cases. The reconstruction of the phantom membrane does show some misclassification along the border where the deformation was applied as well as in the corner adjacent to one of the inclusions (see Figure 5d).

Figures 6 and 7 show the final reconstruction results for the CT and MR breast slice simulations using either one or two inclusions. In both test scenarios, the resolvability of the stiffer material was found to be adequate according to the CNR threshold, but definitely higher in the MR-derived elasticity images. Localization of the inclusions yielded excellent QRS values in reconstructions using either modality, again higher (though slightly) for the MR images.

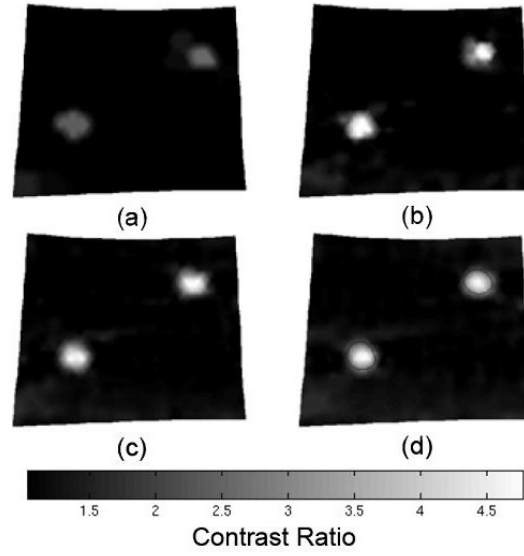


Figure 4. Reconstruction of the simulated membrane deformation using idealized model parameters, progressing through finer resolution distributions (a)-(d) of 64, 256, 512, and 800 regions.

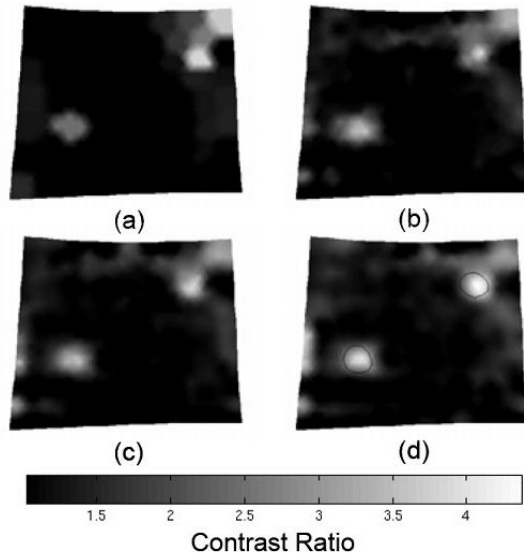


Figure 5. Reconstruction of the actual membrane data. A faint contour in (d) is present to demarcate the actual position of the stiff inclusions. Again, panels (a)-(d) demonstrate the effect of the multi-resolution method in utilizing 64, 256, 512, and 800 regions to better capture the shape and location of the inclusions.

Table 1. Quantitative reconstruction evaluations.

	Avg CR	Max CR	CNR	QRS (%)
Simulation	2.7	4.0	4.4	97.7
Phantom	2.6	4.1	2.8	88.5

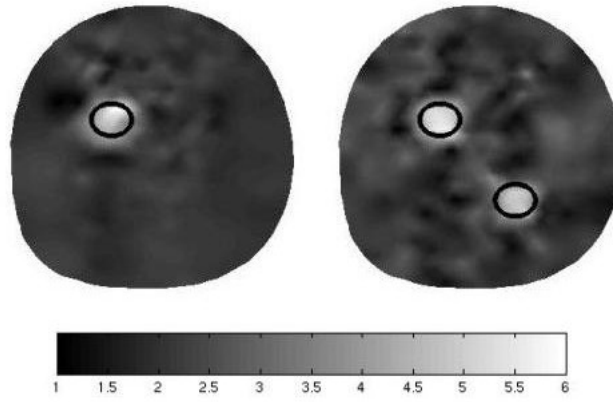


Figure 6. Reconstructions of simulation trials for the CT breast slice using a single inclusion (left) and two inclusions (right). The true inclusion boundaries are overlaid in each elasticity image.

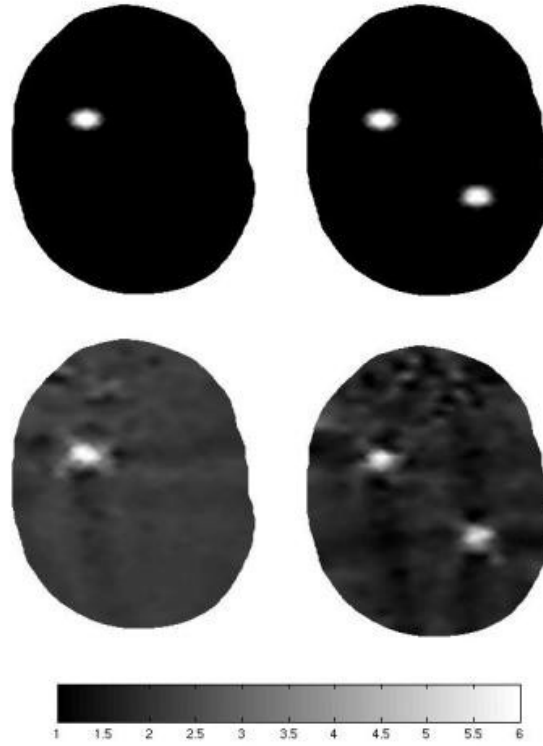


Figure 7. Reconstructions (bottom row) of simulation trials for the MR breast slice using a single inclusion (left) and two inclusions (right). The true elasticity distributions are also shown (top row) for comparison.

Table 2. Quantitative reconstruction evaluations.

	Avg CR	Max CR	CNR	QRS (%)
CT (1 inclusion)	2.1	3.1	3.0	97.6
CT (2 inclusions)	2.0	2.6	3.5	96.9
MR (1 inclusion)	2.8	3.7	20.0	100
MR (2 inclusions)	2.7	3.7	5.7	99.8

4. DISCUSSION

The results of the phantom membrane experiment are encouraging because of their similarity to the idealized simulation. Despite nonlinear model-data mismatch, out-of-plane distortions during stretching, and possible boundary condition inaccuracies, the elasticity reconstruction demonstrated good localization of the two small inclusions. The majority of the problems in reconstruction are mostly likely due to noise incurred in the mapping of the boundary displacements. It should be noted that the phantom reconstruction was achieved with a non-pigmented lesion (see Figure 2, arrows), indicating that deflections of the image structure are capable of driving the image similarity metric of the reconstruction process. This does intuitively suggest that some metric for rating the complexity and density of image pattern in relation to algorithm success may be important and is currently under investigation. Preliminary data not presented in this work indicates that such a threshold does exist for image data that can be properly analyzed by the current framework. The modality independence of the method is also supported by the results here; clearly, the Hounsfield units of CT, floating point values from an MR volume, and the luminance captured by the CCD sensor of a digital camera are quite different types of data to handle because they are based on different physical principles. The simulation reconstructions demonstrate that the method is indifferent to these differences by treating the data as an arbitrary range of intensities and will converge towards the true elasticity distribution based on the image pattern available. This is a possible explanation for the qualitatively more satisfactory results from the MR simulations compared to the CT trials because the distribution of intensities from the former modality yielded a more diversified histogram, an attribute that should naturally aid an intensity-based metric.

While an ideal reconstruction would also be accurate in characterizing a lesion by its modulus contrast, our focus in the study was to test the ability of the method to detect and localize the inclusions. In previous experimentation with reconstructions of single focal lesions, we have been generally successful in achieving a contrast ratio within 25% of the true/expected value. It is somewhat troubling that the contrast ratios calculated here did not meet that criterion, although the experiments with the phantom membrane came fairly close (28%). However, these results underscore the difficulty of the scenarios in not only having to deal with multiple inclusions but quite small ones in both the true physical sense and also the scale of the domain. Any of the given inclusions tested in simulation and with the real data were detected within a homogeneous domain approximately an order of magnitude larger (e.g., 1.5-cm lesions in a 15 cm x 14 cm domain for the phantom). The expectation of being able to identify with any confidence the presence of the inclusion is comparable to the observations made in [12] where the test of finding a single 5-mm lesion within a 4 cm x 5 cm domain proved to be the most problematic. Therefore, the localization of the lesions as determined by the CNR and QRS metrics is deemed to be a success, and further investigation into the nature of the method with respect to the scale of the lesion and domain is warranted.

5. CONCLUSIONS

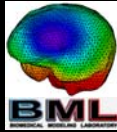
In this work, we have presented further testing of a method for recovering elasticity parameters by maximizing the similarity between images of a tissue of interest acquired under two different states of quasi-static loading within the context of an inverse problem. The specific experiments presented here examined the effectiveness of the technique for the detection of multiple small discrete focal lesions embedded in an otherwise homogeneous medium, as well as further proof-of-concept work in its applicability to utilize image data from various modalities. In both cases, the method provided accurate localization of the lesions based on the reconstruction of relevant elasticity contrast. Because the biomechanical model, multi-resolution optimization, and image acquisition are each modular components of the framework, this elastographic reconstruction technique is readily extensible for added sophistication, and there is ongoing work to enhance the methodology with more complex models and advances in imaging technology.

ACKNOWLEDGMENTS

The authors would like to thank John Boone, PhD of the University of California-Davis, Department of Radiology and Tom Yankeelov, PhD of the Vanderbilt University Institute of Imaging Science for their generous contributions of breast image data (CT and MR, respectively). This work was supported in part by the Whitaker Foundation Young Investigator Award and the Congressionally Directed Medical Research Program BCRP Predoctoral Traineeship Award.

REFERENCES

- [1] J. Ophir, I. Cespedes, H. Ponnekanti, Y. Yazdi, and X. Li, "Elastography - a quantitative method for imaging the elasticity of biological tissues," *Ultrasonic Imaging*, vol. 13, pp. 111-134, 1991.
- [2] A. L. McKnight, J. L. Kugel, P. J. Rossman, A. Manduca, L. C. Hartmann, and R. L. Ehman, "MR elastography of breast cancer: preliminary results," *AJR Am J Roentgenol*, vol. 178(6), pp. 1411-1417, 2002.
- [3] R. Sinkus, M. Tanter, T. Xydeas, S. Catheline, J. Bercoff, M. Fink, "Viscoelastic shear properties of *in vivo* breast lesions measured by MR elastography," *Magn Reson Imaging*, vol. 23(2), pp. 159-165, 2005.
- [4] L. V. Tsap, D. B. Goldgof, S. Sarkar, and P. S. Powers, "A vision-based technique for objective assessment of burn scars," *IEEE Trans Med Imaging*, vol. 17, pp. 620-633, 1998.
- [5] Y. Zhang, D. B. Goldgof, S. Sarkar, and L. V. Tsap, "A modeling approach for burn scar assessment using natural features and elastic property," *IEEE Trans Med Imaging*, vol. 23, pp. 1325-1329, 2004.
- [6] M. I. Miga, M. P. Rothney, and J. J. Ou, "Modality-independent elastography (MIE): potential applications for dermoscopy," *Medical Physics*, vol. 32, pp. 1308-1320, 2005.
- [7] L. Curiel, R. Souchon, O. Rouviere, A. Gelet, and J. Y. Chapelon, "Elastography for the follow-up of high-intensity focused ultrasound prostate cancer treatment: initial comparison with MRI," *Ultrasound Med Biol*, vol. 31(11), pp. 1461-1468, 2005.
- [8] C. W. Washington and M. I. Miga, "Modality independent elastography (MIE): a new approach to elasticity imaging," *IEEE Trans Med Imaging*, vol. 23, pp. 1117-1128, 2004.
- [9] M. I. Miga, "A new approach to elastography using mutual information and finite elements," *Phys Med Biol*, vol. 48, pp. 467-480, 2003.
- [10] M. I. Miga, "A new approach to elastographic imaging: modality independent elastography," *Proceedings of the SPIE*, vol. 4684, pp. 604-611, 2002.
- [11] K. J. Parker, L. S. Taylor, S. Gracewski, and D. J. Rubens, "A unified view of imaging the elastic properties of tissue," *J Acoustical Soc of America*, vol. 117(5), pp. 2705-2712, 2005.
- [12] M. M. Doyley, J. B. Weaver, E. E. W. Van Houten, F. E. Kennedy, and K. D. Paulsen, "Thresholds for detecting and characterizing focal lesions using steady-state MR elastography," *Medical Physics*, vol. 30(4), pp. 495-504, 2003.
- [13] A. Boresi, *Elasticity in Engineering Mechanics*, Wiley-Interscience, 2000.
- [14] L. Lapidus and G. F. Pinder, *Numerical Solution of Partial Differential Equations in Science and Engineering*, John Wiley & Sons, 1982.
- [15] J. M. Fitzpatrick, D. L. G. Hill, C. R. Maurer, "Image registration," *Handbook of Medical Imaging*, vol. 2. SPIE Press, pp. 447-513, 2000.
- [16] N. Joachimowicz, C. Pichot, and J. P. Hugonin, "Inverse scattering: an iterative numerical method for electromagnetic imaging," *IEEE Trans Biomed Engineering*, vol. 39, pp. 1742-1752, 1991.
- [17] T. A. Krouskop, T. M. Wheeler, F. Kallel, B. S. Garra, and T. Hall, "Elastic moduli of breast and prostate tissues under compression," *Ultrasonic Imaging*, vol. 20, pp. 260-274, 1998.
- [18] N. Otsu, "A threshold selection method from gray-level histograms," *IEEE Trans Syst Man Cybern*, vol. 9, pp. 62-66, 1979.
- [19] M. Bilgen, "Target detectability in acoustic elastography," *IEEE Trans Ultrason Ferroelectr Freq Control*, vol. 46, pp. 1128-1133, 1997.



13 Feb 2005

Application of Multi-resolution Modality Independent Elastography for Detection of Multiple Anomalous Objects

Jao J. Ou, Stephanie L. Barnes, Michael I. Miga

Vanderbilt University
Dept. of Biomedical Engineering
Nashville, TN 37235



Modality Independent Elastography (MIE) Concepts

- (Solid) tumors are usually stiffer than surrounding tissue
- Soft tissue interrogation of various organ systems (e.g. skin, liver, prostate, breast) for tumor detection
- Elastography gives representation of a structure according to its mechanical properties
- Deformation processes indicative of material inhomogeneity can be captured by imaging and approximated with modeling
- Associate form and function through image analysis separate from modality acquisition



MIE Components

- (1) Biomechanical FE model of soft-tissue deformation
- Conservation of stresses (continuum)

$$\nabla \cdot \sigma = 0$$

- Constitutive stress-strain relation (Hooke's Law)

$$\sigma = E\varepsilon$$

MIE Components (cont.)

- (2) Similarity measure for comparing images
- Acquired "pre-" (**source**) & "post-" (**target**) quasi-static deformation
- Intensity-based registration metrics
 - MI, NMI, SSD, CC, GC

MIE Components (cont.)

- (3a) Optimization routine to update material properties in the model

- Objective function based on similarity

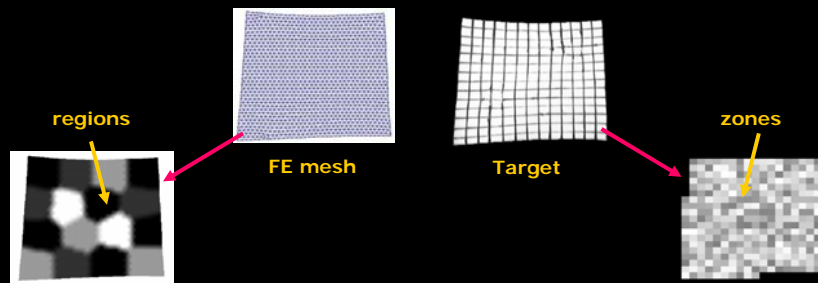
$$\Phi(E) = \sum_{m=1}^M (S(E_T)_m - S(E_E)_m)^2$$

- Levenberg-Marquardt

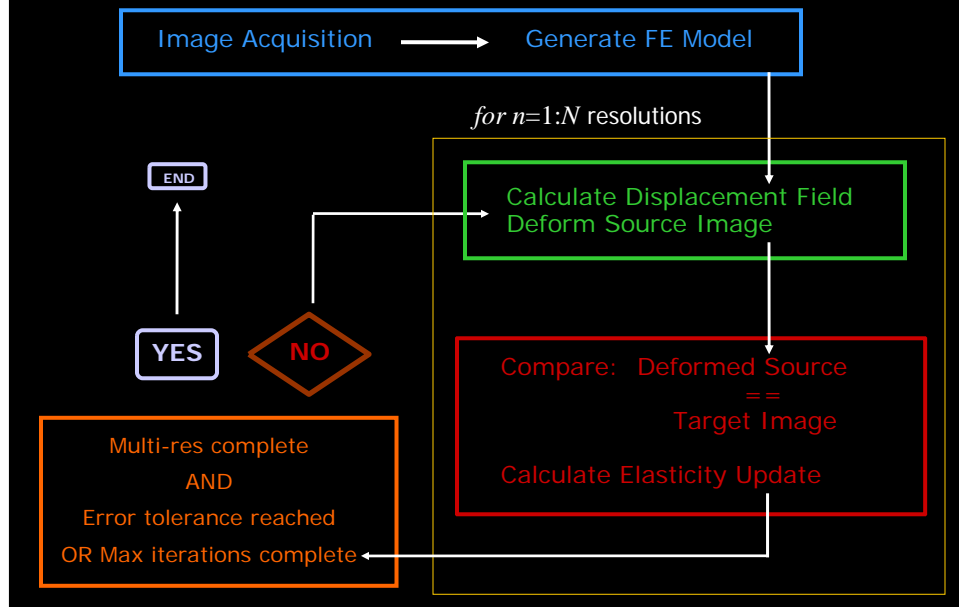
$$(J^T J + \alpha I) \Delta E = J^T (S(E_T) - S(E_E))$$

MIE Components (cont.)

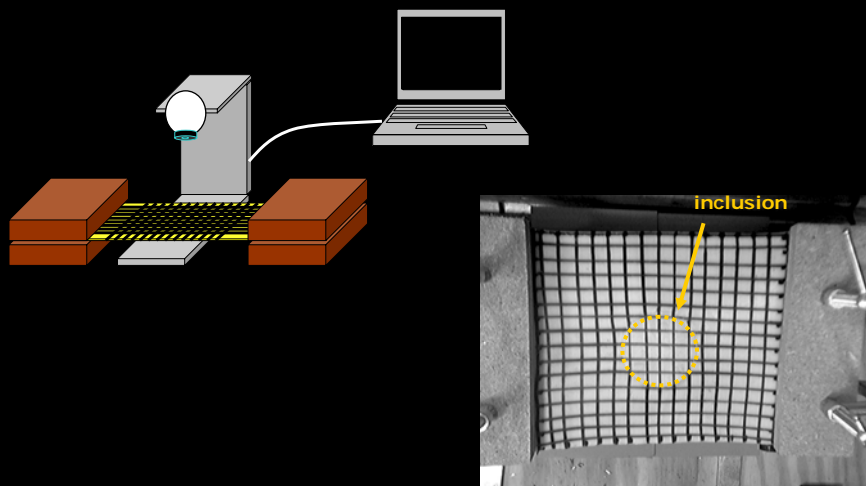
- (3b) Discretization of elasticity distribution and image data
 - Multi-resolution K-means clustering of elements ("regions")
 - Sampling of image comparison area ("zones")



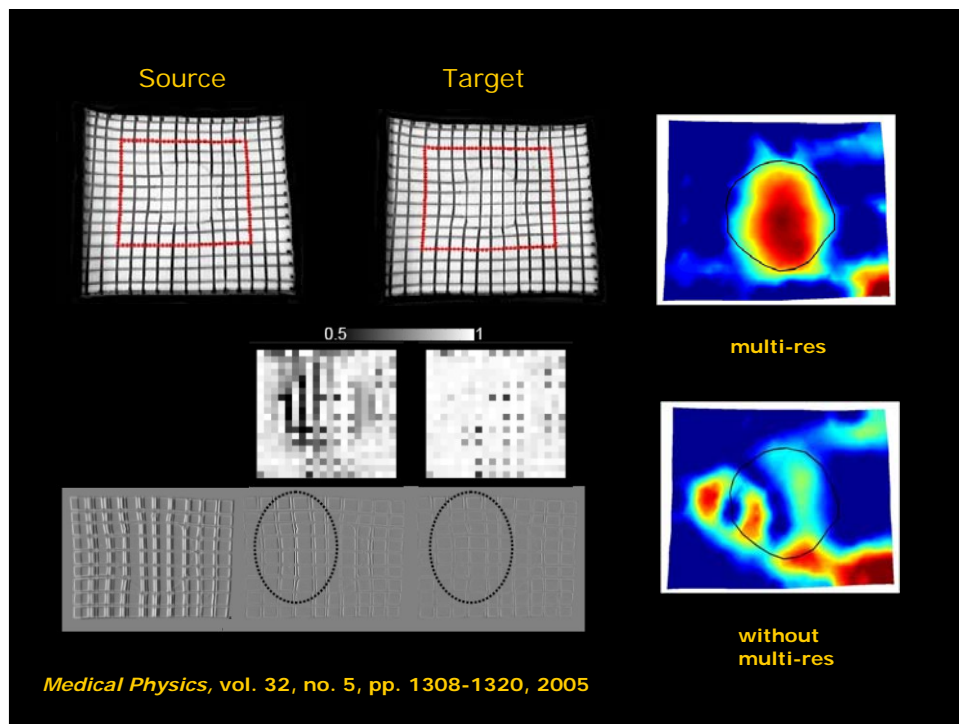
MIE Framework



Prior Work – Single Inclusion



Medical Physics, vol. 32, no. 5, pp. 1308-1320, 2005



Study Objectives:

Further Testing of MIE

- Modality independence
 - Digital photography
 - X-ray computed tomography (CT)
 - Magnetic resonance (MR)
- Two (small) inclusions
- Simulation and phantom membrane study

Evaluating MIE

- Classify reconstruction
Two-class Gaussian mixture model
- Detectability via elasticity image contrast

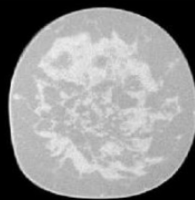
$$CNR = \sqrt{\frac{2(\mu_L - \mu_B)^2}{\sigma_L^2 + \sigma_B^2}} \geq 2.2$$

- Localization accuracy
Positive predictive value of identifying lesion material in correct location

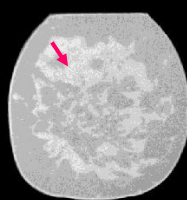
$$QRS = \frac{TP}{TP + FP} \geq 80\%$$

CT breast slice - simulation

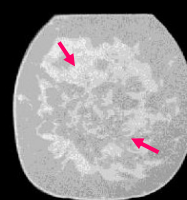
Source



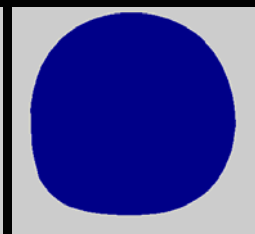
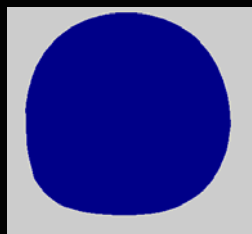
Target1



Target2

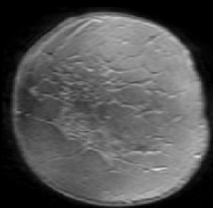


	Target1	Target2
CNR	3.0	3.5
QRS	97.6%	96.9%

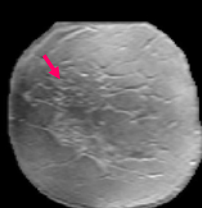


MR breast slice - simulation

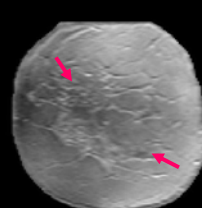
Source



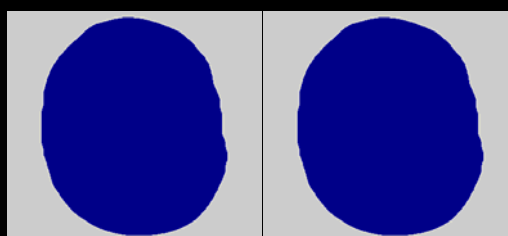
Target1



Target2

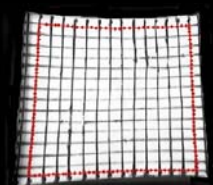


	Target1	Target2
CNR	20.0	5.7
QRS	100%	99.8%

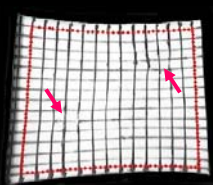


Two inclusion membrane

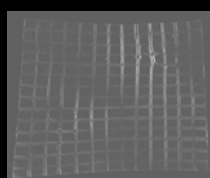
Source



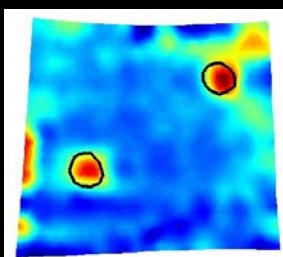
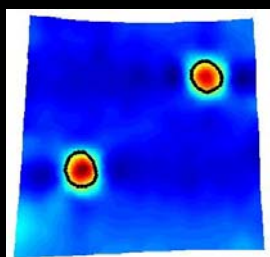
Target



Diff



CNR	2.8
QRS	88.5%



Summary

- Modality independence via simulation for handling various data types
- Multi-resolution approach potentially improves optimization convergence
- Two small stiff inclusions reconstructed in phantom membrane experiment
- Detectability accomplished via CNR
- Localization successful as evaluated by QRS

Acknowledgments

- BML/SNARL
Richard Chen
Prashanth Dumpuri
- John Boone, PhD (CT data)
- Tom Yankeelov, PhD (MR data)
- Whitaker Foundation
- CDMRP/BCRP Pre-doctoral Fellowship

<finis>

Future Directions / Research Questions

- Biological tissues are not typically linearly elastic
- Need for accurate boundary conditions creates dependence on segmentation methodology
- Not all data sets necessarily contain sufficient information for elastographic reconstruction

PRELIMINARY TESTING OF SENSITIVITY TO INPUT DATA QUALITY IN AN ELASTOGRAPHIC RECONSTRUCTION METHOD

Jao J. Ou, Stephanie L. Barnes, Michael I. Miga

Vanderbilt University, Department of Biomedical Engineering, Nashville, TN 37235
 {jao.ou,steph.barnes,michael.i.miga}@vanderbilt.edu

ABSTRACT

An elastographic reconstruction method has been developed to recover the material properties of soft tissue by model-based analysis of image data acquired at different states of mechanical loading. The algorithm utilizes image similarity as part of the cost function for a multi-resolution, non-linear optimization. Previous work with a phantom membrane used for simulated dermoscopic application has prompted this preliminary investigation of the relative effects of additive image noise and boundary condition determination errors on the performance of the method. The results as quantified by elasticity contrast and localization accuracy indicate that the reconstruction process is robust in the presence of realistic levels of image corruption and tolerates the majority of boundary condition mapping errors.

determine a spatial mapping of tissue elasticity, this process can also be classified as an inverse problem.

Our observations during the ongoing development and testing of this method have prompted questions concerning the quality of data necessary and sufficient to achieve satisfactory results (i.e. fidelity of the reconstructed elasticity image). The primary inputs to the reconstruction method are the acquired images and the delineated boundary conditions on the region of interest. While it is clearly preferable to have idealized data, in reality, both inputs involve varying levels of manual interaction. As an initial study, we have sought to test the effects of degradation in data quality on the end reconstruction by using additive image noise and randomized boundary condition selection error.

2. METHODS

1. INTRODUCTION

The practice of palpating soft tissue structures in the course of the physical exam for assessing tissue health has had a long-standing clinical history of providing correlation between improper stiffness and pathology. The ability to characterize the mechanical properties of tissue is therefore a potential source of information relevant for both diagnosis and prognosis. One way in which this could be achieved in a non-invasive manner is through analysis of tissue deformation with imaging and image processing techniques, which is a central goal of the field of elastography [1].

The conceptual framework for our elastographic reconstruction has been previously described in [2-4]. In brief, images of a tissue of interest are acquired in an initial (*source*) and then mechanically loaded state (*target*). The source image is deformed by a prescribed computational model and compared to the target. This is repeated in an iterative process using updates to the elasticity parameters of the model as generated by a multi-resolution, non-linear optimization scheme in order to achieve a suitable match in image similarity. Because the goal of the reconstruction is to

2.1. Elastographic Reconstruction Framework

There are three major components in the reconstruction framework: a biomechanical model of tissue response to applied deformation, a method of image comparison, and an optimization scheme. For the current version, a continuum-based model of mechanical equilibrium using isotropic Hookean linear elasticity with a plane stress approximation is employed [5]. This allows for a reduction of the general 3D formulation of Cauchy's Law to the two parameters of Young's modulus and Poisson's ratio in 2D. The displacement solution of the finite element representation of the model, solved using the standard Galerkin method of weighted residuals [6], is then applied to the nodes of a simple triangular mesh based on the source image domain in order to perform image deformation. The mesh is partitioned by K-means clustering (MATLAB R14, Mathworks, Nattuck, MA) into N number of *regions*, each of which describes a distinct set of homogeneous elastic properties for a grouping of adjacent elements. This allows for implementation of the multi-resolution approach by creating a hierarchy of increasingly finer spatial distributions of elasticity parameters, which has been shown to be an improvement upon previous versions using only a

single resolution [2,3]. A second discretization is performed to divide the target image into M number of rectangular *zones* containing approximately equal numbers of pixels. The deformed source image is compared to the target using an intensity-based image similarity metric (here, the correlation coefficient [7]) in the evaluation of the least squares error objective function

$$\sum_{m=1}^M (S_{TRUE} - S_{EST})^2 \quad (1)$$

where S_{TRUE} is an $M \times 1$ vector of the (maximum) similarity values achieved when comparing the target image to itself and S_{EST} is the $M \times 1$ vector of similarity between the target and model-deformed source image created using current estimates of the elastic modulus distribution. It should be noted that S_{TRUE} has by definition a value of 1 for the correlation coefficient.

The minimization of equation (1) using a Levenberg-Marquardt approach takes the form

$$[J^T J + \alpha I] \Delta E = [J^T] [S_{TRUE} - S_{EST}] \quad (2)$$

where \mathbf{J} is the Jacobian matrix of size $M \times N$ estimating $\partial S / \partial E$, ΔE is the $N \times 1$ vectors of updates to the current elasticity values, and α is the scalar regularization term for the Hessian matrix as described in [8].

2.2. Material Preparation and Image Acquisition

For our simulation purposes, a two-material skin phantom had been previously constructed [2] as a thin membrane measuring 15 cm x 15 cm, with a single 5-cm circular stiff inclusion embedded in the center (Figure 1). The phantom was manufactured with Smooth-On™ polyurethanes (Smooth-On, Easton, PA) Evergreen 10 and Evergreen 50. These materials have essentially indistinguishable colors but vary significantly in their elastic modulus values, so the former was used as the bulk material and the latter for the inclusion. Based on material testing, the expected contrast ratio of Young's modulus values was determined to be approximately 5.7:1. A black permanent marker was used to place a pattern of regularly spaced (~1 cm) grid lines on the membrane. The membrane was clamped along two opposite edges and then stretched in a uniaxial fashion by means of a milling vise. A commercial webcam (Logitech QuickCam Pro 4000) was mounted above the assembly to acquire image pairs of the membrane in pre- and post-stretched states (960 x 1280 pixel resolution, 8-bit grayscale).

2.3. Reconstruction Experiments

Based on prior work, a data set consisting of a particular image pair and associated boundary conditions

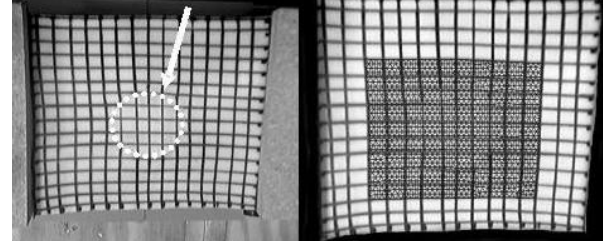


Figure 1. Experimental phantom membrane system (left) and input image with overlaid finite element mesh (right). The inclusion location is indicated by the arrow and dotted line. The mesh designates the actual region reconstructed.

known to produce a satisfactory reconstruction was designated as the gold standard for the remainder of the experiments (Figure 1). In order to test the effect of increasing amounts of additive noise on the reconstruction algorithm, Gaussian random fields of 1, 5, 10, 15, 20, 25, and 30% noise were applied to the base target image in three separate trials. This presents a challenge that ascertains the ability of the similarity metric and objective function to discern a proper match.

The current method for selecting Dirichlet boundary conditions on the finite element mesh is semi-automated and requires the user to make a final determination on point correspondence. The second experiment was intended to simulate the targeting error of the user (e.g. visual cues and input device control). Each test involved applying randomized vectors of equal magnitude to alter the boundary conditions of the gold standard data set. Errors of 0.1, 0.2, 0.3, 0.5, 0.75, 1.0, 1.5, and 2.0 mesh units (scaled to be equivalent to pixel coordinates) were used in two separate trials for a total of 16 reconstructions. Sub-pixel magnitudes were included after determining that the accuracy of selecting a feature point in the image/mesh was typically less than or equal to 0.5 units for users ranging from moderate to expert skill.

For all reconstructions, resolutions progressing through $N = 16, 36, 64, 144, 256$, and 400 regions and $M = 9$ similarity zones were used; domains were initialized to homogeneous elasticity and Poisson's ratio held constant at 0.485 to represent nearly incompressible material(s).

2.4. Reconstruction Analysis

The final reconstructed elasticity values were modeled as a mixture of two Gaussian distributions, and a threshold was established to maximize inter-class variation [9] and subsequently classify each region as bulk or stiff material. Because Dirichlet boundary conditions are exclusively used in these reconstructions, the method is only sensitive to relative differences in elasticity. The quantities used in evaluating reconstruction success are the elasticity contrast ratio, localization accuracy of the inclusion, and an overall measure designated the 'quality of reconstruction score' (QRS). The elasticity contrast ratio (CR) was calculated

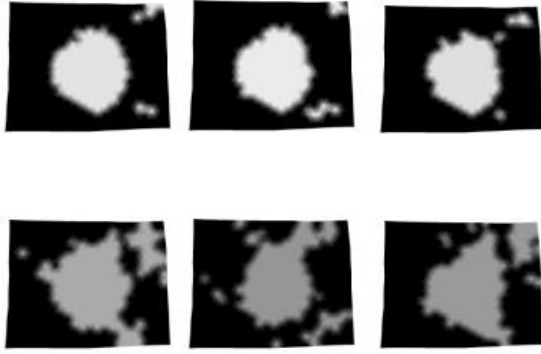


Figure 2. Representative reconstructions with image noise. From top left: 1, 5, 10, 20, 25, and 30% additive Gaussian noise. The reconstructions are visualized as two materials, with whiter areas indicating higher elasticity contrast values.

Table 1. Reconstruction quality under noise conditions

Additive image noise								
% Noise	1	5	10	15	20	25	30	
LA	0.92	0.90	0.91	0.70	0.69	0.66	0.56	
CR	3.56	3.45	3.45	3.24	2.88	2.83	2.68	
Gold standard: LA = 0.95, CR = 3.60								
Boundary condition error								
Err	0.1	0.2	0.3	0.5	0.75	1.0	1.5	2.0
AE	0.96	3.32	2.21	102	0.93	32.2	12.6	7.66
LA	0.87	0.92	0.88	0.59	0.94	0.86	0.86	0.96
CR	3.63	3.68	3.44	2.91	3.46	3.71	3.78	3.30
CR = elasticity contrast ratio, LA = localization accuracy								
AE = initial alignment error (%), Err = error magnitude.								

from the mean values of the two material classes, and the positive predictive value of identifying stiff material within the independently segmented boundary of the inclusion gives a measure of localization accuracy (LA). The quality of reconstruction is simply then the product $QRS = CR \cdot LA$, which allows the user to consider the other two measures in conjunction.

3. RESULTS

Figures 2 and 3 show examples of reconstructions achieved under various image noise and boundary condition errors, and individual localization errors and contrast ratio values are listed in Table 1. Note that the data for the image noise experiment was averaged from the three trials, and that the data presented for the boundary condition experiment is from one [representative] trial. Figure 4 is a plot of the reconstruction quality decreasing with increasing image noise, and Figure 5 shows the reconstruction quality trend plotted against the change in initial alignment error (detailed in the following section) relative to that of the gold standard.

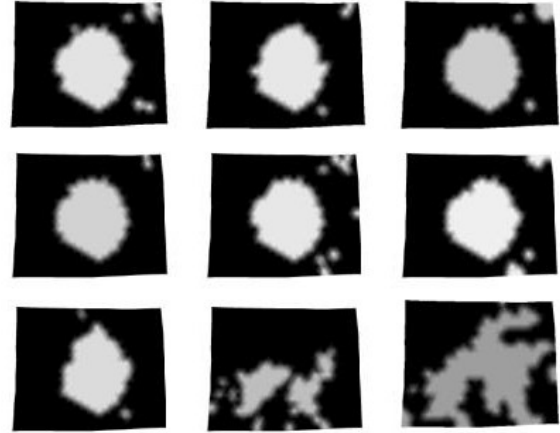


Figure 3. Representative reconstructions with boundary condition error. Left to right: 0.1, 0.2, 0.3 units (top row); 0.75, 1.0, 2.0 units (middle row, trial #1); 0.75, 1.0, 2.0 units (bottom row, trial #2). Error magnitudes greater than or equal to 0.5 mesh units are not accurate predictors of reconstruction quality.

4. DISCUSSION

From visual inspection of Figure 2, it is apparent that the achieved reconstruction becomes more inaccurate with increased image noise. However, the ability to identify and localize the stiff inclusion is not significantly impaired until a noise field of greater than 10% is applied. The threshold was found by determining which level of noise provided the best minimum sum squared error fit of two lines to the distribution of reconstruction quality in Figure 4. This would indicate that the similarity metric and objective function are robust to intensity deviations of about 6 gray levels. While Gaussian noise is one of several possible types and may not always be an ideal model, it is still relevant to acquisition inaccuracy and corruption processes that may be encountered across several medical imaging modalities. The use of an intensity-based similarity metric appears to give the method an advantage in being generally insensitive to reasonably expected amounts of image noise.

Figure 3 demonstrates that because of the random nature of the boundary condition errors, the magnitude is itself not an accurate indicator of reconstruction quality. This necessitated the introduction of a more suitable parameter that accounts for the net effect of the altered boundary conditions in order to perform fair evaluations. In essence, randomizing the vectors at every node causes the optimization to use an unpredictable starting pose and increases its chance of converging to an improper minimum. Therefore, the ‘initial alignment error’ (AE) is defined as the relative percent change between the objective function evaluation using the gold standard boundary conditions and those of the test case. An example, it could be assumed that vectors of magnitude 0.5 would be a much more tolerable error than 2.0, but it is the significantly larger AE

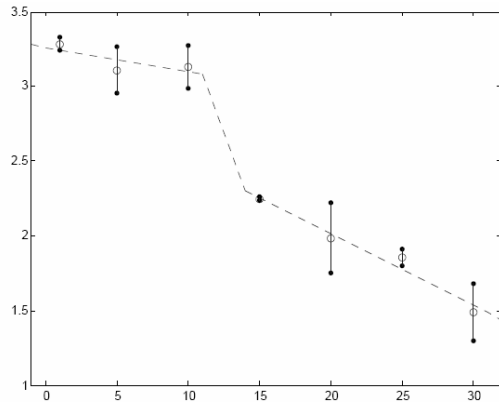


Figure 4. Reconstruction quality vs. percent additive image noise. The drop-off after 10% additive noise indicates the threshold of tolerance for the method.

of the former that actually predicts the poor outcome. However, it should also be noted (results not shown here) that even if the same set of error vectors are scaled over varying magnitudes, there is no clear trend in alignment error or reconstruction quality. This appears to imply that certain boundary nodes, most likely those in the direction of largest strain, have a greater effect on reconstruction and merit particular care in selection. Other factors influencing unfavorable reconstructions are most likely nonlinear effects not predicted by the current model as well as an inherent lack of discrimination by intensity-based similarity metrics in analyzing the regularity of the imposed grid pattern. Nevertheless, for the error magnitudes tested that best approximate realistic inaccuracies (i.e. <0.5 units), the alignment errors were small and quality of the end reconstruction was seen to be quite good. This qualitatively validates the current method of determining point correspondence as a reasonable procedure with an accommodating margin (factor of four) in light of typical user interaction.

5. CONCLUSIONS

In this work, we have presented a method for recovering elasticity parameters from image data of thin membrane structures by maximizing the image similarity between two different states of mechanical loading within the context of an inverse problem. The biomechanical model, multi-resolution optimization, and image acquisition are each modular components of this elastographic reconstruction framework, making it extensible to added sophistication. Tests were conducted to examine the tolerance of the method to degraded or improper inputs. The results indicate that the gold standard data set was mostly optimal for obtaining a successful reconstruction. Widening disparities in either image data or boundary condition selection from that in the gold standard caused observable trends of declining reconstruction quality. Based on these observations, it appears that the method handles most

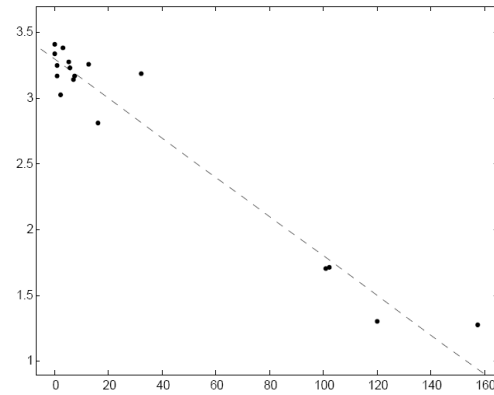


Figure 5. Reconstruction quality vs. percent change in initial alignment relative to gold standard. The majority of errors tested produced satisfactory reconstructions.

expected variations encountered in image acquisition as well as the majority of typical user inaccuracies. Because there are complicated effects associated with mapping of the Dirichlet boundary conditions in constraining the displacement solution of the model, further study on inter-rater variability in selection as well as comparisons with more automated point correspondence methods is ongoing.

Acknowledgements This work was supported in part by a Whitaker Foundation Young Investigator Continuation Award and the Congressionally Directed Medical Research Program – Breast Cancer Research Program Pre-doctoral Fellowship.

6. REFERENCES

- [1] J. Ophir, I. Cespedes, H. Ponnekanti, Y. Yazdi, and X. Li, "Elastography - a quantitative method for imaging the elasticity of biological tissues," *Ultrasonic Imaging*, vol 13, pp. 111-134, 1991.
- [2] M.I. Miga, M.P. Rothney, J.J. Ou, "Modality-independent elastography (MIE): potential applications for dermoscopy," *Medical Physics*, vol 32 pp. 1308-1320, 2005.
- [3] C.W. Washington, M.I. Miga, "Modality independent elastography (MIE): a new approach to elasticity imaging," *IEEE Trans Med Imaging*, vol 23, pp. 1117-1128, 2004.
- [4] M.I. Miga, "A new approach to elastography using mutual information and finite elements," *Phys Med Biol*, vol 48, pp. 467-480, 2003.
- [5] Boresi, A., *Elasticity in Engineering Mechanics*, Wiley-Interscience, 2000.
- [6] Lapidus, L., and G.F. Pinder, *Numerical Solution of Partial Differential Equations in Science and Engineering*, John Wiley & Sons, 1982.
- [7] Fitzpatrick, J.M., Hill, D.L.G., and C.R. Maurer, "Image registration," *Handbook of Medical Imaging, Volume 2*. SPIE Press, pp. 447-513, 2000.
- [8] N. Joachimowicz, C. Pichot, J.P. Hugonin, "Inverse scattering: an iterative numerical method for electromagnetic imaging," *IEEE Trans Biomed Engineering*, vol 39, pp. 1742-1752, 1991.
- [9] N. Otsu, "A threshold selection method from gray-level histograms," *IEEE Trans Syst Man Cybern*, vol 9, pp. 62-66, 1979.



PRELIMINARY TESTING OF SENSITIVITY TO INPUT DATA QUALITY IN AN ELASTOGRAPHIC RECONSTRUCTION METHOD

Jao J. Ou, Stephanie L. Barnes, and Michael I. Miga

Vanderbilt University, Department of Biomedical Engineering, Nashville, TN 37235



BACKGROUND

Changes to the local cytoarchitecture induced in a variety of pathologies can manifest as alterations in tissue elasticity that are relevant in clinical examination and evaluation. Many elastography methods are typically dependent on the specific modality around which they were developed (e.g. magnetic resonance and ultrasound imaging). We have developed 'modality-independent elastography' (MIE) as a reconstruction method that recovers the material properties of soft tissue via model-based analysis of image data acquired at different states of mechanical loading. The algorithm utilizes image similarity in the performance of a multi-resolution, non-linear optimization. Previous work with a phantom membrane used for simulated dermoscopic applications prompted this preliminary investigation of the relative effects of additive image noise and boundary condition determination errors on the performance of the method. The results as quantified by elasticity contrast and localization accuracy indicate that the reconstruction process is robust in the presence of realistic levels of image corruption and tolerates the majority of boundary condition mapping errors.

PURPOSE

The inputs to the reconstruction process are in two major forms: image data and boundary condition estimation. Inadequate fidelity in either quantity is capable of affecting the success of the reconstruction through some form of model-data mismatch. We proposed to test the sensitivity of the algorithm to various levels of an applied noise process by altering either the intensity distribution of the target image or the displacement vectors defining the Dirichlet boundary conditions.

METHODS

Figure 1. Flow chart of MIE. After acquisition, source and target images (A) are discretized into regions and zones, respectively. The reconstruction process involves updating elastic modulus values (B,E) to drive a finite element model-based image deformation (C) until the best match is found (D).

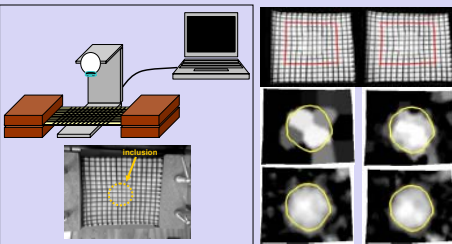
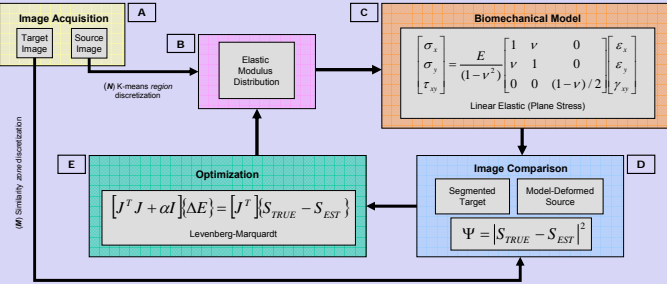


Figure 2. MIE reconstruction experiment.

(Left panel) A two-material phantom mimicking skin was constructed as a thin membrane measuring 15 cm x 15 cm, with a single 5 cm circular stiff inclusion embedded in the center. The phantom was manufactured with like-colored polyurethanes which have an inclusion-to-bulk elasticity contrast of approximately 5:1. The membrane was stretched in a uniaxial fashion while a CCD camera mounted above acquired image pairs of the membrane in pre- and post-deformed states (960 x 1280 pixel resolution, 8-bit grayscale).

(Right panel) Top row: Source and target images with overlay of finite element mesh boundaries (red) that demarcate the area reconstructed. Below: Reconstruction progression over increasing number of regions ($N = 16, 64, 256, 400$) to refine the spatial distribution of elasticity values. This reconstruction serves as the gold standard for the remainder of this work.

RESULTS

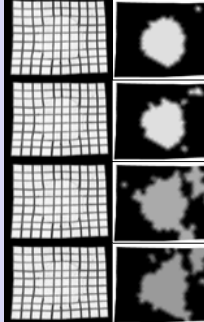


Figure 3. MIE image noise reconstruction experiment.

Gaussian random fields of variable strength with respect to the variance of non-background pixel values were applied in an additive fashion to the target image. Shown in the left column from top to bottom are the original target and then with 10%, 20%, and 30% noise. In the right column are the corresponding elasticity reconstructions after application of a thresholding scheme to classify bulk (black) and inclusion materials (white/gray). The known segmentation of the inclusion was used to retrospectively calculate the positive predictive value of identifying the correct material type within the proper boundaries as well as the mean elasticity contrast of the overall distribution. For this work, our overall evaluation of reconstruction quality is expressed as the product of these two quantities. The effect of additive noise is to decrease reconstruction quality as evidenced in the progressively poorer localization of the inclusion.

Figure 4. MIE boundary condition noise reconstruction experiment.

Randomized vectors of a particular magnitude were applied to the boundary condition specifications of the same finite element mesh used for all reconstructions. This simulates targeting error by the user in the currently semi-automated method of point correspondence selection, and the effect is illustrated in the top row from left to right, the gold standard boundary and then with mis-estimation of 0.75, 1.0, and 2.0 mesh units (equivalent to pixel coordinates) in the Dirichlet conditions (slightly exaggerated scale for visual effect). The corresponding reconstructions in the middle and bottom rows demonstrate that two different trials using the same magnitude of randomized vectors can effect very different levels of reconstruction quality.

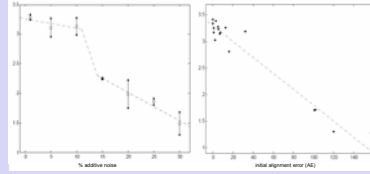
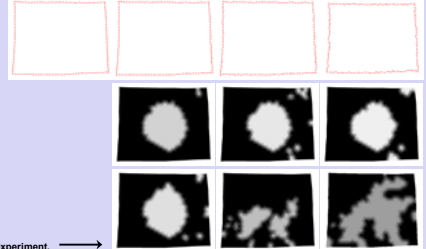


Figure 5. Reconstruction quality vs. image noise.

Three trials of image noise were performed (shown averaged and with standard error bars); the drop-off in reconstruction quality indicates the presence of a threshold at approximately 10% additive Gaussian noise.

Figure 6. Reconstruction quality vs. boundary condition noise.

Two trials of eight levels of noise ranging from 0.1 to 2.0 mesh units were performed. Each reconstruction was treated as a separate data point based on its initial alignment error, defined here as the relative change between the objective function evaluation using the gold standard boundary conditions and those of the (randomized) test case.

DISCUSSION

Figures 3 and 5 show that the achieved reconstruction becomes more inaccurate with increased image noise. However, the ability to identify and localize the stiff inclusion is not significantly impaired until a noise field of greater than 10% is applied. The threshold was found by determining which level of noise provided the best minimum sum squared error fit of two lines to the distribution of reconstruction quality. This would indicate that the similarity metric and objective function are robust to intensity deviations of about 6 gray levels in an 8-bit image. While Gaussian noise may not always be an ideal model, as a preliminary point of investigation, it is still relevant to acquisition inaccuracy and corruption processes that can be encountered across several medical imaging modalities.

Figure 4 demonstrates that the magnitude of the random vectors is itself not an accurate indicator of reconstruction quality because the multiple degrees of freedom afforded by the boundary nodes cause the optimization to use an unpredictable starting pose, increasing the chances of converging to an improper local minimum. This necessitated the introduction of the initial alignment error (AE) to provide a consistent means of comparison between trials (Figure 6). As a further example, it could be assumed that vectors of magnitude 0.5 would be a much more tolerable error than 2.0, but it is the significantly larger AE of the former that actually predicts the poor outcome. It should also be noted (results not shown here) that even if the same set of error vectors are scaled over varying magnitudes, there is no clear trend in alignment error or reconstruction quality. This appears to imply that certain boundary nodes, most likely those in the direction of largest strain, have a greater effect on reconstruction and merit particular care in selection. Nevertheless, for the error magnitudes that approximate inaccuracy in boundary condition demarcation (i.e. <0.5 units), the quality of those reconstructions was satisfactory. This qualitatively validates the current method of determining point correspondence as a reasonable procedure with an accommodating margin (factor of four) in light of typical user interaction. Further research is ongoing into validation and control of boundary conditions, as well as more automated methods of point correspondence.

REFERENCES

- M.I. Miga, M.P. Rothney, J.J. Ou, "Modality-independent elastography (MIE): potential applications for dermoscopy," *Medical Physics*, vol 32 pp. 1308-1320, 2005.
- M.I. Miga, "A new approach to elastography using mutual information and finite elements," *Phys Med Biol*, vol 48, pp. 467-480, 2003.
- N. Joachimowicz, C. Pichot, J.P. Hugonin, "Inverse scattering: an iterative numerical method for electromagnetic imaging," *IEEE Trans Biomed Engineering*, vol 39, pp. 1742-1752, 1991.
- N. Otsu, "A threshold selection method from gray-level histograms," *IEEE Trans Syst Man Cybern*, vol 9, pp. 62-66, 1979.

This work was supported in part by a Whitaker Foundation Young Investigator Award and a Congressionally Directed Medical Research Program Breast Cancer Research Program Pre-doctoral Fellowship.

Automatic surface correspondence methods for a deformed breast

Daniel R. Schuler III, Jao J. Ou, Stephanie L. Barnes, Michael I. Miga
 Department of Biomedical Engineering, Vanderbilt University, VU Station B #351631,
 Nashville, TN, 37235-1631
 {daniel.r.schuler, jao.ou, steph.barnes, michael.i.miga*}@vanderbilt.edu
 {*corresponding author}
 Phone: 615-343-8336 Fax: 615-343-7919

ABSTRACT

A significant amount of breast cancer research in recent years has been devoted to novel means of tumor detection such as MR contrast enhancement, electrical impedance tomography, microwave imaging, and elastography. Many of these detection methods involve deforming the breast. Often, these deformed images need to be correlated to anatomical images of the breast in a different configuration. In the case of our elastography framework, a series of comparisons between the pre- and post-deformed images needs to be performed. This paper presents an automatic method for determining correspondence between images of a pendant breast and a partially-constrained, compressed breast. The algorithm is an extension to the symmetric closest point approach of Papademetris et al. However, because of the unique deformation and shape change of a partially-constrained, compressed breast, the algorithm was modified through the use of iterative closest point (ICP) registration on easily identifiable sections of the breast images and through weighting the symmetric nearest neighbor correspondence. The algorithm presented in this paper significantly improves correspondence determination between the pre- and post-deformed images for a simulation when compared to the original Papademetris et al.'s symmetric closest point criteria.

Keywords: deformation, registration, finite element, breast cancer, elastography, soft-tissue mechanics

1. INTRODUCTION

In a 2001 report released by the American Cancer Society, a woman in the United States had a 1 in 8 lifetime risk of developing breast cancer, and these odds increased depending on factors such as age, family history, ethnicity, and genetic predisposition. It also presented statistics illustrating the strong connection between survival rate and stage of cancer development at diagnosis (localized (96.4%), regional (77.7%), and distant (21.1%))*[1]. Given the obvious benefits of extended lifetime with early diagnosis, there has been a resultant push to increase the sensitivity and specificity of current imaging methods and modalities. However, in addition to improving upon current tumor-detection methodologies, much recent research has been devoted to novel imaging techniques devised to supplement diagnosis.

Many of these new techniques are based upon the exploitation of constitutive properties of tissue, e.g. electrical, optical, or stiffness properties. The differences between healthy and cancerous tissue with regards to these properties has been investigated to varying degrees for a number of years and suggested results have been forthcoming [2-4]. Currently, the use of the differences in these properties as a tumor detection method can be seen through microwave imaging [5], electrical impedance tomography (EIT) [6], near-infrared tomography [3], ultrasound elastography (USE), magnetic resonance elastography (MRE), and, most recently, in modality independent elastography (MIE) [7]. Many of these detection methods, particularly elastography, involve deforming the breast and comparing the pre- and post-deformed images of the breast. In addition, there are other methods whereby deformations occur due to repositioning of the patient as in MR contrast enhancement [8].

The purpose of this paper is to present an algorithm that automatically determines correspondence between images of the pendant and deformed breast geometry. This algorithm is based on the symmetric nearest neighbor algorithm presented by Papademetris et al. [9]; however, the algorithm presented in this paper uses certain geometric characteristics of the breast to improve upon the accuracy of Papademetris et al.'s method. Due to the unique deformation and shape

* These statistics represent the 5-year survival rate.

change of a partially-constrained, compressed breast, the algorithm was modified through the use of iterative closest point (ICP) registration on easily identifiable sections of the breast images, and it included weighting the symmetric nearest neighbor correspondence. The work presented here has implications within the modality independent elastography method presented by Miga et al. [7, 10] as well as for the multi-modal registration among alternative imaging techniques for breast cancer.

2. MATERIALS AND METHODS

2.1. Breast surface correspondence algorithm

A model of a human breast is generated in the pendant position based on breast CT data (courtesy of John M. Boone, Ph.D., Professor of Biomedical Engineering, University of California at Davis [11-12]). Using a finite element model, a deformation simulating the inflation of a membrane pressing against the breast is performed, creating a deformed breast geometry. Correspondence between point clouds of the pendant breast and the compressed breast is performed using a multi-step procedure based on the symmetric closest point algorithm of Papademetris et al. The algorithm was modified such that easily identifiable regions are constrained using an iterative closest point (ICP) registration to initially establish correspondence. End correspondence of a point is still partially determined by its neighbors' correspondence. Thus, the algorithm consists of four main steps: ICP registration of the base and nipple regions of the breast, the initial correspondence determination by symmetric nearest neighbors, the "propagating front" of the correspondence through the remaining points in the point cloud, and the final smoothing and mapping of the correspondence.

For purposes of simplicity, the following nomenclature will be used in describing the algorithm: the point cloud that defines the pendant breast is the source point cloud, s_1 , and the point cloud that defines the partially-constrained, compressed breast is the target point cloud, s_2 . Also, a "faux registration" of s_1 to s_2 means that the rotation and translation matrices necessary to ICP register s_1 to s_2 are known, but the actual registration of s_1 to s_2 does not take place. Furthermore, the algorithm is constructed for a super-sampled target point cloud.

2.1.1. Initial correspondence via ICP partial volume registration

The purpose of this step is to use the more prominent geometric characteristics of the breast and the fixation of the breast at the chest wall, namely the regions around the nipple and the base of the breast, as a location for accurately determining initial correspondence. However, due to the compression, the nipple of the deformed breast (the target point

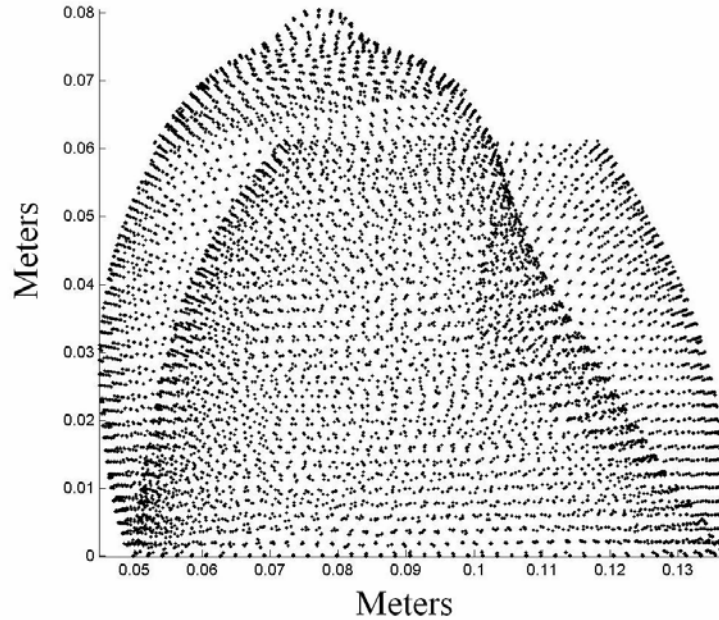


Figure 1: Point clouds of the deformed and pendant breast, with the top 20% of the pendant breast registered to the deformed breast according to the rotation and translation matrices provided from a faux registration of the top 46.25% of the breasts.

cloud) is translated and lies at a different angle than the nipple of the pendant breast (the source point cloud). By minimizing the average distance from the points in the nipple region on the registered source point cloud to the points in the nipple region on the target point cloud, the nipple regions of the pendant and deformed breast are most accurately aligned. (The average distance means the average Euclidean distance between a point on the source point cloud and its closest point on the target point cloud.) For the nipple region registration (which the nipple region is assumed to reside at the upper 20% of the breast's height), there exists a certain height percentage, ψ , such that if all points of the pendant breast at or above ψ were faux registered to all of the points of the deformed breast at or above ψ , then the resultant rotation and translation matrices would minimize the distance between nipple regions of the pendant and deformed breast. This height percentage, ψ , is determined as follows: a binary search algorithm faux registers a range of height percentages, from the upper 50% to the upper 20% of the breast height. The algorithm then compares the average distance between the nipple regions for the rotation and translation matrices produced by the faux registration. The height percentage that produces the minimal distance between nipple regions is designated ψ . Finally, by using the rotation and translation matrices defined by the registration of the ψ percentage, the nipple region of the source point cloud is registered to the nipple region of the target point cloud (see Figure 1), and initial correspondence between the point clouds can now take place. This process is repeated for the base regions (i.e. the lower 5% of the breast height) of the source and target point clouds.

2.1.2. Symmetric nearest neighbor correspondence

Initial correspondence is restricted to the registered regions of the point clouds (the nipple and base regions). Correspondence is achieved through a method Papademetris et al. coined "symmetric nearest neighbor." For a point p_1 on the source point cloud s_1 , the closest point to p_1 on the target point cloud s_2 is p_2 . In other words, p_2 is chosen such that the distance from p_1 to p_2 is the shortest Euclidean distance possible when compared to the Euclidean distance between p_1 and any other point on s_2 . p_2 then determines its closest point on s_1 to be P . If $p_1 = P$, then the points p_1 and p_2 are corresponding and called symmetric nearest neighbors. The vector from p_1 to p_2 is called a corresponding vector.

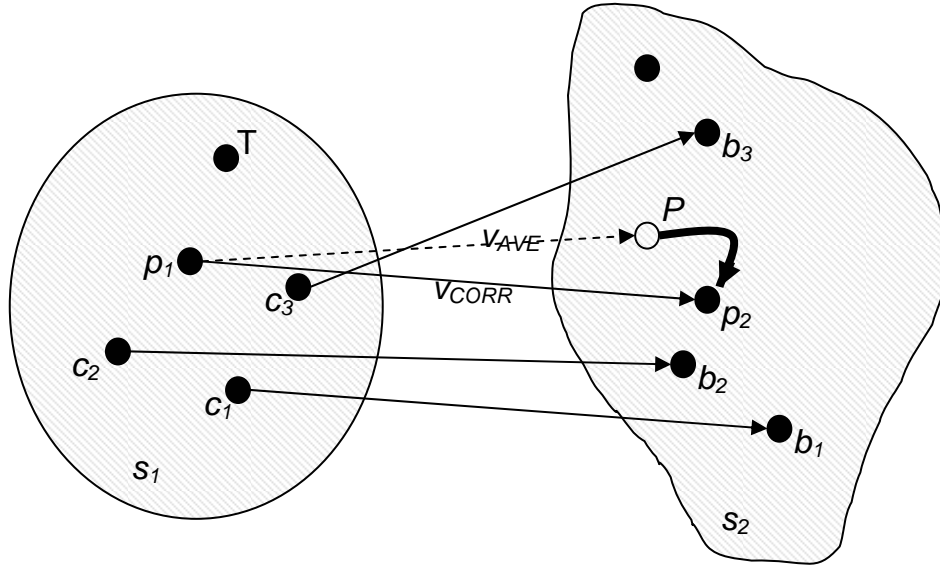


Figure 2: Simple diagram of a "propagating front" of correspondence. The weighted average of the symmetric closest point vectors from c_1, c_2, c_3 to b_1, b_2, b_3 create v_{AVE} . p_1 is a point that does not have correspondence. P is created by projecting along v_{AVE} from p_1 , and the closest point p_2 to P becomes p_1 's corresponding point (with corresponding vector v_{CORR}). Correspondence then bleeds to T , which now uses v_{CORR} in the creation of its weighted average vector.

2.1.3. "Propagating front" of correspondence

Correspondence then continues to be established using a "propagating front" methodology in which points on the source point cloud that have neighbors with a high degree of correspondence are the first candidates for establishing

correspondence, as shown in Figure 2. For point p_1 on s_1 , the first- and second-order neighboring points of p_1 in s_1 that already have correspondence are c_1, c_2, \dots, c_n (points b_1, b_2, \dots, b_n are the corresponding points of c_1, c_2, \dots, c_n on the target point cloud s_2 , and their corresponding vectors are v_1, v_2, \dots, v_n). An average of the corresponding vectors v_1, v_2, \dots, v_n weighted by the distance of c_1, c_2, \dots, c_n to p_1 , is then computed and is denoted v_{AVE} . A temporary point, P , is then projected by v_{AVE} from p_1 , and the closest point (as determined by Euclidean distance) on s_2 to P is p_2 . p_2 is the corresponding point for p_1 . The vector from p_1 to p_2 is the corresponding vector, v_{CORR} . p_2 can be any point in s_2 unless it is b_1, b_2, \dots, b_n . In this case, the next closest point to P on s_2 that is not b_1, b_2, \dots, b_n is the corresponding point to p_1 . This step will provide correspondence for every point in the source point cloud as long as there is at least one initial point correspondence between the source and target point clouds. The algorithm continues in an iterative fashion such that correspondence will be determined only for those points in s_1 with a maximum number of neighbors with correspondence.

2.1.4. Smoothing and mapping

After every point in the source point cloud has correspondence, the entire point cloud undergoes a smoothing and mapping to reach a final correspondence. Point p_1 of source point cloud s_1 has neighboring points c_1, c_2, \dots, c_n . Points c_1, c_2, \dots, c_n have corresponding points b_1, b_2, \dots, b_n in the target point cloud s_2 , and their corresponding vectors are v_1, v_2, \dots, v_n . An average of the corresponding vectors v_1, v_2, \dots, v_n , weighted by the distance of c_1, c_2, \dots, c_n to p_1 , is computed and denoted v_{AVE} . A temporary point, P , is then projected by v_{AVE} from p_1 , and the closest point (as determined by Euclidean distance) from s_2 to P is p_2 , which is the final corresponding point of p_1 .

2.2. Breast deformation simulation

In order to test the algorithm described above, a finite element (FE) model of a breast was generated based on a subject's CT image volume. The biomechanics of breast deformation was described using a three-dimensional linear elastic Hookean solid. Once the geometry was generated, boundary conditions were implemented that simulated the compression of the breast by an adjacent balloon inflation cuff. Figure 3 shows the geometry and the boundary conditions applied. Results from varying the strength of the stress field can be seen in Figure 4. Figure 4a shows the pre-post compression of the breast subject to the boundary conditions in Figure 3. Figure 4b and 4c represent different inflation states, 75% and 50% respectively. By using a finite element model, exact correspondence between source and target can be established and used to rate the algorithm performance. It should be noted though that the target cloud, i.e. deformed finite element breast mesh, was super-sampled to allow for more variability when executing the correspondence algorithm. In the clinical context, the point-cloud representations would represent two unique image acquisitions so a corresponding structured grid (as provide by the FE mesh) would not exist.

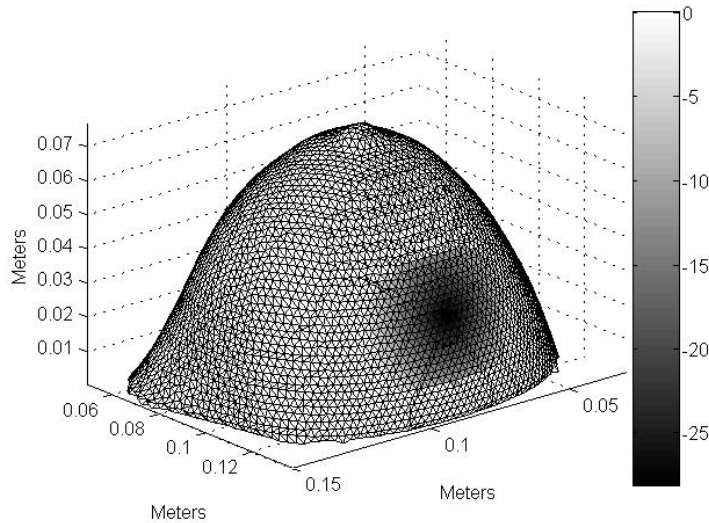


Figure 3. Finite element breast model with boundary conditions shown. Grayscale represents the application of a normal stress in kPa. The base of the volume was fixed.

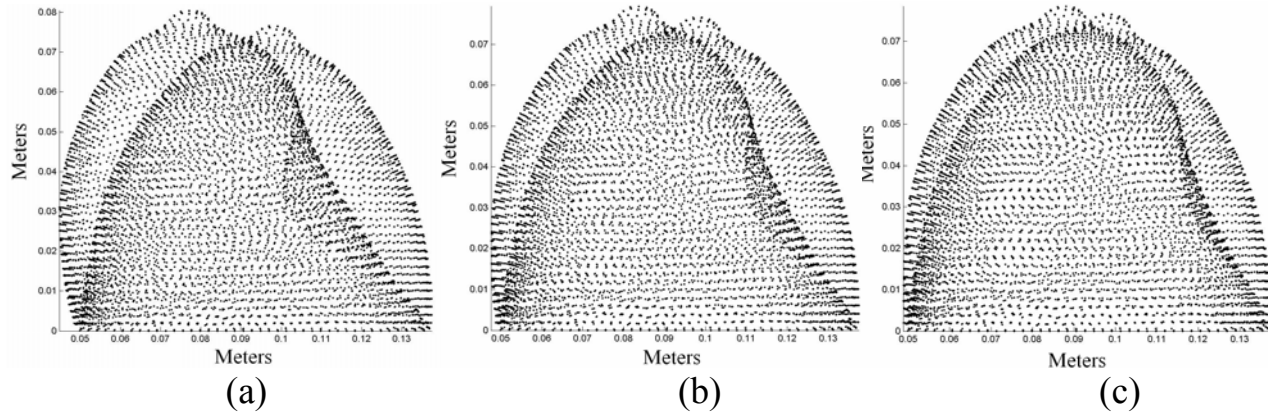


Figure 4: Pendant and deformed breast point clouds for a. 100% simulation b. 70% simulation and c. 50% simulation.

3. RESULTS

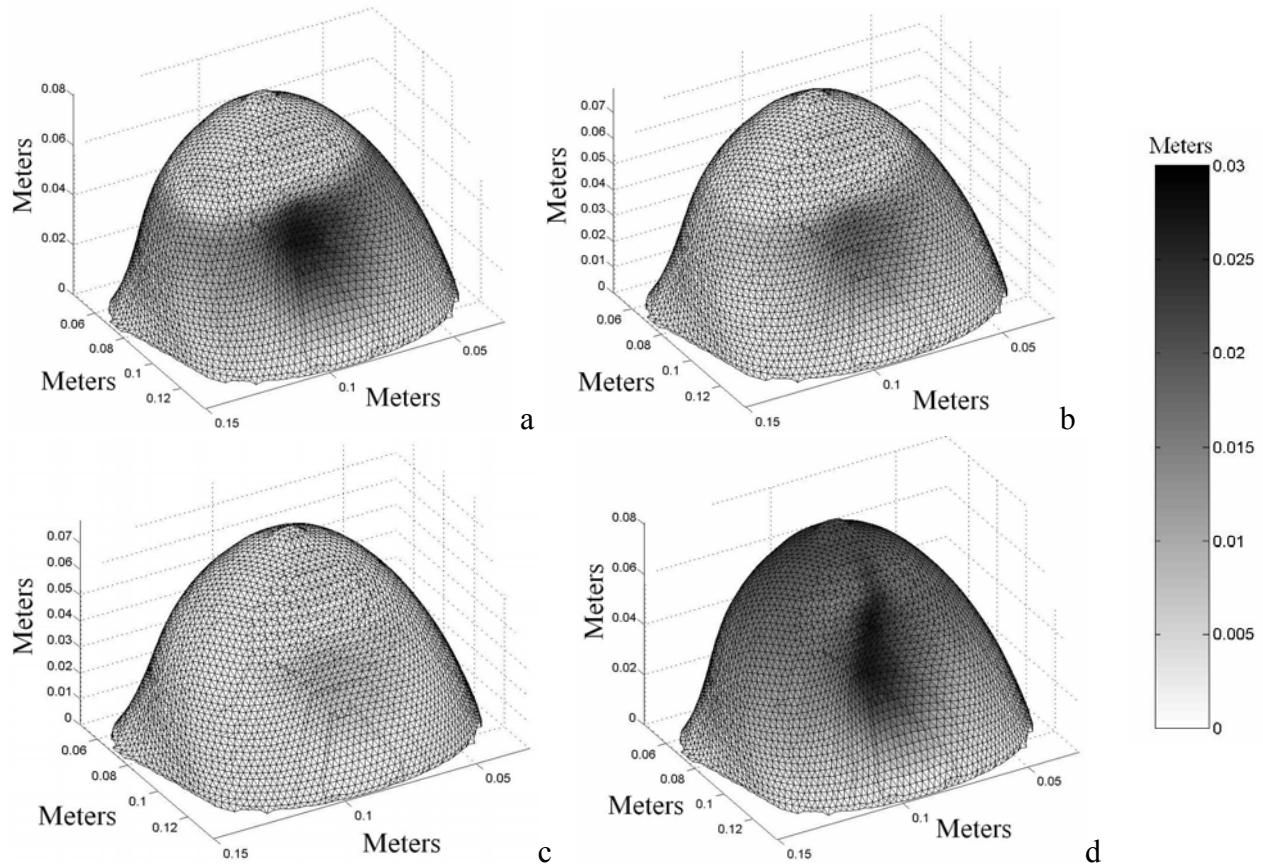


Figure 5. (a) Distribution of correspondence error using the proposed algorithm with the 100% deformation FE simulation. (b) Distribution of correspondence error with the 70% simulation. (c) Distribution of correspondence error with the 50% simulation. (d) Distribution of correspondence error for 100% deformation FE simulation using Papademetris et al.'s algorithm. Grayscale shown is common to all figures.

Figure 5a-c shows the result of running the various simulations through our algorithm while Figure 5d shows the result of running the 100% simulation with using solely the symmetric closest point criteria of Papademetris et al.'s algorithm. The shading of each deformed breast is root mean square (RMS) error of the distance from the predicted target corresponding point and the actual target corresponding point. Figure 6 compares the RMS error and maximum error (again, the distance from the predicted target corresponding point to the actual target corresponding point) of our algorithm versus the maximum displacement compression exerted on the breast for each simulation. Additionally, the maximum error for Papademetris et al.'s algorithm and the 100% simulation is 2.78 cm, and the RMS error is 1.02 cm.



Figure 6: Comparison of the maximum displacement in the depression of the breast to the RMS error (●) and the maximum error (■) for the 100% simulation (right points), 70% simulation (middle points) and 50% simulation (left points).

4. DISCUSSION

Figure 5a-c demonstrates that our algorithm, overall, assigns correspondence from the pendant to the deformed breast reasonably well, especially at less severe deformations. Figure 6 provides further support, demonstrating that the relatively low RMS error ranges from 1.2 mm for the 50% simulation to 6.0 mm for the 100% simulation. Furthermore, there is a linear relationship between degree of compression and the maximum and RMS error for our algorithm, with both errors decreasing as the degree of compression decreases. However, there is still error in the correspondence assignments, primarily at the site of compression. This error is due to the algorithm's inability to cope with the steep point translations associated with the depression; the algorithm continues to assign correspondence to the edge of the depression rather than penetrating into the depression. This suggests that further research into the incorporation of some other type of information into our algorithm is needed for greater accuracy. But, as evidenced by Figure 5d, our algorithm is significantly more accurate than the original Papademetris et al. algorithm. While the Papademetris et al. algorithm handles the depression approximately as well as our algorithm with a maximum error of 2.78 cm (compared to our algorithm's maximum error of 2.68 cm for the same simulation), the accuracy of the correspondence assignments continues to decrease up into the nipple region. This results in a RMS error of 1.02 cm, which is significantly higher than our RMS error of 6.0 mm. It should be noted though that only the symmetric closest point portion of the Papademetris et al. algorithm has been implemented. The algorithm in its entirety also utilizes a curvature mapping aspect for their particular application in cardiac deformation mapping. Usage of curvature information would not be useful for breast applications due to its geometrically homogeneous nature.

The main reason our algorithm is more accurate than just utilizing the symmetric closest point algorithm is due to the first step, the initial registration of the nipple and base regions, which constrains the search greatly. By rigidly registering the nipple and base regions, the initial pass of establishing correspondence is highly accurate. In the original algorithm, the initial pass of determining correspondence frequently was inaccurate (the entire point cloud was permitted to initially establish correspondence), particularly at the nipple region. Because the deformed breast's nipple was translated away from the pendant breast's nipple, correspondence was established between the far side of the pendant breast's nipple and the near side of the deformed breast's nipple as opposed to the far side of the deformed breast's nipple.

At this time, it needs to be noted that this paper's algorithm needs further study with respect to the number and type of test cases (this algorithm assumed the nipple resided in the upper 20% of the breast's height, which may not always be the case). The ICP registration of the nipple region may introduce an error when our algorithm is used with other simulations. ICP registration may produce a rotation causing the source point cloud to spin around the longitudinal axis of the breast (a full 180° in the most extreme case) resulting in inaccurate correspondence. Given the intention of the step is to provide accurate correspondence of the nipple (an easily identifiable structure), a more robust algorithm that prohibits significant rotation may be needed. In addition, we should also note that without careful validation of the FE model for deformation, it may be that the boundary conditions represented by Figure 3 do not accurately describe the displacements associated with an inflating adjacent balloon.

5. CONCLUSIONS

The addition of rigid registration initialization of the chest-wall and nipple region of the breast to the Papademetris et al. symmetric closest point criteria significantly improves the accuracy of the approach for the breast's morphology. While the maximum error located in the center of the depression remains high for our algorithm at 2.68 cm (similar to Papademetris et al.'s maximum error of 2.78 cm), the RMS error is significantly improved to 6.0 mm (as compared to Papademetris et al.'s RMS error of 1.02 cm). Furthermore, it is clear that the algorithm demonstrates an increase in accuracy as the degree of compression is decreased. Finally, the use of other geometric information and additional experimentation with test cases may enhance this algorithm to provide more robust and accurate determination of correspondence.

ACKNOWLEDGEMENTS

This work was supported by the Vanderbilt Undergraduate Summer Research Program and the Whitaker Young Investigator Program as sponsored by the Whitaker Foundation. The authors would also like to thank John Boone, PhD of the University of California-Davis, Professor of Biomedical Engineering for providing the CT images of the breast volume that were used in this work.

REFERENCES

- [1] American Cancer Society, "American Cancer Society: Breast Cancer Facts & Figures 2001-2002," American Cancer Society, Inc. 2001
- [2] H. Frick and S. Morse, "The electrical capacity of tumors of the breast," *Journal of Cancer Research*, vol. 10, pp. 340-76, 1926
- [3] B. A. Brooksby, H. Dehghani, B. W. Pogue, and K. D. Paulsen, "Near-infrared (NIR) tomography breast image reconstruction with a priori structural information from MRI: algorithm development for reconstructing heterogeneities," *IEEE Journal of Selected Topics in Quantum Electronics*, vol. 9, pp 199-209, 2003
- [4] T. A. Krouskop, T. M. Wheeler, F. Kallel, B. S. Garra, and T. Hall, "Elastic moduli of breast and prostate tissues under compression," *Ultrasonic Imaging*, vol. 20, pp. 260-74., 1998.
- [5] E. C. Fear, "Microwave imaging of the breast," *Technology in Cancer Research and Treatment*, vol. 4, pp. 69-82, 2005
- [6] Y. Zho and Z. Gho, "A review of electrical impedance techniques for breast cancer detection," *Medical Engineering and Physics*, vol. 25, pp. 79-90, 2003
- [7] C. W. Washington and M. Miga, "Modality independent elastography (MIE): a new approach to elasticity imaging," *IEEE Transactions on Medical Imaging*, vol. 23, pp 1117-28, 2004

- [8] D. Rueckert, L. I. Sonoda, C. Hayes, D. L. G. Hill, M. O. Leach, and D. J. Hawkes, "Nonrigid registration using free-form deformations: application to breast MR images," *IEEE Transactions on Medical Imaging*, vol. 18, pp. 712-21, 1999
- [9] X. Papademetris, A. J. Sinusas, D. P. Dione, R. T. Constable, and J. S. Duncan, "Estimation of 3-D Left Ventricular Deformation from Medical Images using Biomechanical Models," *IEEE Transactions on Medical Imaging*, vol. 21, pp. 786-800, 2002
- [10] M. I. Miga, "A new approach to elastography using mutual information and finite elements," *Physics in Medicine and Biology*, vol. 48, pp. 467-80, 2003
- [11] J. M. Boone and K. K. Lindfors, "The effect of breast density on cancer detection performance in mammography," *Journal of Women's Imaging*, vol. 3, pp. 122-28, 2001
- [12] J. M. Boone, T. R. Nelson, K. K. Lindfors, and J. A. Seibert, "Dedicated breast CT: radiation dose and image quality evaluation," *Radiology*, vol. 221, pp. 657-67, 2001

An Elastography Framework for Use in Dermoscopy

Michael I. Miga^{1,2,a}, Jao J. Ou¹, Darrel L Ellis³

¹Vanderbilt University, Department of Biomedical Engineering, Nashville, TN 37235

²Vanderbilt University Medical Center, Department of Radiology and Radiological Sciences,
Nashville, TN 37232

³Vanderbilt University Medical Center, Department of Medicine, Division of Dermatology,
Nashville, TN 37232

^acorresponding author

(Michael.I.Miga, Jao.J.Ou, Darrel.L.Ellis)@vanderbilt.edu

ABSTRACT

Multiple skin conditions exist which involve clinically significant changes in elastic properties. Early detection of such changes may prove critical in formulating a proper treatment plan. However, most diagnoses still rely primarily on visual inspection followed by biopsy for histological analysis. As a result, there would be considerable clinical benefit if a noninvasive technology to study the skin were available. The primary hypothesis of this work is that skin elasticity may serve as an important method for assisting diagnosis and treatment. Perhaps the most apparent application would be for the differentiation of skin cancers, which are a growing health concern in the United States as total annual cases are now being reported in the millions by the American Cancer Society. In this paper, we use our novel modality independent elastography (MIE) method to perform dermoscopic skin elasticity evaluation. The framework involves applying a lateral stretching to the skin in which dermoscopic images are acquired before and after mechanical excitation. Once collected, an iterative elastographic reconstruction method is used to generate images of tissue elastic properties and is based on a two-dimensional (2-D) membrane model framework. Simulation studies are performed that show the effects of three-dimensional data, varying subdermal tissue thickness, and nonlinear large deformations on the framework. In addition, a preliminary in vivo reconstruction is demonstrated. The results are encouraging and indicate good localization with satisfactory degrees of elastic contrast resolution.

KEY WORDS: Elastography, Dermoscopy, Mechanical Properties, Finite Element, Image Similarity, Elasticity Imaging

1. INTRODUCTION

Because multiple conditions exist which involve clinically significant changes in skin elasticity, early detection of such changes could prove critical in formulating a proper treatment plan. However, most diagnoses still rely primarily on visual inspection followed by biopsy of suspect areas for histological analysis. Perhaps the most apparent application would be for the differentiation of skin cancers, which are a growing health concern in the United States as total annual cases are now being reported in the millions by the American Cancer Society¹. Of the three major types of skin cancer reported annually, basal cell carcinoma (BCC) makes up approximately 800,000+, squamous cell carcinoma (SCC) cases number approximately 200,000+, and a remaining 60,000+ melanoma cases. With respect to BCC, approximately 5-10% of these can be aggressive and infiltrate the surrounding tissue and sometimes into bone and cartilage. It rarely metastasizes but can cause scars and disfigurement. With respect to SCC, early detection is the key to successful treatment. If left unchecked, SCC can also cause

disfigurement and typically approximately 3-4% of cases results in metastasis which is usually fatal. Melanoma is the most fatal. Melanoma is malignant and if left unchecked, it will spread to other parts of the body, becomes difficult to treat, and can be fatal. If one were to include among the common cancer statistics, aggressive BCC's and metastatic SCC's, skin cancer would likely be the second most prevalent among newly diagnosed cancers.

While the above statistics are compelling, when speaking to lethality, skin cancer is less significant than its more fatal counterparts in breast, lung, colon/rectal, and prostate. However when considering the economic cost that skin cancer incurs on US healthcare, the pursuit of skin cancer characterization has considerable merit. The ability to differentiate benign from malignant, and aggressive from non-aggressive skin lesions would provide considerable savings to health care costs within the United States. Each year it is estimated that approximately 5-7 million patients undergo biopsies for skin cancer with only a fraction resulting in malignancies. While complete multi-center biopsy studies have not been performed, one study that took place documented the percentage of skin biopsy specimens that were malignant, i.e. they termed this the "malignancy ratio"². In this study, the malignancy was approximately 40% with a very wide variability among the 22 dermatologists (13.4-86.6%) that participated in the study. If one considers 5 million biopsies, this would translate to approximately 3 million unnecessary biopsies per year, and approximately \$300-600 million in saved expenditures per year^{3,4}. Furthermore, this does not even include cosmetic surgery costs in the case of scarring or complications associated with bleeding and infections. If an inexpensive imaging device could differentiate lesions with reasonably high specificity and sensitivity, it would have considerable significance.

It should also be noted that measuring cutaneous elasticity is also potentially important to medical areas outside of clinical dermatology. For instance, in a recent study of 100 women receiving hormone replacement therapy, Pierard *et al* demonstrated a positive correlation between bone mass density and skin elasticity^{5,6}. Another study conducted by Yoon *et al* showed a similar relevance for patients afflicted with diabetes mellitus⁷. Further uses for evaluating skin elasticity range from surgery (minimization of scarring, chronic graft versus host disease) to rheumatology (scleroderma, lupus) to obstetrics (striae development in pregnancy)⁸⁻¹².

With respect to diagnostic technological advances, developments have been concerned with obtaining a better view of the skin, either via improved optics (i.e. dermoscopy) or by more advanced and novel imaging systems ranging from high-frequency ultrasound to confocal laser microscopy^{13,14}. Other strategies involving electrical impedance mismatch¹⁵, Raman spectroscopy¹⁶, and cytological smears¹⁴ have also been forthcoming. In lieu of these methods that capitalize on electrical, optical, and biochemical phenomena, we have chosen to pursue an approach which is based on analyzing mechanical behavior of the skin. Detecting changes in tissue by palpation and then associating them with a disease state has a long-standing history in clinical medicine, and utilizing changes in the mechanical properties to specifically characterize the skin does have precedent. A thoughtful review by Edwards and Marks discusses the complex mechanical behavior of skin when subjected to in vitro and in vivo testing¹⁷. Their review highlights extensive methodologies being used to quantify skin properties (e.g. uni-axial and bi-axial extensometry, torsion stimulators, indentometry, ballistometric tests, shear wave application devices, dynamic suction methods, ultrasonics, and electrodynamicometry) and also emphasizes the difficulties in comparing across these methods. One of the authors' conclusions is that the need for quantitative reproducible methods to assess skin health is necessary given the considerable subjectivity in clinical analysis.

Following previous work in¹⁸, we are developing a new method we have termed 'modality-independent elastography' (MIE) that combines image processing with an inverse problem. More specifically, image similarity metrics routinely used with image registration methods are recast to satisfy an inverse elasticity problem framework whereby mechanical properties within a biomechanical model of deforming tissue become the driving parameters for improved image similarity. In this way, MIE circumvents two potential limitations of current elastographic techniques. First, it is not inherently

dependent on pre-processing steps such as homologous feature selection and tracking which drive active contour models¹⁹⁻²¹ and other traditional displacement-based iterative methods²²⁻²⁴, although such techniques can aid in the determination of boundary conditions. Secondly, because it is an image processing methodology, MIE is not reliant on a particular imaging modality (such as in ultrasound and magnetic resonance elastography) as long as the acquired images provide sufficient pattern to allow for comparison. Building upon recently with a multi-resolution implementation²⁵, this paper presents analysis using a tissue model that incorporates geometric nonlinearities, the effects of the three-dimensional nature of the problem which include varying subcutaneous layer thicknesses, and varying lesion depth. In addition, a relatively crude preliminary *in vivo* result is also demonstrated.

2. MATERIALS AND METHODS

2.1. Modality Independent Elastography

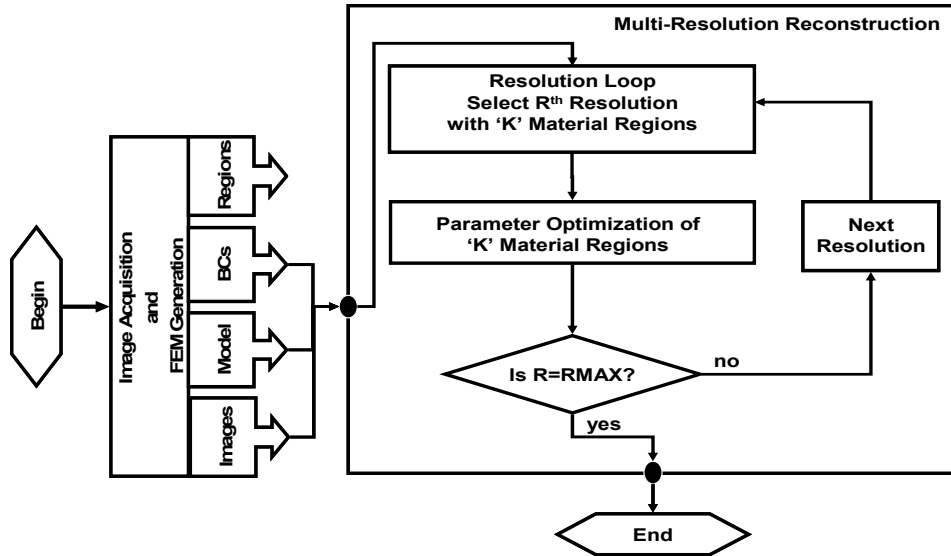


Fig 1. MIE framework.

MIE begins with the acquisition of an image series consisting of an image acquired prior to and after an applied deformation. The method is “independent” because it does not require any specific imaging modality but rather that sufficient pattern is present within the acquired images such that material properties can be assessed from pattern changes within the acquisition-pair. This is a similar requirement for many methods of non-rigid image registration. At its core MIE is an image analysis method whereby a model-generated deformation field is applied to the pre-deformed image series (*source*) and compared to its acquired deformed counterpart (*target*). This comparison is nested within a Levenberg-Marquardt optimization routine such that the material properties become the parameters of interest in matching the model-deformed *source* image to the acquired *target* image. The methods and development of this technique have been reported in detail elsewhere^{18, 25-29}.

With respect to the optimization framework for MIE, it can be represented as a least squared error objective function:

$$\phi(\vec{E}) = \min \left\{ \left\| \mathbf{S}(\vec{E}_t) - \mathbf{S}(\vec{E}_e) \right\|^2 \right\} \quad (1)$$

where $\mathbf{S}(\vec{E}_t)$ is the similarity value achieved when comparing the target image to itself (i.e. the maximum value for the similarity measure, so for the correlation coefficient $\mathbf{S}(\vec{E}_t) = 1$) and $\mathbf{S}(\vec{E}_e)$ is the similarity between the model-deformed source image and the acquired target image using the current estimate of the

elastic modulus. Eq. (1) is optimized by setting the partial derivative equal to zero and solved using a Levenberg-Marquardt approach:

$$[\mathbf{J}^T][\mathbf{J}] + \alpha[\mathbf{I}]\{\Delta\bar{\mathbf{E}}\} = [\mathbf{J}^T]\{\mathbf{S}(\bar{\mathbf{E}}_t) - \mathbf{S}(\bar{\mathbf{E}}_E)\} \quad (2)$$

where $[\mathbf{J}]$ is the $M \times N$ Jacobian matrix of the form $\mathbf{J} = \frac{\partial \mathbf{S}(\bar{\mathbf{E}}_E)}{\partial \bar{\mathbf{E}}}$ and M is the number of similarity measurements (i.e. zones) being made and N is the number of material property regions. Because $[\mathbf{J}^T][\mathbf{J}]$ (an approximation to the Hessian matrix) tends to be ill-conditioned, it is regularized with an empirically determined α parameter found in the standard Levenberg-Marquardt approach³⁰. The determination of this regularization parameter is described in³¹. The multi-resolution framework to MIE is shown in Fig. 1. The methodology used involves a hierarchical material parameter resolution series. This has been reported elsewhere^{25, 27} and has been shown to assist in avoiding local minima that are associated with the decorrelation of patterned data.

2.2. Model for Skin

One critical component within all model-based inverse problem frameworks is the selection of the computer model to represent the continuum of interest. In previous phantom, simulation, and in vivo studies, we have elected to employ a plane stress linear elastic model to simulate the skin. This model is a two dimensional approximation of the three dimensional system which assumes a symmetric, isotropic, thin specimen in equilibrium, and stresses that are constrained to lie within the plane. These assumptions simplify Cauchy's law from 36 stiffness constants to 2 and use the equation:

$$\nabla \cdot \boldsymbol{\sigma} = \mathbf{0} \quad (3)$$

where $\boldsymbol{\sigma}$ is the 2D Cartesian stress tensor and is defined below followed by the plane stress constitutive equations:

$$\begin{bmatrix} \sigma_x \\ \sigma_y \\ \tau \end{bmatrix} = \frac{E}{(1-\nu)^2} \begin{bmatrix} 1 & \nu & 0 \\ \nu & 1 & 0 \\ 0 & 0 & \frac{1-\nu}{2} \end{bmatrix} \begin{bmatrix} \partial u / \partial x \\ \partial v / \partial y \\ \partial v / \partial x + \partial u / \partial y \end{bmatrix} \quad (4)$$

where E is Young's modulus, and ν is Poisson's ratio. For this work, we have determined that a Poisson's ratio of 0.485 for our skin phantoms and tissue work has performed reasonably well. This value would correlate with a $\sim 32:1$ ratio of the Lamé' constants ($\lambda : \mu$, with μ the shear modulus, and λ being the second Lamé' constant) which is reasonably below the convention for Poisson locking (sometimes called mesh locking and typically has $\lambda \gg \mu$) although one could argue that hyperelastic models may be the more appropriate model and will need to be explored in the future. Using the Galerkin weighted residual method to integrate and solve this set of partial differential equations, a finite element framework is generated and can be solved to represent a displacement field for a given distribution of Young's modulus.

In this paper, the plane stress model has been enhanced to incorporate the full Green-Lagrange strain tensor as defined by:

$$\varepsilon_{i,j} = \frac{1}{2} \left(\frac{\partial \mathbf{u}_i}{\partial \mathbf{x}_j} + \frac{\partial \mathbf{u}_j}{\partial \mathbf{x}_i} + \frac{\partial \mathbf{u}_k}{\partial \mathbf{x}_i} \frac{\partial \mathbf{u}_k}{\partial \mathbf{x}_j} \right). \quad (6)$$

Use of this tensor description abandons the traditional small-strain approximation in favor of one compatible with large deformations. The difference in solutions between small and large deformation theory can be seen in the 2D simulations shown in Fig. 2. Fig. 2 compares the boundary shape of a

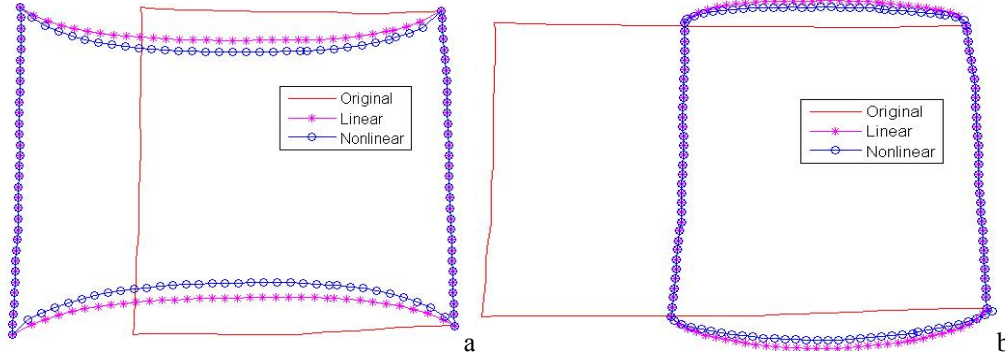


Fig. 2. (a) Fixed ~30-40% tensile strain applied to original with linear and nonlinear model, (b) ~30-40% compressive strain.

Hookean linear elastic membrane to a 2D Hookean geometrically nonlinear elastic model. For these simulations, a plane stress approximation was performed *for comparison only* of the solution due to nonlinear terms (i.e. a ~30-40% compressive stress could never be applied to a thin specimen, the material would buckle well before). The important aspect to notice is that more necking and less bulging occur in the nonlinear than the linear model in tension, and compression, respectively. With respect to the difference in the linear model among Fig. 2a and 2b, 2b is the reverse of 2a (this is a characteristic of linear theory). However, the lack of this symmetry for the nonlinear model is characteristic of the Green-Lagrange strain tensor and is caused by the interplay between the linear and quadratic terms in the tensor. In this paper, the results from the linear and nonlinear model will be compared.

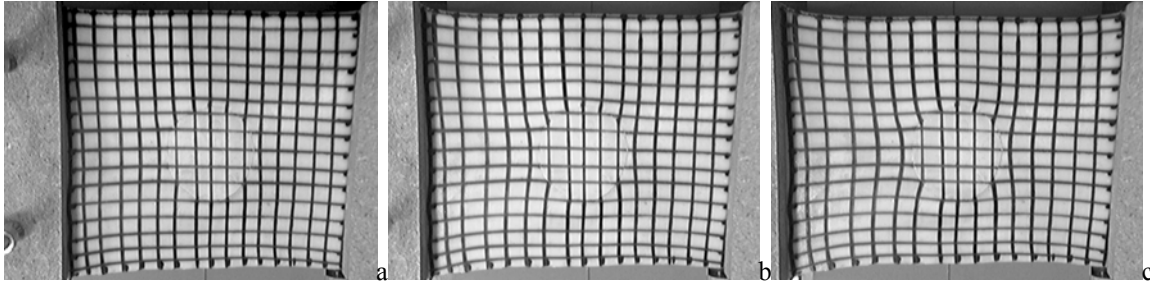


Fig 3. Phantom membrane stretches (a) baseline, (b) 1 cm stretch, (c) 2 cm stretch.

2.3. Nonlinear Model Experiments

In previous work, a phantom of simulated skin was generated from using a polyurethane membrane 25 cm long, 15 cm wide, and approximately 2 mm thick containing two types of materials. The bulk material, representing “normal” skin, was chosen to be Evergreen 10 (Smooth-On, Easton, PA), while the stiffer Evergreen 50 was used to create a 5 cm circular inclusion of full depth and was placed at the center of the phantom. The visible surface of the phantom was modified by drawing a regular grid of horizontal and vertical lines spaced about 1 cm apart in either direction. Fig. 3 shows the skin phantom as acquired by an optical camera at the baseline, 1 cm, and 2cm stretch levels. Separate mechanical tests on the membrane were conducted using the EnduraTEC ELF 3200 material tester (EnduraTEC Systems Group, Bose Corporation, Minnetonka, MN)²⁵. Table 1 reports the expected Young’s Modulus contrast ratio based on a Hookean solid fitted to each respective stretch/strain level. The scale of lesion to field-of-view size is the anticipated aspect ratio for a dermoscopic system. This

Stretch	CR (Linear)	CR (Nonlinear)
1 (0.5 cm)	5.7	5.0
2 (1.0 cm)	5.0	4.8
3 (1.5 cm)	4.6	4.7
4 (2.0 cm)	4.2	4.4

Table 1. Expected elastic contrast ratio.

image data was used as an input to the MIE framework, and reconstructions comparing the linear and nonlinear model were generated.

2.4. Three-Dimensional Model Experiments

In an effort to test the MIE algorithm with more realistic images of the skin as would be expected in the clinic, a simulation study was performed on an image obtained from the Dermatology Image Atlas project (www.dermatlas.org, “melanoma_1_040510”, contributed by Eric Ehram, M.D., Fig. 4a). Dermoscopic images provide the challenge of relying on the natural pattern instead of the structured grid used in the membrane phantom experiments (although the skin could be printed upon with an ink grid). Previous simulation work on this image can be found in ²⁵.

One possible critique of this dermoscopic framework is the fear that underlying layers would confound the approach. As a result, we have modified the simulation study reported in ²⁵ (e.g. Fig. 4b) to be more realistic. Fig. 5a-5c shows the setup of the new simulation study. In this study, six $10\text{ cm} \times 10\text{ cm}$ domains were constructed which had different layered structures. Three domains were 6mm in total thickness ($\sim 4\text{mm}$ epidermis/dermis, 2mm subcutaneous) and had 1cm central inclusions varying in depth 1mm , 2mm , and 3mm , respectively. The remaining three domains were the same except that the subcutaneous layer thickness was increased to 7mm . The selection of subcutaneous layer thickness ^{32, 33} and stiffness values ³⁴ were based on the literature. Using this domain, a mechanical aperture that stretched the skin was simulated, 3D displacements were calculated (Fig. 5b), and then projected on to the

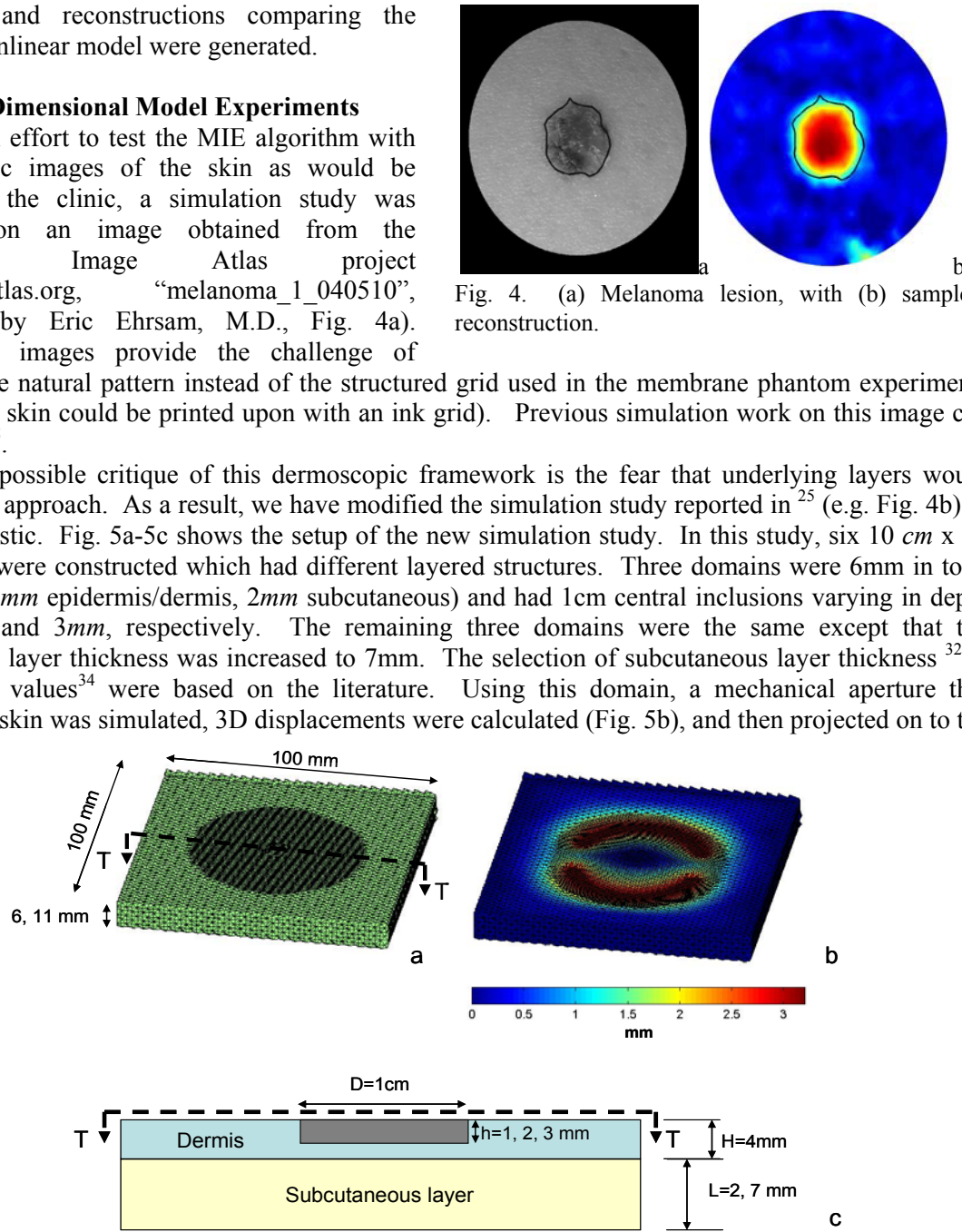


Fig. 5. (a) Mesh with refinement in lesion area, (b) simulated compression of skin by device, and (c) depth variation (transect T is shown in (a)).

original 2D mesh. A new set of simulated images (deforming Fig. 4) was generated and then used as input to the 2D MIE algorithm.

2.5 Noninvasive In Vivo Experiments

In addition to the simulation experiments, a second camera and deformation system was constructed using a Sony XCD-X710CR CCD camera with a Schneider 12 mm lens and a circular

polarizing filter for the optics mounted over a crude spring-loaded standard set of pincers that were pressed against the skin surface and bound with commercial adhesive. Digital images (800 x 600 resolution) of a common nevus of palpable stiffness that was 2-3 mm in diameter and located on the volar aspect of the left forearm of a male volunteer were acquired in both relaxed and stretched states. It was determined that the reflection and scattering of ambient fluorescent lighting interfered with this particular setup and affected the input image quality, so an artificial grid was imposed to counteract specularly.

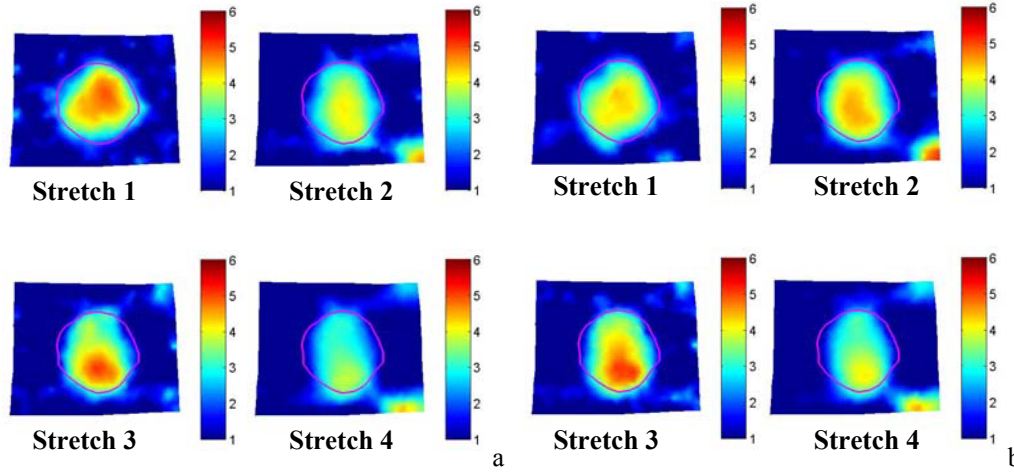


Fig 6. (a) Linear Hookean reconstructions for each stretch state, and (b) the geometrically nonlinear Hookean reconstructions. Contour shows inclusion border.

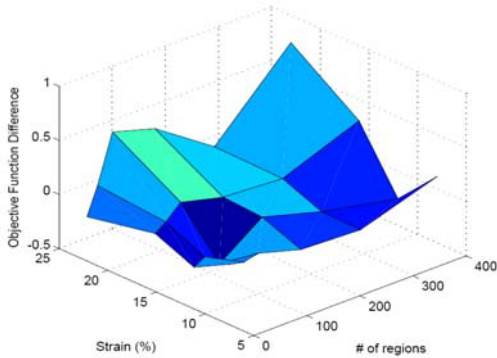


Fig 7. Objective function difference between linear and nonlinear models over all stretches and resolutions.

approximate contrast ratio of the lesion-to-bulk material for each of the cases shown in Fig. 8. Fig 9. illustrates the results from the *in vivo* experiment conducted. Fig. 9 shows (a) the nevus, (b) the finite element grid, and (c,d) reconstructed elasticity images. Fig. 9c-d illustrate the effect of incorporating increasing degrees of *a priori* knowledge of the actual location and elasticity distribution into the algorithm. Fig. 9c is a general elasticity reconstruction of the nevus with lesion-related initial guess, and Fig. 9d maintains the spatial *prior* of Fig. 9c for the entire duration of the reconstruction process.

4. DISCUSSION

With respect to Fig. 6, the most important features to note are a very subtle improvement in satisfying the inclusion contour, and the decrease in variability of the contrast in the geometric nonlinear reconstructions. This is consistent with the behavior in Table 1 and indicates that the geometric nonlinear reconstruction is performing as predicted. One thing to note is that if the membrane were a true Hookean

Images were acquired in the baseline and stretched state and given to the MIE algorithm.

3. RESULTS

Fig. 6 illustrates the reconstructions of the phantom membrane system using the linear and nonlinear models, respectively. Fig. 7 reports how the objective function varies between the linear and nonlinear model reconstructions of Fig. 6. Fig. 8 demonstrates the dependence of resolving stiffness (3:1, 6:1, 12:1) on depth (1, 2, 3 mm) for the 18 combinations (combinations of 3 depths, 3 contrast ratios, and 2 subcutaneous layer thicknesses). Table 2 reports an

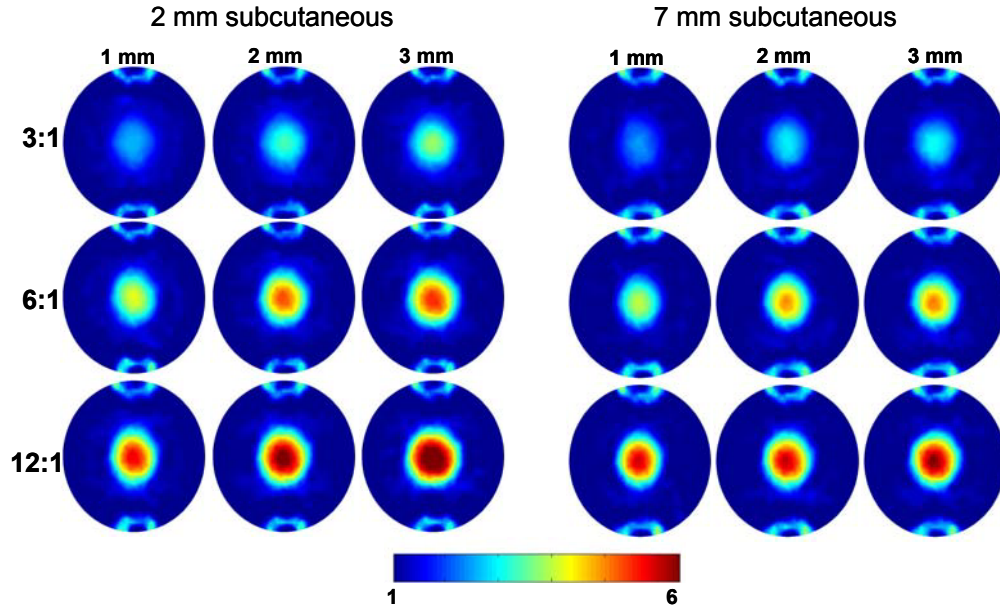


Fig. 8. 3-D effects on elasticity images with varying lesion depth and subcutaneous layer depth. Ratio on left shows actual contrast while colorbar shows reconstructed. Fig. 4 shows the lesion contour.

2mm SQ	1 mm	2 mm	3 mm
3:1	2.12	2.55	2.79
6:1	3.08	3.76	4.00
12:1	4.11	4.71	5.15

7mm SQ	1 mm	2 mm	3 mm
3:1	1.93	2.27	2.34
6:1	2.87	3.49	3.55
12:1	4.03	4.28	4.53

Table 2. Lesion-to-bulk contrast ratio at each lesion depth (1mm, 2mm, 3mm) and target contrast level (3:1, 6:1, 12:1) for 2mm (top) and 7mm (bottom) subcutaneous thicknesses.

nonlinear solid, the CR would be the same across all stretches, i.e. strain levels. While the variability across levels was reduced between the linear and nonlinear models for strain, the data supports a more complex constitutive model for this phantom system. Fig. 7 also demonstrates some consistency with the extension to a nonlinear model. Here we see that at the largest stretch values, the difference between the two models is highest with the nonlinear model outperforming the linear.

With respect to Fig. 8, and Table 2, despite not reaching the expected contrast ratio values, each result localized the lesion and demonstrated sensitivity to depth and contrast. With respect to contrast ratio, this

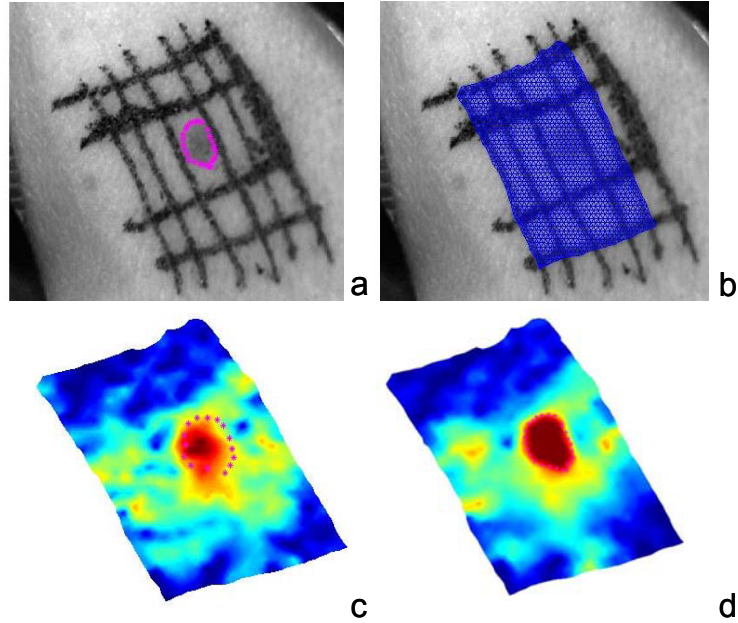


Fig. 9. (a) Dermoscopic scale interrogation (magenta border is about 3 mm in diameter), (b) reconstruction mesh, (c) general elasticity reconstruction, (d) incorporation of lesion border as *a priori* information.

simulation was more challenging than previous work. The results indicate that varying subcutaneous thicknesses has a very modest effect in confounding lesion reconstructions for the contrast regime shown. Fig. 8 does suggest that at some contrast levels there may be overlap (e.g. a 3mm, 3:1 lesion with 2mm subcutaneous layer may be confused with a 1mm, 6:1 lesion with 7mm subcutaneous layer). This could be potentially confounding if left in the absence of other information. However, Horejsi et al. and Moller et al.^{32, 33} do provide guidance for estimating the subcutaneous tissue thickness in a general population. Additionally, they use a relatively inexpensive optical device to make these measurements. There is little doubt that using this *a priori* information would reduce variability in interpretation. It is interesting to speculate that if a particular lesion type was of a known stiffness *a priori* then perhaps the reconstruction contrast could be used to estimate lesion depth. Looking across the grids of a particular property contrast, there is a definitive change in the reconstruction as a function of depth.

Fig. 9 demonstrates a preliminary attempt of applying the framework to an *in vivo* system. Considering there was very little control over this system and no ground truth was available, these results qualitatively confirm the potential utility of MIE in evaluating an area of skin with a region of differing elasticity. While the results in Fig. 9 c,d are not completely satisfying at this time, it should be emphasized that the camera-system employed a coarse resolution, and the skin-to-device coupling system was extremely crude. Given this somewhat ad-hoc experiment, the detection of any anomaly in the correct region is encouraging for this approach. It was also interesting to note the increase in performance by adding the lesion extents to the information provided to the algorithm.

5. CONCLUSIONS

The results from the experiments above demonstrate an ability to use the MIE framework within the dermoscopy setting. Methodological concerns regarding the use of geometric nonlinear models, three-dimensional effects, and *in vivo* conditions are addressed. The results indicate that while geometric nonlinearities do modestly affect reconstructions, nonlinear material models may be needed to correct for remaining discrepancies. A modest improvement was shown using the geometric nonlinear model especially at large strain values which is consistent with the theoretical development. The three-dimensional effects of lesion depth and varying subcutaneous layer thicknesses are assessed. Lesion depth does affect contrast ratio whereas subcutaneous layers affect the reconstructions to a significantly lesser degree. Avenues to detect lesion depth in the presence of *a priori* knowledge of a lesion's stiffness may have surgical implications. Preliminary *in vivo* work suggests that lesion characterization is possible although specificity and sensitivity of the method await further study and will need a considerably more robust acquisition system.

6. ACKNOWLEDGEMENTS

This work was supported by the Whitaker Foundation's Young Investigator Program and the Whitaker Foundation's Continuation Program. This work was also supported by the Congressionally Directed Medical Research Program—Breast Cancer Research Program.

7. REFERENCES

1. American Cancer Society, "Cancer Facts and Figures 2006," A. C. Society, ed. (Atlanta, GA, 2006).
2. A. R. Green, G. W. Elgart, F. Ma, D. G. Federman, and R. S. Kirsner, "Documenting dermatology practice: Ratio of cutaneous tumors biopsied that are malignant," *Dermatol. Surg.* **30**, 1208-1209 (2004).

3. G. J. Chen, C. B. Yelverton, S. S. Polisetty, T. S. Housman, P. M. Williford, H. V. Teuschler, and S. R. Feldman, "Treatment patterns and cost of nonmelanoma skin cancer management," *Dermatol. Surg.* **32**, 1266-1271 (2006).
4. K. A. Freedberg, A. C. Geller, D. R. Miller, R. A. Lew, and H. K. Koh, "Screening for malignant melanoma: A cost-effectiveness analysis," *Journal of the American Academy of Dermatology* **41**, 738-745 (1999).
5. G. E. Pierard, C. Pierard-Franchimont, S. Vanderplaetsen, N. Franchimont, U. Gaspard, and M. Malaise, "Relationship between bone mass density and tensile strength of the skin in women," *Eur. J. Clin. Invest.* **31**, 731-735 (2001).
6. G. E. Pierard, S. Vanderplaetsen, and C. Pierard-Franchimont, "Comparative effect of hormone replacement therapy on bone mass density and skin tensile properties," *Maturitas* **40**, 221-227 (2001).
7. H. S. Yoon, S. H. Baik, and C. H. Oh, "Quantitative measurement of desquamation and skin elasticity in diabetic patients," *Skin Res. Technol.* **8**, 250-254 (2002).
8. C. Braham, D. Betea, C. Pierard-Franchimont, A. Beckers, and G. E. Pierard, "Skin tensile properties in patients treated for acromegaly," *Dermatology* **204**, 325-329 (2002).
9. D. Carrino, J. Sorrell, and A. Caplan, "Age-related changes in the proteoglycans of human skin," *Archives of Biochemistry and Biophysics* **373**, 91-101 (2000).
10. J. A. Clark, J. C. Y. Cheng, and K. S. Leung, "Mechanical properties of normal skin and hypertrophic scars," *Burns* **22**, 443-446 (1996).
11. H. Dobrev, "In vivo study of skin mechanical properties in psoriasis vulgaris," *Acta Derm.-Venereol.* **80**, 263-266 (2000).
12. H. Sumino, S. Ichikawa, M. Abe, Y. Endo, O. Ishikawa, and M. Kurabayashi, "Effects of aging, menopause, and hormone replacement therapy on forearm skin elasticity in women," *J. Am. Geriatr. Soc.* **52**, 945-949 (2004).
13. A. A. Marghoob, L. D. Swindle, C. Z. M. Moricz, F. A. S. Negron, B. Slue, A. C. Halpern, and A. W. Kopf, "Instruments and new technologies for the in vivo diagnosis of melanoma," *Journal of the American Academy of Dermatology* **49**, 777-797 (2003).
14. E. Ruocco, G. Argenziano, G. Pellacani, and S. Seidenari, "Noninvasive imaging of skin tumors," *Dermatol. Surg.* **30**, 301-310 (2004).
15. R. Dua, D. G. Beetner, W. V. Stoecker, and D. C. Wunsch, "Detection of basal cell carcinoma using electrical impedance and neural networks," *IEEE Trans. Biomed. Eng.* **51**, 66-71 (2004).
16. M. Gniadecka, P. A. Philipsen, S. Sigurdsson, S. Wessel, O. F. Nielsen, D. H. Christensen, J. Hercogova, K. Rossen, H. K. Thomsen, R. Gniadecki, L. K. Hansen, and H. C. Wulf, "Melanoma diagnosis by Raman spectroscopy and neural networks: Structure alterations in proteins and lipids in intact cancer tissue," *J. Invest. Dermatol.* **122**, 443-449 (2004).
17. C. Edwards, and R. Marks, "Evaluation of biomechanical properties of human skin," *Clin. Dermatol.* **13**, 375-380 (1995).
18. M. I. Miga, "A new approach to elastography using mutual information and finite elements," *Phys. Med. Biol.* **48**, 467-480 (2003).
19. L. V. Tsap, D. B. Goldgof, and S. Sarkar, "Nonrigid motion analysis based on dynamic refinement of finite element models," *IEEE Trans. Pattern Anal. Mach. Intell.* **22**, 526-543 (2000).
20. L. V. Tsap, D. B. Goldgof, and S. Sarkar, "Fusion of physically-based registration and deformation modeling for nonrigid motion analysis," *IEEE Trans. Image Process.* **10**, 1659-1669 (2001).
21. L. V. Tsap, D. B. Goldgof, S. Sarkar, and P. S. Powers, "A vision-based technique for objective assessment of burn scars," *IEEE Trans. Med. Imaging* **17**, 620-633 (1998).
22. T. L. Chenevert, A. R. Skovoroda, M. O'Donnell, and S. Y. Emelianov, "Elasticity reconstructive imaging by means of stimulated echo MRI," *Magn. Reson. Med.* **39**, 482-490 (1998).
23. J. Ophir, S. K. Alam, B. Garra, F. Kallel, E. Konofagou, T. Krouskop, and T. Varghese, "Elastography: ultrasonic estimation and imaging of the elastic properties of tissues," *Proc. Inst. Mech. Eng. Part H-J. Eng. Med.* **213**, 203-233 (1999).

24. E. E. W. Van Houten, M. I. Miga, J. B. Weaver, F. E. Kennedy, and K. D. Paulsen, "Three-dimensional subzone-based reconstruction algorithm for MR elastography," *Magn.Reson.Med.* **45**, 827-837 (2001).
25. M. I. Miga, M. P. Rothney, and J. J. Ou, "Modality independent elastography (MIE): Potential applications in dermoscopy," *Medical Physics* **32**, 1308-1320 (2005).
26. M. I. Miga, "A new approach to elastographic imaging: Modality independent elastography," *Medical Imaging 2002: Image Processing: Proc. of the SPIE* **4684**, 604-611 (2002).
27. J. J. Ou, S. L. Barnes, and M. I. Miga, "Application of multi-resolution modality independent elastography for detection of multiple anomalous objects," in *Medical Imaging 2006: Physiology, Function, and Structure from Medical Images: Proc. of the SPIE*, (SPIE, San Diego, CA, 2006).
28. J. J. Ou, S. L. Barnes, and M. I. Miga, "Preliminary testing of sensitivity to input data quality in an elastographic reconstruction method," in *International Symposium on Biomedical Imaging 2006*, (Washington, D.C., 2006).
29. C. W. Washington, and M. I. Miga, "Modality independent elastograph ({MIE}): {A} new approach to elasticity imaging," *IEEE Trans. Med. Imaging* (**in press**), (2004).
30. D. W. Marquardt, "An algorithm for least-squares estimation of nonlinear parameters," *SIAM Journal of Applied Mathematics* **11**, 431-441 (1963).
31. N. Joachimowicz, C. Pichot, and J. P. Hugonin, "Inverse scattering: an iterative numerical method for electromagnetic imaging," *IEEE Trans. Biomed. Eng.* **39**, 1742-1752 (1991).
32. R. Horejsi, R. Moller, T. R. Pieber, S. Wallner, K. Sudi, G. Reibnegger, and E. Tafeit, "Differences of subcutaneous adipose tissue topography between type-2 diabetic men and healthy controls," *Exp. Biol. Med.* **227**, 794-798 (2002).
33. R. Moller, E. Tafeit, K. H. Smolle, T. R. Pieber, O. Ipsiroglu, D. M., C. Huemer, K. Sudi, and G. Reibnegger, "Estimating percentage total body fat and determining subcutaneous adipose tissue distribution with a new non-invasive optical device LIPOMETER," *Americal Journal of Human Biology* **12**, 221-230 (2000).
34. F. M. Hendriks, D. Brokken, J. T. W. M. van Eemeren, C. W. J. Oomens, F. P. T. Baaijens, and J. B. A. M. Horsten, "A numerical-experimental method to characterize the non-linear mechanical behavior of human skin," *Skin Res. Technol.* **9**, 274-283 (2003).

An Evaluation of 3D Modality Independent Elastography Robustness to Boundary Condition Noise

Jao J. Ou*, Rowena E. Ong, Michael I. Miga*

{jao.ou,rowena.ong,michael.i.miga}@vanderbilt.edu

Vanderbilt University, Department of Biomedical Engineering, Nashville, TN 37235

ABSTRACT

This work explores an inverse problem technique of extracting soft tissue elasticity information via nonrigid model-based image registration. The algorithm uses the elastic properties of the tissue in a biomechanical model to achieve maximal similarity between image data acquired under different states of loading. A framework capable of handling fully three-dimensional models and image data has been recently developed utilizing parallel computing and iterative sparse matrix solvers. For this preliminary investigation, a series of simulation experiments with clinical image data of human breast are used to test the robustness of the algorithm to expected mis-estimation of displacement boundary conditions encountered in real-world situations. Three methods of automated point correspondence are also examined as means of generating boundary conditions for the algorithm.

Keywords: elastography, computational modeling, inverse problem, non-rigid registration

1. INTRODUCTION

The characterization of the mechanical properties of tissue is an important potential source of information for detection and diagnosis of disease processes. For example, there is a long-standing clinical appreciation of evaluating tissue elasticity through palpation in the physical examination and correlating differences in stiffness with possible pathological states. A minimally invasive methodology for analyzing tissue deformation through imaging and/or image processing techniques is a central goal of the field of elastography [1,11]. Application of such methods to the interrogation of the breast [2,3], skin [4-6], prostate [7], and other accessible organ systems is an active area of research.

Many of the current elastography methods are founded in ultrasound (US) and magnetic resonance (MR) imaging and involve the estimation of induced displacements within the tissue of interest to infer the elasticity distribution. We have recast the problem as a physically-constrained non-rigid image registration utilizing quasi-static deformation and image similarity metrics that reconstruct the spatial distribution of elasticity parameters. This technique has been termed 'modality-independent elastography' (MIE) [8-10] because of its ability to handle native anatomical images from different sources with relatively simple modifications to the acquisition procedure. To date, data from MR, X-ray computed tomography (CT), and digital photography have been used to drive the algorithm. In addition to the necessary preparation and effort involved in gathering images, the other major input to this reconstruction method is the delineation of boundary conditions on the region of interest. Because this process currently involves varying levels of manual interaction, there is a need to develop a protocol that is both effective and mostly automated for determining point correspondences. The objectives of this work are to test the effects of degradation in input data quality on the end reconstruction and examine candidate methods for generation of displacement boundary conditions. This is done in the context of evaluating the robustness of a newly realized three-dimensional version of MIE by performing simulation experiments with randomized noise processes and comparing the fidelity of reconstructions resulting from boundary conditions generated by three different techniques of determining surface point correspondence.

2. METHODS

2.1 Elastographic reconstruction framework

The conceptual framework for our elastographic reconstruction has been previously described in [6,8-10]. In brief, an image of a tissue of interest (*source*) is deformed by a biomechanical computer model and compared against an acquired image of the same tissue in a mechanically loaded state (*target*). Iterative updates of elasticity parameters to the model

are performed until a suitable match in intramodal image similarity is achieved in a least squares manner to satisfy a non-linear optimization scheme. This process can be classified as an inverse problem, with model-based deformation of the source image representing the forward problem. The three major components of the algorithm are the model, image comparison, and optimization, each of which is described in more detail below.

The partial differential equation that expresses a state of mechanical equilibrium can be written as [12]:

$$\nabla \cdot \sigma = 0 \quad (1)$$

where σ is the Cartesian stress tensor. We have elected to model the constitutive tissue behavior using Hooke's Law of linear elasticity, which states that the strain is proportional to the applied stress, and assume that materials are isotropic and incompressible in nature. This leads to the formulation of Cauchy's Law as

$$\begin{pmatrix} \epsilon_{xx} \\ \epsilon_{yy} \\ \epsilon_{zz} \\ \epsilon_{xy} \\ \epsilon_{yz} \\ \epsilon_{xz} \end{pmatrix} = \begin{pmatrix} \frac{\sigma_{xx}}{E} - \frac{\nu}{E}(\sigma_{yy} + \sigma_{zz}) \\ \frac{\sigma_{yy}}{E} - \frac{\nu}{E}(\sigma_{xx} + \sigma_{zz}) \\ \frac{\sigma_{zz}}{E} - \frac{\nu}{E}(\sigma_{xx} + \sigma_{yy}) \\ \frac{\sigma_{xy}}{2G} \\ \frac{\sigma_{yz}}{2G} \\ \frac{\sigma_{xz}}{2G} \end{pmatrix} \quad (2)$$

which describes the constitutive relationship between stress and strain in terms of the elasticity parameters E (Young's modulus) and ν (Poisson's ratio). The shear modulus G is defined as $\frac{E}{2(1+\nu)}$.

A finite element (FE) representation of the model is constructed from the source image and assigned appropriate boundary conditions based on estimated displacement or stress. The standard Galerkin method of weighted residuals [13] is used to construct and solve the system, which yields a set of displacements that are used to deform the source image. This model-deformed image is then compared to the target using an intensity-based image similarity calculated for a series of voxel groupings determined by a downsampling of the image set overlap. The correlation coefficient (CC) [14] is the method of choice, as it has empirically demonstrated superior performance over other metrics such as the sum of squared differences and normalized mutual information.

The elasticity parameter optimization can be written as the minimization of the least squares error objective function

$$\Psi = |S_{TRUE} - S_{EST}|^2 \quad (3)$$

where S_{TRUE} is the set of similarity values achieved when comparing the target image to itself, S_{EST} is the similarity between the model-deformed source and the target images using current estimates of the elastic modulus distribution, and $|\cdot|$ denotes the vector L_2 norm. Note that by definition, S_{TRUE} for CC has a constant value of 1. Using a Levenberg-Marquardt approach, the residual form of equation (3) becomes

$$[J^T J + \alpha I] \{\Delta E\} = [J^T] \{S_{TRUE} - S_{EST}\} \quad (4)$$

where $\mathbf{J} = \partial \mathbf{S}_{\text{EST}} / \partial \mathbf{E}$ is the Jacobian matrix and the regularization parameter α is determined using the methods described in [15]. Modulus values are updated by $\Delta \mathbf{E}$ until an error tolerance is reached or a maximum number of iterations have been completed. Spatial averaging of elasticity values in the model and solution relaxation between iterations are also utilized to improve the stability of the optimization.

It should be noted that the size of the Jacobian matrix is dependent on the number of material properties to be reconstructed, with each column requiring a forward solve of the FE model. For the general lesion detection problem, a fine discretization of the mesh requires many solutions such that the building of this matrix consumes a considerable portion of computational resources. This fact is exacerbated with the use of three-dimensional data and necessitates a parallelized system. Recent work using the Portable Extensible Toolkit for Scientific Computation (PETSc) toolkit [16,17] has provided the necessary coding base for interfacing sparse matrix system solvers with a C/C++ optimization framework in order to supersede the original MATLAB/FORTRAN framework. This new version is designed to scale readily between the complexity of the model and the number of processors available; it has been tested on a homogeneous cluster of ten processors, with further active development taking place in conjunction with the Vanderbilt ACCRE project, which houses hundreds of CPUs.

2.2 Simulation experiment setup

A CT volume of a human breast, obtained from UC-Davis Dept. of Radiology, was used as the source image (256 x 256 x 130, 0.6mm x 0.6mm x 0.6mm voxel spacing) for the remainder of this work. The surface of the breast was segmented (ANALYZE 6.0, Mayo Clinic, Rochester, MN) to create a three-dimensional mesh composed of 39,013 nodes connected as 214,163 tetrahedral elements. In order to ensure initial data fidelity for reconstruction experiments, an idealized target image volume and gold standard boundary condition set were created. A 2-cm spherical tumor was implanted in the center of the mesh by assigning a stiff modulus value to the member elements that was six times higher than the surrounding material [18]. Tissue deformation from the inflation of a rectangular air bladder against the lateral surface of the breast was numerically simulated to qualitatively match observed mechanical loading of an existing device on a breast-mimicking phantom of polyvinyl alcohol cryogel. The stress distribution over a rectangular contact area was modeled as the cross-section of a Gaussian pressure field with its maximum value located at the center of the bladder; the base of the breast was fixed in place as if pinned to the chest wall. The deformation field throughout the domain was calculated using a direct forward solve of the finite element model and then applied to the intensity field of the source image to create a target volume. Displacements at the surface nodes were used to make a final description comprised of all Type I (Dirichlet) boundary conditions. Figure 1 below illustrates the setup of the data used.

All reconstructions were performed using *a priori* knowledge of the location and size of the inclusion in order to limit the scope of the problem (e.g. the expense of the Jacobian matrix) to a two-material discrimination of relative stiffness (elastic contrast). Having a defined physical model and synthetic image comparison also allows for examination of the optimization behavior separately from the other MIE components in order to best evaluate the effect of input inaccuracies on the final elasticity distribution. The reconstruction algorithm begins by assigning a homogeneous elasticity distribution, with Poisson's ratio held constant at $\nu = 0.485$ to represent a nearly incompressible material. For this data set, 733 similarity zones were discretized from the target image volume.

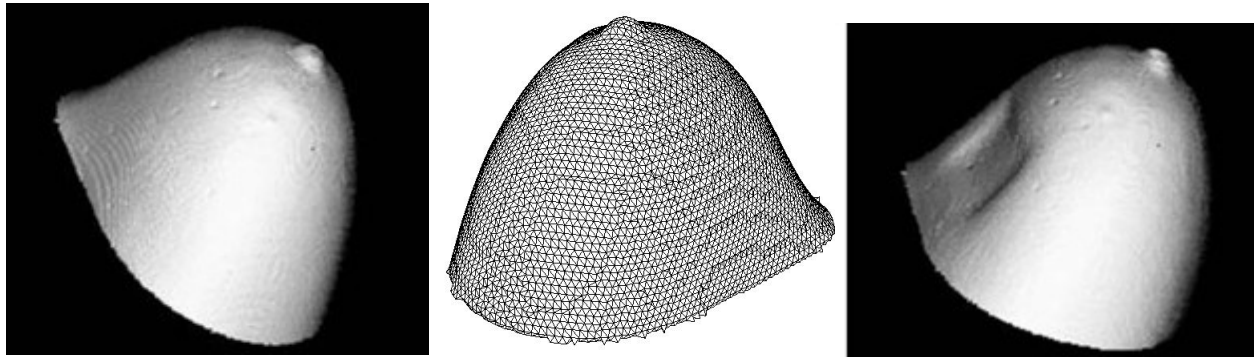


Figure 1. Surface renderings of CT breast volume used in MIE simulation experiments. From left to right: source image, finite element mesh, and target image with deformation created by presumed inflation of an air bladder.

2.3 Testing robustness of the algorithm

The current method of selecting boundary conditions as derived from experiences in 2D work requires manual interaction to guide or correct point correspondence for every surface node. Assuming that visible markers are available in an image, but that an input device (e.g. a mouse) is needed to identify the specific coordinates, this introduces an operator-dependent noise process in localizing any given point. The cumulative effect of these inaccuracies is propagated from the model to the image deformation and then the similarity measurements. For a given reconstruction experiment, the gold standard boundary condition set was systematically disrupted by adding a Gaussian randomized vector of a particular length (0.1, 0.2, 0.5, 1.0 or 2.0 voxel units). Figure 2 shows an example of the distortion caused by the applied noise.

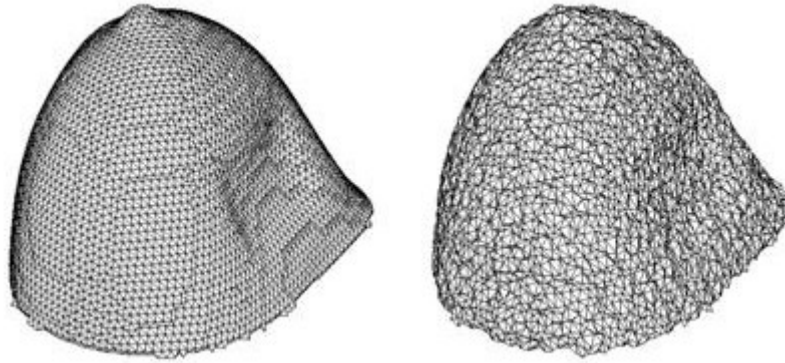


Figure 2. Example of distortion due to additive randomized error. The gold standard boundary conditions used to generate a controlled deformation produce the mesh shown on the left. For effect, the 2.0 voxel unit noise is show on the right.

2.4 Testing automated boundary condition generating methods

For this work, three methods of surface registration and point correspondence were considered for a more automated method of determining boundary conditions for the reconstruction algorithm. Two are derived from surface matching of potential energy distributions, and the other is a free-form warping.

If the flow of a substance over undeformed and deformed breast surfaces is taken to be a conserved process, then correspondence can be achieved by matching the same energy deposition between the source and target, that is, the equivalent level sets. In a physical sense, Laplace's equation can be used to describe this type of movement analogously to steady-state heat distribution:

$$\nabla^2 \Phi = 0 \quad (5)$$

where Φ would represent the temperature over a given region. Similarly, the diffusion equation describes the change in concentration or density of a material over time on a region:

$$\frac{\partial \Phi}{\partial t} = \alpha \nabla^2 \Phi \quad (6)$$

where α is the diffusivity constant.

These partial differential equations were used to calculate an energy distribution from the nipple area to the chest wall over the surface of a breast. Isocontours of particular energy values were then extracted from each surface to form a set of connected points. The symmetric closest point method described by [19] was used to determine a displacement field from which point correspondence at boundary nodes could be interpolated.

The third method involves thin-plate spline interpolation [20] to determine point correspondence. This was done to consider a widely-used method of non-rigid transform that can take advantage of fiducial information that should be present in future real-world data acquisition. The use of physical markers to track breast surface displacement during a deformation also defines a set of control points would allow the displacement boundary conditions for MIE to be simply interpolated from the local warping. In these simulation experiments, 40 surface nodes of known correspondence in each of the image volumes (due to the controlled deformation) served as fiducials.

2.5 Evaluation of reconstructions

Evaluation of the reconstruction results is performed by calculating the ratio of the elasticity of the inclusion to the rest of the breast for the distribution that yields the minimal objective function value over the course of optimization. The robustness of the MIE algorithm was tested with four trials at each of the magnitudes of randomized vectors (described above in Section 2.3), and the reconstruction results were averaged to determine a trend and possible threshold of noise tolerance for the algorithm.

For the automated boundary condition generation methods, a forward mapping of the objective function space was calculated to determine a theoretical optimum to the reconstruction. This was done by calculating the similarity values for model-based image deformations created by adjusting the elasticity contrast of the inclusion over a range of 0.5:1 to 30:1. An interpolating curve was fit and the minimum objective function value and associated elasticity contrast were extracted.

3. RESULTS

3.1 Robustness of algorithm to boundary condition noise

The following tables summarize the effects of additive noise of a particular magnitude to the gold standard boundary condition set. As the magnitude of the applied randomized vectors increased, a dramatic increase in the minimum objective function value is observed. Additionally, changes in the reconstructed elasticity contrast indicate that a cutoff exists in the ability of the algorithm to achieve a successful result (recall that the known correct ratio is 6:1) for disruption by vectors of length 0.5 voxel units or higher.

Table 1. Effect of applied random boundary condition noise on objective function space and reconstructed elasticity contrast ratio.

Randomized vector magnitude (voxel units)	Mean optimal objective function value	Mean optimal elasticity contrast value
0.1	2.85 ± 0.0382	5.62 ± 0.421
0.2	10.1 ± 0.367	5.70 ± 0.588
0.5	60.1 ± 4.19	2.36 ± 0.393
1.0	80.2 ± 0.561	2.47 ± 0.266
2.0	104 ± 3.42	2.17 ± 0.422

3.2 Use of automated point correspondence

Figure 3 depicts the deformation fields found by the various automated methods which were converted into a boundary condition sets and run through the reconstruction algorithm. Qualitatively, the displacements found by the diffusion method are quite different from the gold standard set, while the results from the solution of Laplace's equation and the thin-plate spline interpolation appear to be more satisfactory. The mean target registration error of the three methods confirms this with the spline having the best performance (0.26 mm), the Laplace method next (1.0 mm), and the diffusion method being the worst (2.0 mm). Inspection of Figure 4 further demonstrates that the imposition of an inexact boundary condition set on the model has a distinct effect on the optimization by shifting the minimum value to a different position. A comparison of the fit with the reconstruction in both objective function value and elasticity contrast is provided in Table 3 below and indicates that the algorithm is mostly in agreement with the predicted values for the Laplace and thin-plate spline methods but not as well for the diffusion method.

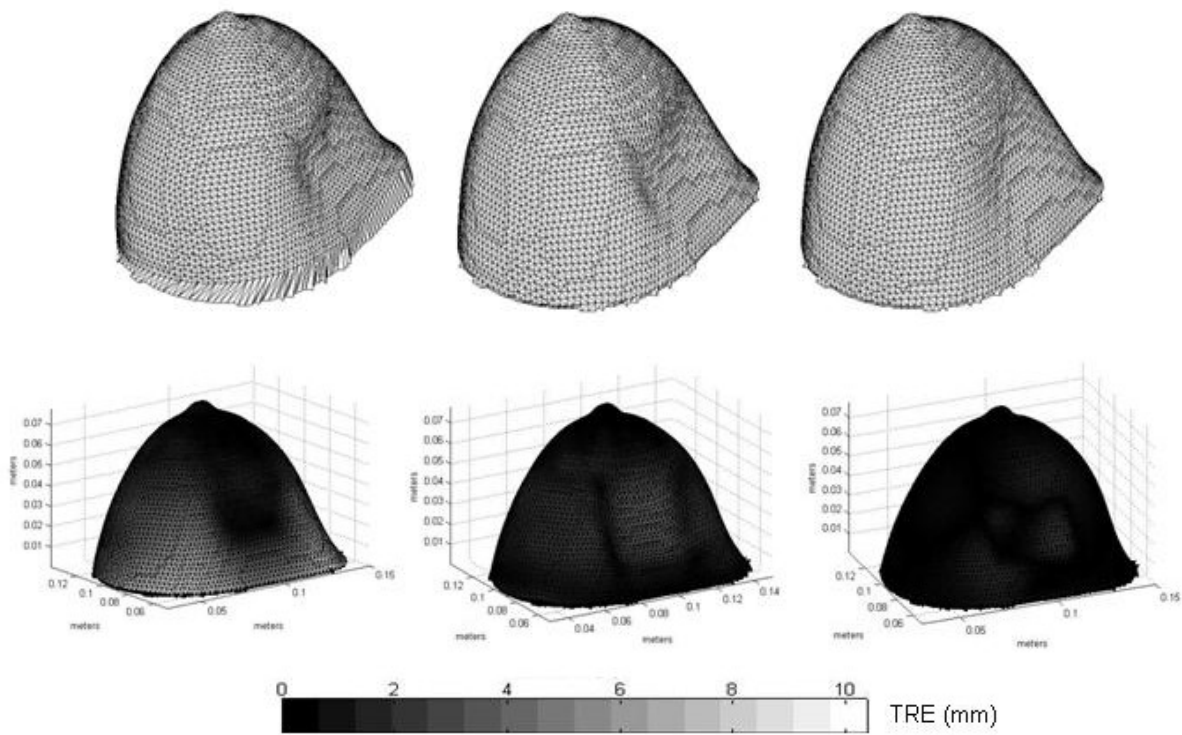


Figure 3. Three candidate automated methods for MIE boundary condition generation. Top row, from left to right: surface deformations calculated from diffusion energy matching, Laplace solution energy, and thin-plate spline interpolation. Bottom row: target registration error (TRE) distribution for each method when compared against the gold standard of known correspondence. The diffusion-based mesh is both qualitatively and quantitatively the worst performer. The Laplace solution appears to capture the shape of the bladder indentation more precisely, but the thin-plate spline has the best overall accuracy in determining point correspondence.

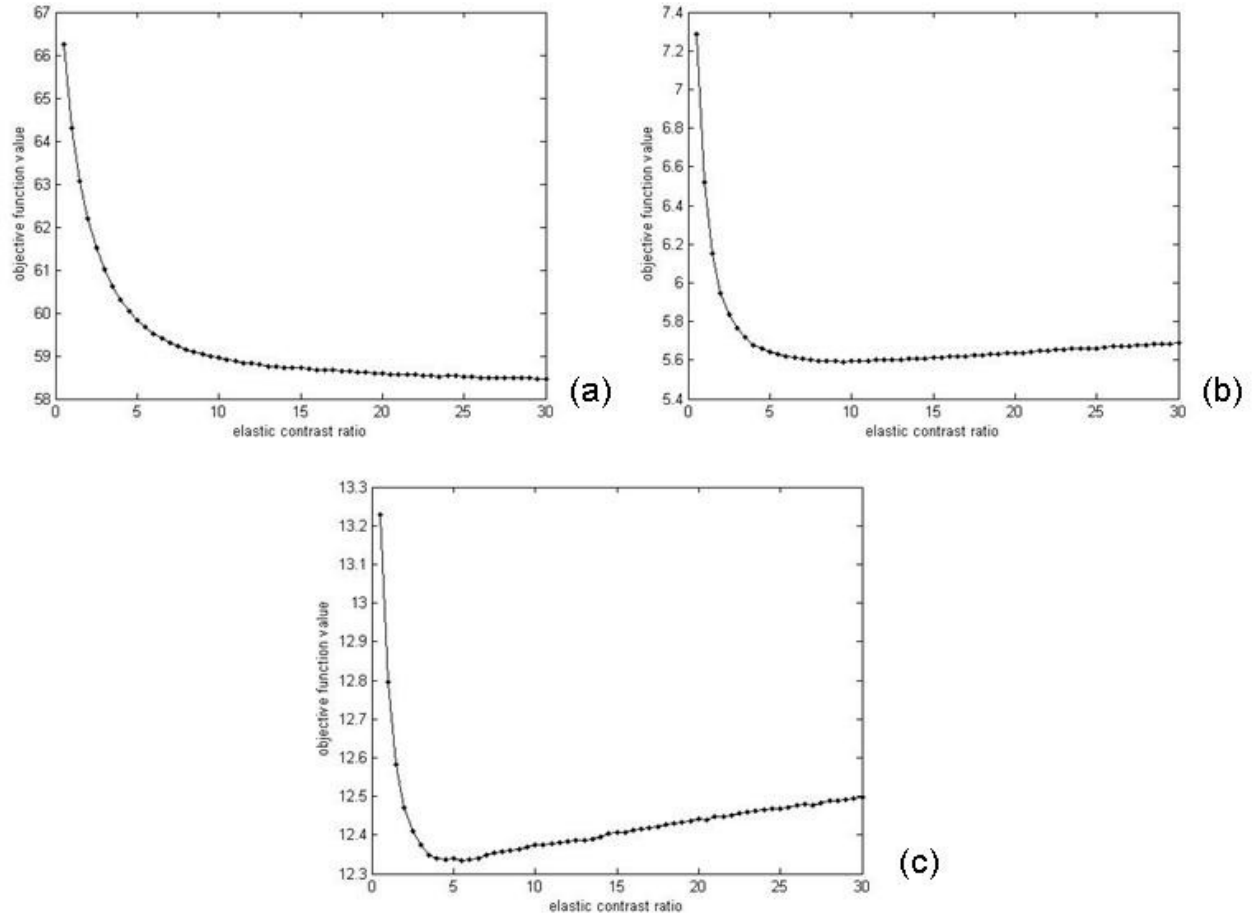


Figure 4. Mappings of objective function value vs. elasticity contrast ratio (tumor:breast) as affected by the boundary condition sets generated by different automated methods of surface point correspondence. The minimum value of each curve corresponds to the optimal elasticity contrast that can be achieved by the algorithm when constrained by the inaccuracies of the methods: (a) diffusion, (b) Laplace, and (c) thin-plate spline interpolations.

Table 3. Comparison of automated point correspondence methods on MIE reconstruction quality. Predicted values are found from the minimum point of the curves shown in Figure 4.

Method	Predicted minimum objective function value	Reconstructed minimum objective function value	Predicted optimal elasticity contrast	Reconstructed optimal elasticity contrast
Diffusion	58.5	58.8	30.0	12.6
Laplace	5.59	5.59	9.55	10.3
Thin-plate spline	12.3	12.3	5.55	5.66

4. DISCUSSION

The results of the boundary condition noise experiment are interesting because they indicate that improper localization of boundary points greater than or equal to 0.5 units of voxel spacing can introduce significant error to the reconstruction process and impair its ability to characterize the underlying elasticity distribution. This is a similar result to prior work done in two-dimensional systems in which successful reconstructions correlated to boundary condition selection error limited to half a pixel length [21]. It also confirms that randomizing the vectors is a significant challenge to the algorithm because it introduces highly non-physical deformations that cause backlash in the finite element mesh and other numerical anomalies.

The implausibility of performing manual selection on all 6,319 boundary nodes underscores the importance of finding an automated method for determining point correspondences, especially at less than 0.5 voxel units of error. In these simulation experiments, energy matching from the solutions of the diffusion and Laplace equations yield boundary condition sets that are inadequate for reconstructing a proper elasticity contrast. This can be partly explained because the mean errors of those surface registration techniques (as compared to the gold standard) are approximately 3.3 and 1.7 voxel units, respectively, which based on the randomized trials were magnitudes too large for the algorithm to handle. The diffusion-based boundary conditions also proved more difficult to obtain a stable solution for in the model, which probably contributed to the mismatch in reconstructed elasticity contrast. However, the results obtained from reconstructions using the thin-plate spline method are encouraging because the mean error was 0.43 voxel units. The reconstruction behavior in that case was consistent with the predicted objective function space and the optimal elasticity contrast was found to be within 6% of the true value. This preliminary result appears to identify the use of thin-plate spline interpolation as a strong candidate for generating boundary conditions for MIE. The use of 40 control points is also seen as a reasonable choice for data acquisition and processing in order to capture the extent of expected deformation processes.

5. CONCLUSIONS

In this work, we have demonstrated the effects of inaccuracies in boundary condition determination on an elastography method that maximizes the similarity between images of a tissue of interest acquired under two different states of mechanical loading. In order to characterize the robustness of the current version of this method, which has been updated to handle three-dimensional data in a parallelized scheme, randomized vectors were applied to distort a gold standard boundary condition set. The results were used to determine a threshold of accuracy needed in order to still achieve an accurate reconstruction. In order to streamline the pre-processing involved in the algorithm, three methods of automated point correspondence were evaluated. The success of these methods correlated with their mean error (relative to the true displacements) meeting the putative cutoff, and initial results indicate that established techniques such as thin-plate splines hold promise for generating boundary conditions.

REFERENCES

1. J. Ophir, I. Cespedes, H. Ponnekanti, Y. Yazdi, and X. Li, "Elastography - a quantitative method for imaging the elasticity of biological tissues," *Ultrasonic Imaging*. 13, 111-134 (1991).
2. A. L. McKnight, J. L. Kugel, P. J. Rossman, A. Manduca, L. C. Hartmann, and R. L. Ehman, "MR elastography of breast cancer: preliminary results," *AJR Am J Roentgenol*. 178(6), 1411-1417 (2002).
3. R. Sinkus, M. Tanter, T. Xydeas, S. Catheline, J. Bercoff, M. Fink, "Viscoelastic shear properties of *in vivo* breast lesions measured by MR elastography," *Magn Reson Imaging*. 23(2), 159-165 (2005).
4. L. V. Tsap, D. B. Goldgof, S. Sarkar, and P. S. Powers, "A vision-based technique for objective assessment of burn scars," *IEEE Trans Med Imaging*. 17, 620-633 (1998).
5. Y. Zhang, D. B. Goldgof, S. Sarkar, and L. V. Tsap, "A modeling approach for burn scar assessment using natural features and elastic property," *IEEE Trans Med Imaging*. 23, 1325-1329 (2004).
6. M. I. Miga, M. P. Rothney, and J. J. Ou, "Modality-independent elastography (MIE): potential applications for dermoscopy," *Medical Physics*. 32, 1308-1320 (2005).

7. L. Curiel, R. Souchon, O. Rouviere, A. Gelet, and J. Y. Chapelon, "Elastography for the follow-up of high-intensity focused ultrasound prostate cancer treatment: initial comparison with MRI," *Ultrasound Med Biol.* 31, 1461-1468 (2005).
8. C. W. Washington and M. I. Miga, "Modality independent elastography (MIE): a new approach to elasticity imaging," *IEEE Trans Med Imaging.* 23, 1117-1128 (2004).
9. M. I. Miga, "A new approach to elastography using mutual information and finite elements," *Phys Med Biol.* 48, 467-480 (2003).
10. M. I. Miga, "A new approach to elastographic imaging: modality independent elastography," *Proceedings of the SPIE.* 4684, 604-611 (2002).
11. K. J. Parker, L. S. Taylor, S. Gracewski, and D. J. Rubens, "A unified view of imaging the elastic properties of tissue," *J Acoustical Soc of America.* 117(5), 2705-2712 (2005).
12. A. Boresi, *Elasticity in Engineering Mechanics*, Wiley-Interscience, 2000.
13. L. Lapidus and G. F. Pinder, *Numerical Solution of Partial Differential Equations in Science and Engineering*, John Wiley & Sons, 1982.
14. J. M. Fitzpatrick, D. L. G. Hill, C. R. Maurer, "Image registration," *Handbook of Medical Imaging*, vol. 2. SPIE Press, 447-513, 2000.
15. N. Joachimowicz, C. Pichot, and J. P. Hugonin, "Inverse scattering: an iterative numerical method for electromagnetic imaging," *IEEE Trans Biomed Engineering.* 39, 1742-1752 (1991).
16. S. Balay, W. D. Gropp, L. C. McInnes, and B. F. Smith, "Efficient management of parallelism in object oriented numerical software libraries," in *Modern Software Tools in Scientific Computing*: Birkhauser Press, 163-202, 1997.
17. S. Balay, K. Buschelman, V. Eijkhout, W. Gropp, D. Kaushik, M. Knepley, L. McInnes, B. Smith, and H. Zhang, "PETSc Users Manual," Argonne National Laboratory, 2004.
18. T. A. Krouskop, T. M. Wheeler, F. Kallel, B. S. Garra, and T. Hall, "Elastic moduli of breast and prostate tissues under compression," *Ultrasonic Imaging.* 20, 260-274 (1998).
19. X. Papademetris, A. J. Sinusas, D. P. Dione, R. T. Constable, and J. S. Duncan, "Estimation of 3-D Left Ventricular Deformation from Medical Images using Biomechanical Models," *IEEE Transactions on Medical Imaging.* 21, 786-800 (2002).
20. A. Goshtasby, "Registration of images with geometric distortions," *IEEE Transactions on Medical Imaging.* 26(1), 60-64 (1988).
21. J. J. Ou, S. L. Barnes, and M. I. Miga, "Preliminary testing of sensitivity to input data quality in an elastographic reconstruction method," *IEEE International Symposium on Biomedical Imaging.* 948-951 (2006).

Using Laplace's equation for non-rigid registration of breast surfaces

Rowena E. Ong¹, Jao J. Ou¹, Michael I. Miga^{1,2,*}

¹Vanderbilt University, Department of Biomedical Engineering, Nashville, TN 37235

²Vanderbilt University Medical Center, Department of Radiology and Radiological Sciences,
Nashville, TN 37232

ABSTRACT

Recent advances in breast cancer imaging have generated new ways to characterize the disease. Many analysis techniques require a method for determining correspondence between a pendant breast surface before and after a deformation. In this paper, an automated point correspondence method that uses the surface Laplacian or the diffusion equation coupled to an isocontour matching and interpolation scheme are presented. This method is compared to a TPS interpolation of surface displacements tracked by fiducial markers. The correspondence methods are tested on two realistic finite element simulations of a breast deformation and on a breast phantom. The Laplace correspondence method resulted in a mean TRE ranging from 1.0 to 7.7 mm for deformations ranging from 13 to 33 mm, outperforming the diffusion method. The TPS method, in part because it utilizes fiducial information, performed better than the Laplace method, with mean TRE ranging from 0.3 to 1.9 mm for the same range of deformations. The Laplace and TPS methods have the potential to be used by analyses requiring point correspondence between deforming surfaces.

Keywords: Registration, non-rigid, breast, deformation, correspondence, surface Laplacian, diffusion, finite element, thin-plate spline, interpolation

1. INTRODUCTION

As breast cancer is estimated to kill over 40,000 women and be diagnosed in more than 178,000 in 2007 [1], the detection and treatment of breast cancer is an important area of scientific research. Many novel techniques to aid in tumor detection are being developed that exploit the difference in physical properties between healthy and cancerous tissue. Some of these techniques measure the optical, electrical, or elastic properties of tissue, including near-infrared tomography [6], electrical impedance tomography (EIT) [7], ultrasound elastography (USE) [8], magnetic resonance elastography (MRE) [9], and in particular, modality-independent elastography (MIE) [2,3].

MIE is a reconstruction algorithm for elasticity imaging that can be used for detecting breast tumors. It involves imaging a pendant breast before and after a compression and using these images to reconstruct the elastic properties of the tissue using a nonlinear optimization framework, computer models of soft-tissue deformation, and standard measures of image similarity. Unique to MIE is its ability to utilize images from any modality such as MRI or CT, as well as its usage of image similarity measures that make direct displacement measurements unnecessary.

One requirement of MIE is an automated method of finding point correspondence between the pendant breast surfaces before and after compression, needed to specify the boundary conditions for the elasticity model. As the breast is composed of soft tissue that deforms non-rigidly, standard rigid registration methods cannot be applied. Previous work in non-rigid registration includes using splines and FEM models [11], as well as point-based methods such as the symmetric closest point (SCP) algorithm [10].

In this paper, two automated methods that use the Laplace and diffusion equations to establish point correspondence between deformed breast surfaces were developed and compared to a standard thin-plate spline (TPS) interpolation method [4].

*michael.i.miga@vanderbilt.edu

2. METHODOLOGY

2.1 Laplace and diffusion methods of finding point correspondence

A major investigative task of this work was to evaluate whether the energy distributions modeled by a partial differential equation (PDE) over an undeformed (*source*) surface and a deformed (*target*) surface can be used to find the correspondence between the two surfaces. In this method, the Laplace and diffusion equations were independently solved over the source and target meshes using the finite element method (FEM). Laplace's equation is most commonly used to describe potential flow problems such as in thermal, fluid, and electrostatic systems and is given by

$$\nabla \cdot (\sigma \nabla \Phi) = 0 \quad (1)$$

where Φ represents the potential and σ describes the spatially varying conductivity. The diffusion equation which allows a time-varying potential is given by

$$\frac{d\Phi}{dx} = \nabla \cdot (\alpha \nabla \Phi) \quad (2)$$

where Φ represents the potential and α is the diffusion coefficient. Let Φ_{source} refer to the solution to the Laplace or diffusion equation over the source surface, and let Φ_{target} refer to the solution over the target. The basic premise is that the potential field distributed over the source and target surfaces as calculated by the Laplace or diffusion equation will provide information about the correspondence between the source and target surfaces.

To solve the equations, Dirichlet boundary conditions were set to simulate potential flow from the nipple area to the chest wall over the surface of a pendent breast (specifically, nodes in the nipple and chestwall area were given boundary values of 1 and 0, respectively). To solve equation 1, a Galerkin finite element method is used whereby the equations are expressed along the surface orientation ($\sigma=1$). To solve equation 2, a similar scheme was used for handling the spatial component of the PDE and a fully implicit backwards Euler scheme was used for time-stepping. In the case of equation 2, a no-flux condition was prescribed at the chest wall, and the potential field was allowed to propagate from the nipple ($\alpha=1$). In this calculation, time-stepping was stopped once the potential field reached the chest wall.

After the Laplace or diffusion equation was solved over the source and target surfaces, the solutions were used to establish correspondence between the source and target nodes. This involved two distinct processes: finding correspondence between isocontours of Φ_{source} and Φ_{target} and then "interpolating" that correspondence back to every source node on the mesh. In the first step, isocontours were extracted from Φ_{source} and Φ_{target} for a set of selected isovalues. The correspondence between the source and target isocontours was determined by aligning the contours by their centroids and using the SCP algorithm. In the second step, the displacement vectors at the source isocontours were interpolated to all source nodes using a thin-plate spline. The final correspondence was found by adding these displacements to the source nodes to get the location of the corresponding point on the target surface.

The method can be summarized in the following steps:

1. Obtain the undeformed source mesh and deformed target mesh that define a breast surface before and after deformation.
2. Assign boundary conditions at nipple and/or chest wall nodes.
3. Solve PDE (diffusion or Laplace) over the source and target meshes using FEM.
4. Extract isocontours on the source and target surfaces.
5. Determine point correspondence between source and target isocontours using SCP.
6. Interpolate displacements at source isocontours to all source nodes.

2.2 Using thin-plate spline interpolation to find point correspondence

One advantage of the PDE-based correspondence methods is that they do not explicitly rely on external markers to constrain the matching process. However, when real-world data is acquired, fiducials are anticipated to be available. Therefore, TPS interpolation is another method that can be used to find point correspondence [4]. Although there are many different methods for interpolation, including polynomial splines and B-splines [11], TPS interpolation was chosen in part because it does not require a regular grid, the effects of changing a control point are localized, and it is a standard

method that has been successfully used in many non-rigid registration applications. In the simulation experiments described below, TPS interpolation was used to find point correspondence by choosing 40 points on the source surface to act as fiducials. The known displacements at these nodes were then interpolated to all surface nodes using TPS.

The Laplace, diffusion, and TPS methods for finding point correspondence described above were tested on two simulation data sets and a breast phantom.

2.3 Simulation experiments

To perform a controlled test of the methods described above on a breast-shaped surface, a CT image volume of a pendant breast (courtesy of the Dept. of Radiology, University of California-Davis) was segmented to create a source surface consisting of 6,313 points. Two types of deformations were simulated by assuming different contact geometries of an air bladder being inflated against the breast surface. Circular and rectangular cross-sectional areas of a Gaussian stress distribution positioned along the lateral aspect of the breast were used to define Type 2 boundary conditions for a finite element-based deformation; the base was made to be affixed to the chest wall. The displacement solutions, based on a three-dimensional linear elastic model of a Hookean solid, were applied to create the target surfaces for the two simulations (Figure 1).

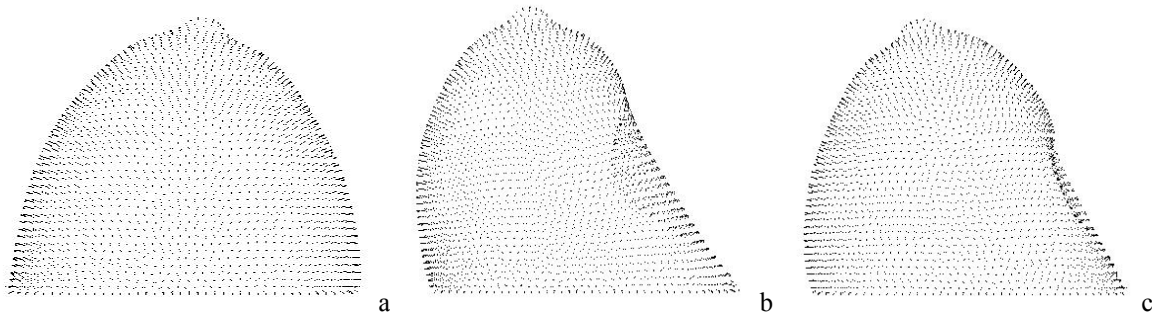


Figure 1. Breast surface point sets. (a) Source surface extracted from CT volume of a breast. (b) Target surface generated from first simulation using circular cross-section of a Gaussian stress distribution. (c) Target surface generated from second simulation using rectangular cross-section of a Gaussian stress distribution. The correspondence between the source and target surfaces was determined using the Laplace, diffusion, and TPS methods.

2.4 Phantom experiments

A breast phantom was constructed to test the point correspondence methods with real-world data. The phantom was fabricated from an 8% w/v solution of polyvinyl alcohol that was frozen in the upper half of a 2-liter beverage container for 16 hours. After 8 hours of thawing, thirty-four 1-mm stainless steel ball bearings were implanted directly under the surface of the resulting cryogel to act as fiducials.

The phantom was then imaged inside a custom-built rectangular chamber designed to deliver compression by means of an air bladder placed against the surface of the phantom (Figure 2). CT images (512 x 512 x 174, 0.54 x 0.54 x 1 mm voxel spacing) were acquired with the phantom at three different states of mechanical deformation (undeformed, 50% of maximum bladder pressure, and full inflation). Triangular surface meshes were obtained by semi-automatic segmentation of the image volumes using the surface extraction tools in ANALYZE 6.0 (Mayo Clinic, Rochester, MN), and the coordinates of the fiducial centroids were localized. These meshes contained approximately 8127, 6777, and 8260 nodes, respectively.

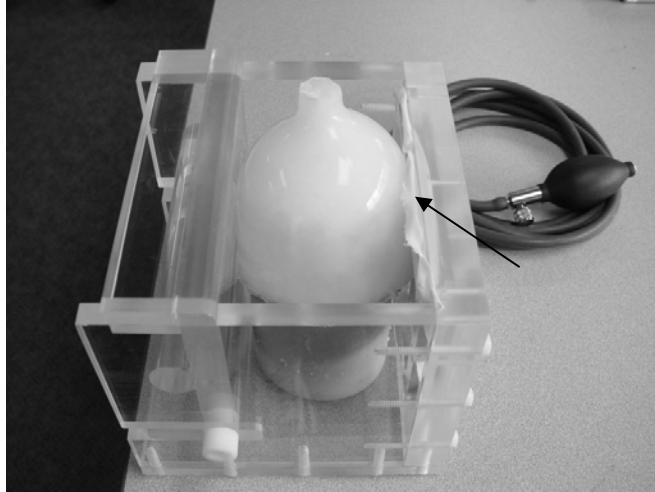


Figure 2. Experimental system for image data acquisition. A polyvinyl alcohol cryogel is placed within a Plexiglas chamber with its surfaces held in place against the walls. Compression is delivered through an air bladder (arrow) inflated manually through a bulb adapted from a standard sphygmomanometer.

The Laplace, diffusion, and TPS methods were tested on the phantom surface meshes. For the TPS method, 30 of the fiducials was used in the interpolation and the four remaining fiducials were reserved for validation. The fiducials used in interpolation and validation were selected such that the distribution for both groups over the surface was roughly even and included the deformed region.

2.5 Validation

In order to assess the accuracy of the simulation and phantom experiments, the target registration error (TRE) was calculated. The TRE measures the error between the correspondence determined by the registration method and the true correspondence [11]. For the simulation experiments, the TRE was calculated as the Euclidean distance between the corresponding target points determined by the Laplace, diffusion, or TPS method and the true target points. Since the true correspondence between the source and target surfaces was known, the TRE was calculated for each source node, and the average and maximum were reported. For the phantom experiment, the TRE was calculated using the centroids of the bead fiducials implanted directly under the phantom surface. Since the “gold standard” correspondence was known only at the fiducials, the TRE could only be calculated at these locations.

In addition, since one crucial step in both the Laplace and diffusion methods is to find point correspondence between the source and target isocontours (step 6 of algorithm summary), we evaluated how well the SCP algorithm performed in this step for the simulation data. To accomplish this, the SCP method was given a set of source isocontours and their true corresponding target contours, and the error (the Euclidean distance between the true target point and the corresponding target point determined by SCP) was calculated.

3. RESULTS

3.1 Simulation 1 (circular deformation source)

The Laplace and diffusion equations were solved over the surfaces generated from simulation 1 (cranial-caudal deformation source with maximum displacement of 33 mm) to find point correspondence between the source and target breast surfaces. For comparison, TPS interpolation using 40 simulated fiducials was also used to find point correspondence. The accuracy of each method was assessed by calculating the TRE at each surface node (Figure 3).

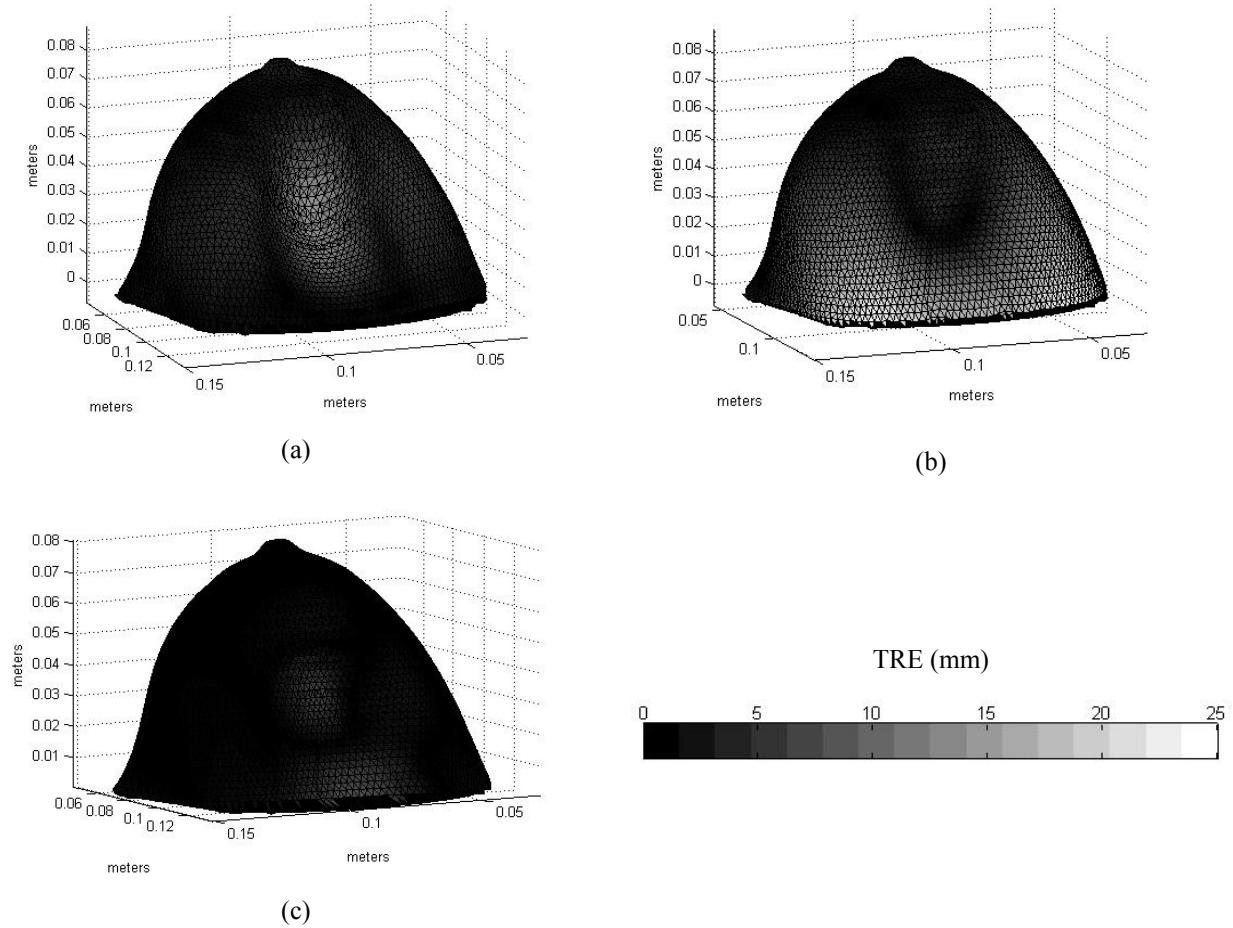


Figure 3. TRE displayed for breast simulation 1 (circular deformation source) when (a) Laplace equation, (b) diffusion equation, and (c) TPS interpolation were used to find point correspondence. The TPS method resulted in the lowest error overall (mean TRE 0.4 mm), followed by the Laplace method (mean TRE 2.3 mm) and diffusion method (max TRE 4.5 mm). The highest TRE is found in the deformed region when the Laplace method is used and in the base when the diffusion method is used.

The results (Table 1) indicated that the Laplace method performed more accurately overall than the diffusion method; however, the area with the highest amount of error differed. When the Laplace method was used, the deformed region had the highest error, whereas when the diffusion method was used, the area farthest from the diffusion source had the highest error. (In this case, since the diffusion source was located in the nipple area, the highest error occurred in the chest wall region.) The TPS interpolation had the lowest error overall, and the error distribution over the surface was related to the locations of the simulated fiducials.

The results given above pertain to a simulated compression with a maximum displacement of approximately 33 mm. Since this amount of compression may be larger than is needed for many applications and may introduce other unwanted effects for MIE due to non-linear elastic behavior, the point correspondence methods were also tested for lesser amounts of compression. The TRE for different amounts of compression when the Laplace method was used to find point correspondence is shown in Figure 4. The TRE appears to increase linearly with respect to increasing compression.

The mean and maximum error for the isocontour point correspondence determined by the SCP algorithm (detailed in methods section) was calculated (Figure 5). The isocontour correspondence given by the SCP algorithm had a maximum error of about 5 mm for the maximum compression of 33 m.

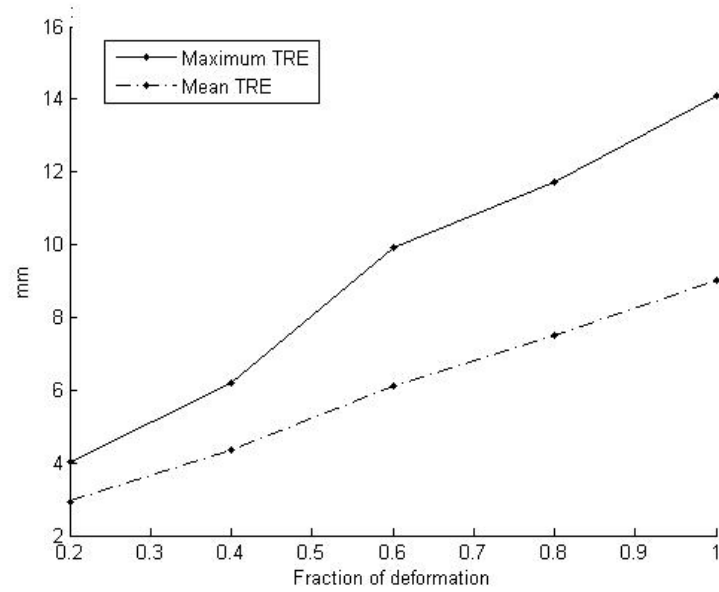


Figure 2. Maximum TRE (solid line) and mean TRE (dotted line) when the Laplace method was used to find point correspondence between the source and target surfaces at different levels of compression. A deformation of 100% indicates a maximum displacement of approximately 33 mm. The TRE seems to increase linearly with respect to the amount of deformation

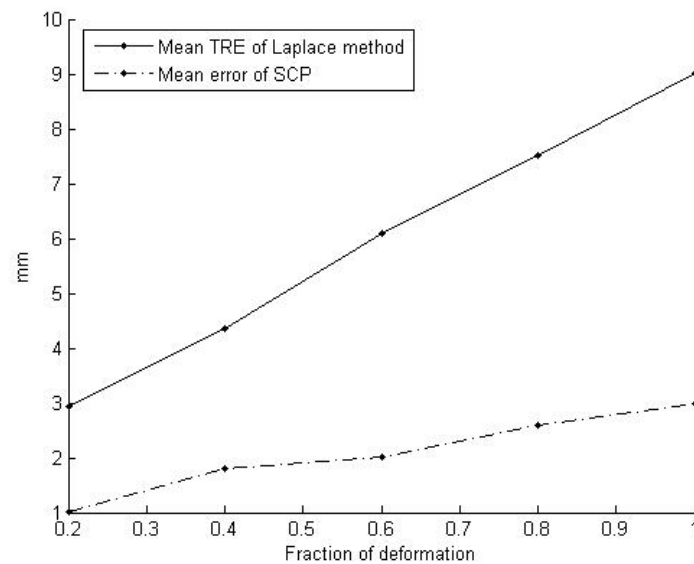


Figure 5. Evaluation of the accuracy of the SCP method used to find isocontour correspondence. The mean error of the SCP method (dotted line) is compared to the mean error of the Laplace method (solid line) when SCP method was used to find isocontour correspondence for simulation 1 data at different levels of compression. (A deformation of 100% indicates a maximum displacement of approximately 33mm.)

3.2 Simulation 2 (rectangular deformation source)

When the Laplace, diffusion, and TPS interpolation methods were used to find point correspondence between the breast surfaces generated by simulation 2 (a more realistic simulation using a rectangular deformation source with a maximum displacement of 13 mm), the results (Figure 6) were very similar to those from simulation 1. However, the TRE for all three methods (Table 1) was slightly lower, possibly due to the lower degree of compression simulated.

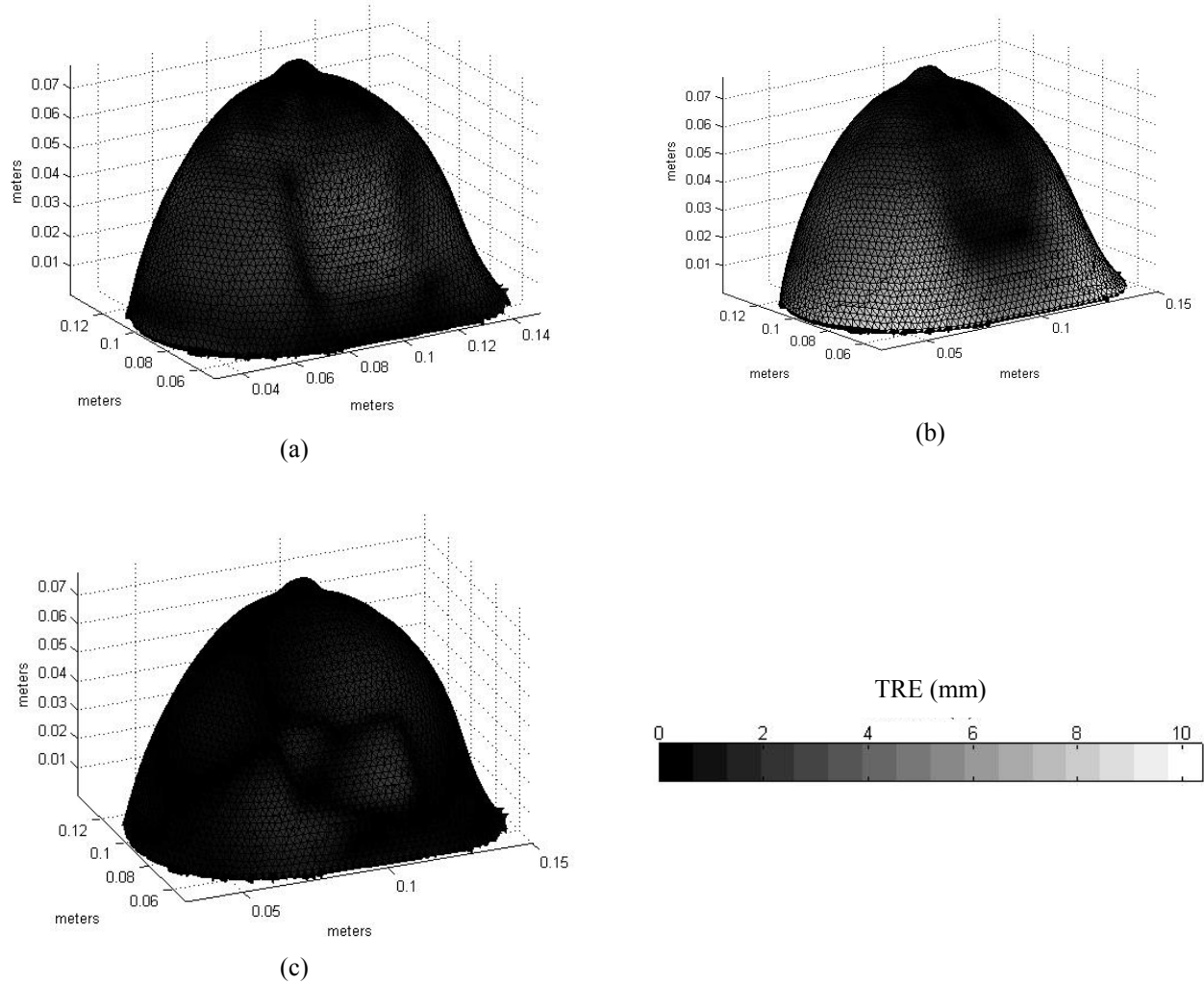


Figure 3. TRE displayed for breast simulation 2 (rectangular deformation source) when (a) Laplace equation, (b) diffusion equation, and (c) TPS interpolation were used to find point correspondence. The TPS method resulted in the lowest error overall (mean TRE 0.3 mm), followed by the Laplace method (mean TRE 1.0 mm) and diffusion method (mean TRE 2.1 mm). The results are similar to that of simulation 1

3.3 Phantom

The Laplace and diffusion methods were used to determine point correspondence between the noncompressed and compressed surfaces of a breast phantom. The results were validated by calculating the TRE at 34 fiducials located directly below the surface of the phantom. For comparison, TPS was used to interpolate the displacements of 30 fiducials to all surface nodes, and the TRE was calculated using the 4 remaining fiducials.

The results for a 50 and 100% compression (with a maximum displacements of about 20mm and 36 mm, respectively) are shown in Table 2. As in the simulations, the Laplace method performed better overall than the diffusion method and had lower TRE. The TRE for the TPS interpolation was lower than that for the Laplace and diffusion methods, but varied with the number and locations of fiducials used in the interpolation.

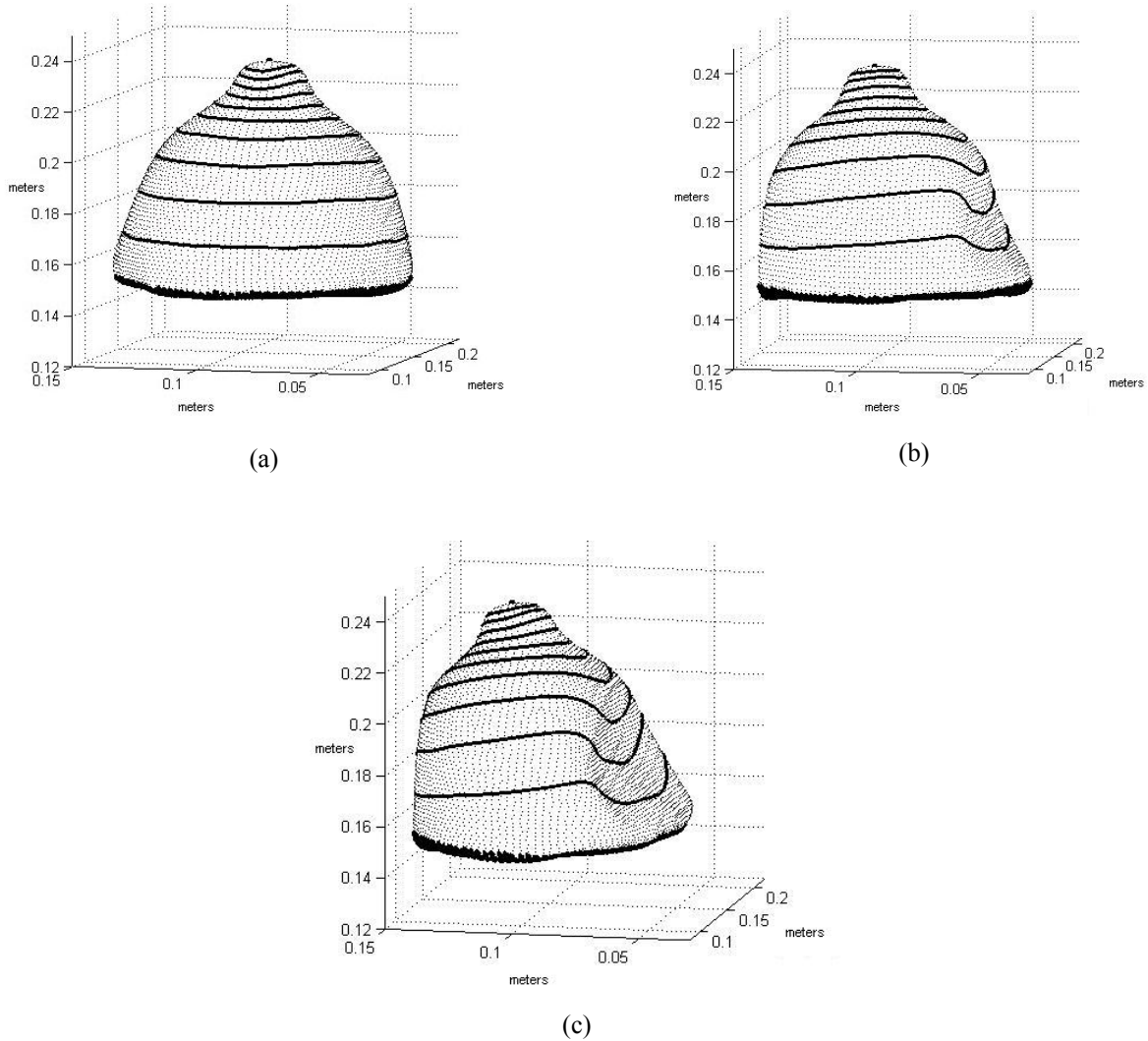


Figure 4. Breast phantom surfaces (a) before compression, (b) at 50% compression with maximum displacement of .020 m, and (c) at 100% compression with maximum displacement of .036 m.) Lines indicate isocontours at different values of k . Black nodes at the nipple and base indicate the nodes assigned boundary values.

Table 1. TRE for different point correspondence methods tested on breast surfaces generated from simulation 1 (point deformation source with max displacement of 33 mm) and simulation 2 (rectangular deformation source with max displacement of 13 mm) breast surfaces. The Laplace method outperformed the diffusion method, while the TPS method performed best of all.

	Simulation 1		Simulation 2	
	Max TRE (mm)	Mean TRE (mm)	Max TRE (mm)	Mean TRE (mm)
Laplace	14.6	2.3	4.6	1.0
Diffusion	24.2	4.5	10.3	2.1
TPS (40 fiducials)	7.6	0.4	2.6	0.3

Table 2. TRE for different point correspondence methods tested on breast phantom at approximately 50% and 100% compression, with max displacements of 20 and 36 mm, respectively. The Laplace method outperformed the diffusion method, while the TPS method performed best of all.

	50% Compression		100% Compression	
	Max TRE (mm)	Mean TRE (mm)	Max TRE (mm)	Mean TRE (mm)
Laplace	8.1	3.5	16.4	7.7
Diffusion	11.9	3.9	19.4	7.9
TPS *	1.5	1.1	2.6	1.9

* TPS interpolation using 30 fiducials; 4 fiducials were used to calculate TRE.

4. DISCUSSION

Of the three registration methods evaluated, the TPS method consistently outperformed the Laplace and diffusion methods and had the lowest error for both the simulation and phantom experiments. However, it is important to note that a comparison of the PDE-based methods and the TPS method is not entirely fair since the TPS method relies on fiducial information that the Laplace and diffusion methods do not require. The performance of the TPS method is dependent on both the number and placement of these fiducials. These results indicate that 30- 40 fiducials with an even distribution over the surface should be sufficient to register surfaces (with 13-33 mm deformations) with mean TRE ranging from 0.3 to 1.9 mm. Although further studies are needed to determine the optimal number and placement of fiducials, experience suggests that increasing the number of fiducials in the areas with greatest deformation increases registration accuracy, and conversely, lowering the number of fiducials in those areas causes a significant decrease in accuracy.

The results indicate that the Laplace method is a useable surface registration method. Although the Laplace method did not perform as accurately as the TPS method, it has the advantage of not requiring fiducial information. However, one of the challenges of the Laplace method is determining the regions to which boundary conditions are assigned. Accurate selection of these regions is important because the implicit correspondence between these regions is used by the Laplace equation to obtain the correspondence for the rest of the surface. For these studies, the nipple region and the chest wall boundary regions were selected manually. Further studies may be needed to find a method to automate the selection of the boundary regions and to evaluate how error in the selection of these regions affects the final registration error.

Although the diffusion method does have certain advantages over the Laplace and TPS registration methods, several problems prevent it from becoming a viable surface registration technique. The advantages of the diffusion method are that the correspondence near to the diffusion source (in this case, the nipple) is relatively accurate. In addition, the diffusion method only requires boundary conditions to be set in one region (in this case, the nipple), unlike the Laplace method, which requires boundary conditions at two regions (nipple and chest wall base), and the TPS method, which requires multiple points of constraint (at 34 fiducials).

However, the diffusion method does not appear to be a very useable surface registration method for the following reasons: the results indicate a substantial amount of error, the registration and resulting error are highly dependent on the diffusion parameters chosen (time step and final time in particular), and the diffusion parameters must be manually adjusted for each different surface mesh since there is no automated method to find the optimal diffusion parameters. Since the diffusion described by the PDE is by definition a non steady-state process, an optimal registration requires that the diffusion front should travel over the entire surface between the nipple and base and stop at the base in order to assure correspondence for as much as the surface as possible. If the parameters are chosen such that the diffusion front does not reach the base, the correspondence for the regions not reached by the diffusion front cannot be constrained and must be interpolated from the displacements of the surrounding regions. Conversely, if the diffusion front travels for too long a time, the solution over the surface approaches saturation, resulting in a flat gradient and lack of isocontours from which to establish correspondence. Various modifications to the diffusion method employing curvature information and using different diffusion coefficients were tested, but none was very successful. Therefore, the sensitivity of the diffusion method to parameters and substantial amount of error may prevent the diffusion method from being a viable surface registration method.

The TRE measured for each registration technique is not only dependent on the factors described above, but also on the amount of deformation of the target surface. The results suggest that the TRE increases roughly linearly with the amount of deformation. Using the simulation and phantom data presented here, one may be able to estimate the range of error expected when one of the described methods is used to register breast surfaces with a particular amount of compression. Conversely, the maximum amount of compression that will yield a registration within a given error bound can be roughly estimated. For the purposes of MIE, realistic compressions will be in the range of 1-2 cm.

Another factor related to the amount of compression is the distribution of TRE over the surface. The TRE was not evenly distributed; rather, the TRE in the areas of greatest deformation tended to be higher than the TRE elsewhere. Therefore, the mean TRE is not necessarily the best measure of the TRE over the surface; the max TRE may reflect the error in the deformed regions more accurately.

In addition to the evaluation of the three registration methods, the performance of the SCP algorithm was evaluated since the matching of the isocontours extracted from the source and target surface is a crucial step of the PDE-based registration methods. The results indicate that the amount of error the SCP algorithm contributes to the Laplace and diffusion methods is relatively small when compared to the total TRE (Figure 2).

In comparison to previous studies, the Laplace method outperformed the modified SCP method implemented by Schuler, et al. The data generated by first simulation described in this paper was also used to test the modified SCP method, and whereas the Laplace method had a maximum error of 14.6 mm for a deformation of 33 mm, the modified SCP method had a maximum error of 27.8 mm [5].

MIE is one application that may use the registration methods described in this paper, in this case to determine boundary conditions for its elasticity model. Preliminary studies indicate that TPS is the most viable registration method, the error of which is within the bounds required for a successful elasticity reconstruction (approximately 0.3 mm). The mean error for the Laplace registration method exceeds MIE's error bounds, and although the target boundary conditions produced by the Laplace method resulted in a viable mesh, the resulting elasticity reconstruction contained a considerable amount of error. The diffusion method could not be used in conjunction with MIE because of the extreme distortion of the target finite element mesh generated from the surface registration.

5. CONCLUSION

The results of the simulation and phantom experiments indicate that while TPS interpolation is the most accurate surface registration method of those evaluated, the Laplace method may be a viable surface registration technique if fiducials are not available. Although the TPS method consistently outperformed the Laplace method, its performance is dependent on the number and distribution of fiducials available. Both the Laplace and TPS methods have been used in MIE to register breast surfaces in order to determine boundary conditions for its elasticity model. In addition to MIE, the Laplace and TPS methods also have potential to be used for non-rigid registration in more general applications.

6. REFERENCES

1. American Cancer Society, "Cancer Facts and Figures 2007," <http://www.cancer.org/downloads/STT/CAFF2007PWSecured.pdf> (accessed Jan 18, 2007).
2. C. W. Washington and M. Miga, "Modality independent elastography (MIE): a new approach to elasticity imaging," *IEEE Transactions on Medical Imaging*, 23, 1117-28 (2004).
3. M. I. Miga, "A new approach to elastography using mutual information and finite elements," *Physics in Medicine and Biology*, 48, 467-80 (2003).
4. A. Goshtasby, "Registration of images with geometric distortions," *IEEE Transactions on Medical Imaging*, 26(1):60-64 (1988).
5. D. R. Schuler III, J. J. Ou, S. L. Barnes, M. I. Miga, "Automatic surface correspondence methods for a deformed breast," Proceedings of SPIE, Medical Imaging, 2006.
6. B. A. Brooksby, H. Dehghani, B. W. Pogue, and K. D. Paulsen, "Near-infrared (NIR) tomography breast image reconstruction with a priori structural information from MRI: algorithm development for reconstructing heterogeneities," *IEEE Journal of Selected Topics in Quantum Electronics*, 9, 199-209 (2003).
7. H. Frick and S. Morse, "The electrical capacity of tumors of the breast," *Journal of Cancer Research*, 10, 340-76 (1926).
8. T. A. Krouskop, T. M. Wheeler, F. Kallel, B. S. Garra, and T. Hall, "Elastic moduli of breast and prostate tissues under compression," *Ultrasonic Imaging*, 20, 260-74 (1998).
9. Y. Zho and Z. Gho, "A review of electrical impedance techniques for breast cancer detection," *Medical Engineering and Physics*, 25, 79-90 (2003).
10. X. Papademetris, A. J. Sinusas, D. P. Dione, R. T. Constable, and J. S. Duncan, "Estimation of 3-D Left Ventricular Deformation from Medical Images using Biomechanical Models," *IEEE Transactions on Medical Imaging*, 21, 786-800 (2002).
11. J. V. Hajnal, D. L. G. Hill, D. J. Hawkes, *Medical Image Registration*. CRC Press LLC, New York, 2001.